4

Dipole approach to high parton density QCD

We are now ready to present more recent developments in high energy QCD. We will consider DIS in the rest frame of a proton or a nucleus. In this frame a virtual photon fluctuates into a quark–antiquark pair, which, in turn, hits the proton or nuclear target. We argue that quark–antiquark dipoles are convenient degrees of freedom for high energy scattering in QCD. We will present a simple model of DIS on a nucleus, due to Glauber, Gribov, and Mueller, in which the $q\bar{q}$ dipole rescatters multiple times on a nuclear target consisting of independent nucleons. We then include quantum corrections to this multiple-rescattering picture: we argue that the initial $q\bar{q}$ dipole may develop a cascade of gluons before hitting the target nucleus. In the large-N_c limit the cascade is described by Mueller's dipole model. When applied to DIS the dipole cascade resummation leads to the Balitsky–Kovchegov (BK) nonlinear evolution equation. We describe approximate analytical and exact numerical solutions of the BK equation and show that it resolves both problems of BFKL evolution: BK evolution is unitary and has no diffusion into the IR. It generates a saturation scale Q_s that grows with energy, justifying the use of perturbative QCD. We conclude the chapter by presenting the Bartels–Kwiecinski–Praszalowicz (BKP) evolution equation for multiple reggeon exchanges, along with the evolution equation for (C-odd) odderon exchange.

4.1 Dipole picture of DIS

Let us begin by considering DIS in the rest frame of the proton or nucleus. While many conclusions in this chapter may also apply to proton DIS, in the strict sense our results would be justified only for DIS on a large nucleus since such a nucleus has a large atomic number parameter A allowing us to make the approximations we will need below. We will therefore only talk about DIS on a nuclear target.

Without any loss of generality we can choose a coordinate axis such that the momentum of the virtual photon is given by

$$q^\mu = \left(q^+, -\frac{Q^2}{q^+}, 0_\perp \right) \tag{4.1}$$

in the $(+, -, \perp)$ light cone notation. The light cone momentum of the virtual photon q^+ is very large (since the (high) photon–nucleus center-of-mass energy is $\hat{s} = mq^+$), so that its

https://doi.org/10.1017/9781009291446.005 Published online by Cambridge University Press

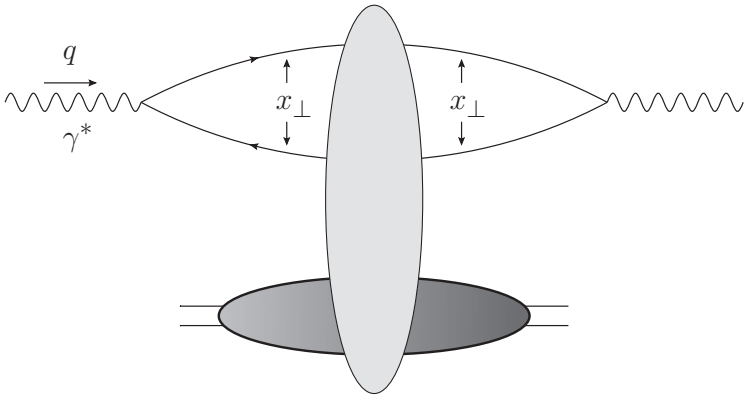

Fig. 4.1. Forward scattering amplitude for DIS on a proton or nuclear target in the rest frame of the target: the virtual photon splits into a $q\bar{q}$ pair which then interacts with the target. The interaction is depicted by the vertical oval. For simplicity the electron that emits the virtual photon is not shown.

coherence length in the longitudinal plus direction (see Sec. 2.3),

$$x^+ \approx \frac{2}{|q^-|} = \frac{2q^+}{Q^2}, \tag{4.2}$$

is much larger than the size of the nucleus. If the virtual photon fluctuates into a quark–antiquark pair, the typical lifetime of such a $q\bar{q}$ fluctuation would also be much longer than the nuclear diameter. Therefore, a DIS process in the nuclear rest frame occurs when a virtual photon fluctuates into a $q\bar{q}$ pair (which we will also refer to as a color dipole or simply a dipole); the $q\bar{q}$ pair proceeds to interact with the target (Gribov 1970, Bjorken and Kogut 1973, Frankfurt and Strikman 1988). The forward scattering amplitude for the process is pictured in Fig. 4.1, with the $q\bar{q}$ dipole–nucleus interaction represented by the vertical oval. This is the dipole picture of DIS (Kopeliovich, Lapidus, and Zamolodchikov 1981, Bertsch *et al.* 1981, Mueller 1990, Nikolaev and Zakharov 1991). Note that while the topology of the DIS diagram in Fig. 4.1 is the same as for DIS in the IMF, shown in Fig. 2.2, the time-ordering of the interactions is different in the two figures.

The interaction of a virtual photon with a nucleus can be viewed as a two-stage process: the virtual photon decays into a colorless dipole consisting of a quark and an antiquark and the colorless dipole travels through the nucleus. However, this separation between the time scale for the photon to decay into the $q\bar{q}$ pair and the interaction time is not the only advantage of the dipole picture. Another important simplification comes from the fact that in high energy scattering a colorless dipole, with transverse size $x_\perp$, does not change its size during the interaction and therefore the S-matrix of the interaction is diagonal with respect to the transverse dipole size (Zamolodchikov, Kopeliovich, and Lapidus 1981, Levin and Ryskin 1987, Mueller 1990, Brodsky *et al.* 1994). Indeed, while the colorless dipole is traversing the target, the distance $x_\perp$ between the quark and antiquark can only

https://doi.org/10.1017/9781009291446.005 Published online by Cambridge University Press

vary by an amount

$$\Delta x_\perp \approx R\frac{k_\perp}{E} \tag{4.3}$$

where $E \sim q^0$ denotes the energy of the dipole in the laboratory frame (the target rest frame), R is the longitudinal size of the target, and $k_\perp$ is the relative transverse momentum of the $q\bar{q}$ pair acquired through interaction with the target. In Eq. (4.3) $k_\perp/E$ is the relative transverse velocity of the quark with respect to the antiquark. From Eq. (4.3) we can see already that the change in the dipole size is suppressed by a power of the energy E and is therefore small. To quantify this better let us first remember the definition of Bjorken x, given in (2.2):

$$x = \frac{Q^2}{2P\cdot q} = \frac{Q^2}{mq^+} \approx \frac{Q^2}{2mE}. \tag{4.4}$$

Using Eq. (4.4) in Eq. (4.3) along with the uncertainty principle $Q \approx k_\perp \approx 1/x_\perp$ yields

$$\frac{\Delta x_\perp}{x_\perp} \approx 2mxR = \frac{4R}{l_{coh}} \ll 1, \tag{4.5}$$

where $l_{coh} = 2/(mx)$ is the coherence length of the dipole fluctuation (see Eq. (2.56)). We thus see that at small $x \ll 1/(mR)$, when the dipole interacts with the whole nucleus coherently in the longitudinal direction, the transverse recoil of the quark and the antiquark are negligible compared with the size of the dipole. Therefore the transverse size of the dipole is invariant in high energy interactions, as indicated in Fig. 4.1.

We conclude that in calculating the total DIS cross section, along with other high energy QCD observables, it is convenient to work in transverse coordinate space. We will therefore adopt a mixed representation: we will use longitudinal momentum space along with transverse coordinate space. Light cone perturbation theory (LCPT) is a very useful tool here again. Using LCPT to calculate the total DIS $\gamma^* A$ cross section we can factorize the diagram in Fig. 4.1 into the square of the light cone wave function $\Psi^{\gamma^*\to q\bar{q}}(\vec{x}_\perp, z)$ for the splitting of a virtual photon into a $q\bar{q}$ dipole and the total cross section for the scattering of a dipole on a target nucleus $\sigma_{tot}^{q\bar{q}A}(\vec{x}_\perp, Y)$, so that

$$\sigma_{tot}^{\gamma^* A}(x, Q^2) = \int \frac{d^2x_\perp}{4\pi}\int_0^1 \frac{dz}{z(1-z)}|\Psi^{\gamma^*\to q\bar{q}}(\vec{x}_\perp, z)|^2 \sigma_{tot}^{q\bar{q}A}(\vec{x}_\perp, Y). \tag{4.6}$$

Here $z = k^+/q^+$, with k^+ the light cone momentum of the quark in the $q\bar{q}$ pair. In general the dipole–nucleus cross section will depend on z too; however, in the eikonal and LLA approximations that we mainly consider below, $\sigma_{tot}^{q\bar{q}A}$ is independent of z. The net rapidity interval for the dipole–nucleus scattering is given by $Y = \ln(\hat{s}x_\perp^2) \approx \ln 1/x$ for $x_\perp \sim 1/Q$.

The reader may have other doubts about the factorization (4.6): after all, the LCPT rules presented in Sec. 1.3 require us to subtract the light cone energy of the incoming state in the energy denominator from each intermediate state's energy. Since the light cone energy of the incoming virtual photon is $q^- = -Q^2/q^+$, it seems that each intermediate state that

https://doi.org/10.1017/9781009291446.005 Published online by Cambridge University Press

we have absorbed into $\sigma_{tot}^{q\bar{q}A}(\vec{x}_\perp, Y)$ should "know" about the photon's energy. However, in the rest frame of the nucleus, q^- is equal to $-Q^2/q^+ \sim 1/\hat{s}$ and is therefore negligibly small compared with the typical minus components of momenta involved in dipole–nucleus interactions. The same would be true for dipole–nucleus scattering: the incoming dipole state would have a negligibly small light cone energy compared with the energies involved in the interaction. Therefore, in our eikonal approximation (up to corrections of order $1/\hat{s}$), we can interchange the negligible light cone energy q^- for the light cone energy of the dipole without changing the answer, thus justifying the factorization of Eq. (4.6). (Note that in calculating the light cone wave function $\Psi^{\gamma^* \to q\bar{q}}(\vec{x}_\perp, z)$ we cannot neglect the light cone energies of the virtual photon and the $q\bar{q}$ dipole, since they are the only terms entering the energy denominator.) Another important assumption is that the light cone energy of the target is not modified until the interaction with the dipole: one can show that the time scale of target fluctuations is much shorter than the lifetime of the dipole. Hence the target does not affect the virtual photon's wave function, since in constructing the latter the same light cone energy of the target enters into both the energies of the intermediate states and the initial-state energy, thus canceling in the energy denominators.

The factorization of Eq. (4.6) is very convenient: it allows us to separate the simple $\gamma^* \to q\bar{q}$ QED process from the strong interaction dynamics contained in $\sigma_{tot}^{q\bar{q}A}(\vec{x}_\perp, Y)$.

Note that the virtual photon may have either transverse or longitudinal polarization. Requiring that the photon polarization satisfies $\epsilon \cdot q = 0$ and imposing $\epsilon_T^2 = -1$ for transverse polarization and $\epsilon_L^2 = 1$ for the longitudinal polarization, we obtain for q^μ, Eq. (4.1), the following polarizations:

$$\epsilon_T^\lambda = (0, 0, \vec{\epsilon}_\perp^\lambda), \tag{4.7a}$$

$$\epsilon_L = \left(\frac{q^+}{Q}, \frac{Q}{q^+}, \vec{0}_\perp\right), \tag{4.7b}$$

with $\vec{\epsilon}_\perp^\lambda$ as given in Eq. (1.54). The polarization vectors (4.7) form a complete basis in the space of possible polarizations, so that the numerator of the photon propagator in the Landau gauge can be decomposed in terms of them as

$$g_{\mu\nu} - \frac{q_\mu q_\nu}{q^2} = -\sum_{\lambda=\pm} \epsilon_{T\mu}^\lambda \epsilon_{T\nu}^{\lambda *} + \epsilon_{L\mu} \epsilon_{L\nu}^*. \tag{4.8}$$

Using the polarizations (4.7) along with Eqs. (2.13) and (2.16) one can separate the total DIS cross section into transverse (T) and longitudinal (L) components (see Halzen and Martin 1984):

$$\sigma_T^{\gamma^* A} = \frac{4\pi^2 \alpha_{EM}}{q^0} W^{\mu\nu} \frac{1}{2} \sum_{\lambda=\pm} \epsilon_{T\mu}^\lambda \epsilon_{T\nu}^{\lambda *} = \frac{4\pi^2 \alpha_{EM}}{q^0} W_1 \tag{4.9a}$$

$$\sigma_L^{\gamma^* A} = \frac{4\pi^2 \alpha_{EM}}{q^0} W^{\mu\nu} \epsilon_{L\mu} \epsilon_{L\nu}^* = \frac{4\pi^2 \alpha_{EM}}{q^0} \left[-W_1 + \left(1 + \frac{\nu^2}{Q^2}\right) W_2\right], \tag{4.9b}$$

with ν as defined in Eq. (2.5) and α_{EM} the fine structure constant. Employing Eqs. (2.18a) and (2.18b), we can rewrite Eqs. (4.9) in the high energy $\nu \gg Q$ limit as expressions for

https://doi.org/10.1017/9781009291446.005 Published online by Cambridge University Press

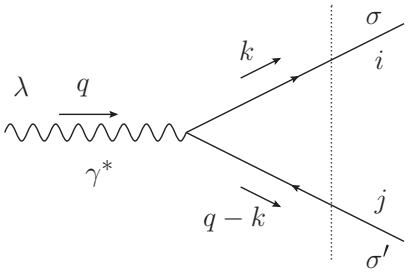

Fig. 4.2. Light cone wave function for a virtual photon fluctuating into a quark–antiquark pair (a dipole). The dotted line denotes the intermediate state.

the dimensionless structure functions:

$$F_2(x,\,Q^2) = \frac{Q^2}{4\pi^2\alpha_{EM}}\sigma_{tot}^{\gamma^* A} = \frac{Q^2}{4\pi^2\alpha_{EM}}\left(\sigma_T^{\gamma^* A} + \sigma_L^{\gamma^* A}\right), \tag{4.10a}$$

$$2xF_1(x,\,Q^2) = \frac{Q^2}{4\pi^2\alpha_{EM}}\,\sigma_T^{\gamma^* A}. \tag{4.10b}$$

It is useful to also define the longitudinal structure function F_L, which measures the violation of the Callan–Gross relation (2.44):

$$F_L(x,\,Q^2) \equiv F_2(x,\,Q^2) - 2xF_1(x,\,Q^2) = \frac{Q^2}{4\pi^2\alpha_{EM}}\,\sigma_L^{\gamma^* A}. \tag{4.11}$$

Equations (4.10) and (4.11) allow us to find the DIS structure functions using the transverse and longitudinal cross sections, which, with the help of Eq. (4.6), can be found from the dipole–nucleus scattering via

$$\sigma_{T,L}^{\gamma^* A}(x,\,Q^2) = \int \frac{d^2x_\perp}{4\pi}\int_0^1 \frac{dz}{z(1-z)}\,|\Psi_{T,L}^{\gamma^*\to q\bar{q}}(\vec{x}_\perp,\,z)|^2\,\sigma_{tot}^{q\bar{q}A}(\vec{x}_\perp,\,Y). \tag{4.12}$$

We have defined the transverse, $\Psi_T^{\gamma^*\to q\bar{q}}(\vec{x}_\perp,\,z)$, and longitudinal, $\Psi_L^{\gamma^*\to q\bar{q}}(\vec{x}_\perp,\,z)$, light cone wave functions, which differ by the polarization vector of the incoming virtual photon.

Let us now calculate the light cone wave functions $\Psi_{T,L}^{\gamma^*\to q\bar{q}}(\vec{x}_\perp,\,z)$ for the quark–antiquark fluctuations of a virtual photon. The diagram is shown in Fig. 4.2, in which the vertical dotted line denotes the intermediate state. Using the LCPT rules from Secs. 1.3 and 1.4, we write for the wave functions in momentum space (cf. the calculation in Sec. 2.4.2)

$$\Psi_{T,L}^{\gamma^*\to q\bar{q}}(\vec{k}_\perp,\,z) = eZ_f\,\frac{z(1-z)\delta_{ij}}{\vec{k}_\perp^2 + m_f^2 + Q^2z(1-z)}\,\bar{u}_\sigma(k)\gamma\cdot\epsilon_{T,L}^\lambda v_{\sigma'}(q-k), \tag{4.13}$$

where σ and σ' are the quark and antiquark helicities, i, j are their colors, m_f is the mass of a quark with flavor f, and Z_f is the quark's electric charge in units of the electron charge e. (Note that q^μ is given in Eq. (4.1).) As mentioned above, we define $z = k^+/q^+$ as the fraction of the photon's light cone momentum carried by the quark.

https://doi.org/10.1017/9781009291446.005 Published online by Cambridge University Press

Starting with the transverse polarization we substitute the polarization vector from Eq. (4.7a) into Eq. (4.13) and evaluate the Dirac matrix element using Appendix A.1, obtaining

$$\Psi_T^{\gamma^*\to q\bar{q}}(\vec{k}_\perp, z) = eZ_f\sqrt{z(1-z)}\,\delta_{ij} \times \frac{(1-\delta_{\sigma\sigma'})\vec{\epsilon}_\perp^{\,\lambda}\cdot\vec{k}_\perp(1-2z-\sigma\lambda)+\delta_{\sigma\sigma'}m_f(1+\sigma\lambda)/\sqrt{2}}{\vec{k}_\perp^2+m_f^2+Q^2z(1-z)}. \quad (4.14)$$

In arriving at Eq. (4.14) we have also used the fact that in two transverse dimensions $\vec{\epsilon}_\perp^{\,\lambda}\times\vec{k}_\perp = -i\lambda\vec{\epsilon}_\perp^{\,\lambda}\cdot\vec{k}_\perp$ for the $\vec{\epsilon}_\perp^{\,\lambda}$ from Eq. (1.54).

Since we are interested in using the virtual photon's wave function in transverse coordinate space in Eq. (4.12), we perform a Fourier transform of Eq. (4.14):

$$\Psi_{T,L}^{\gamma^*\to q\bar{q}}(\vec{x}_\perp, z) = \int \frac{d^2k_\perp}{(2\pi)^2} e^{i\vec{k}_\perp\cdot\vec{x}_\perp}\Psi_{T,L}^{\gamma^*\to q\bar{q}}(\vec{k}_\perp, z) \quad (4.15)$$

and employ Eq. (A.11) along with $K_0'(z) = -K_1(z)$ to obtain

$$\Psi_T^{\gamma^*\to q\bar{q}}(\vec{x}_\perp, z) = \frac{eZ_f}{2\pi}\sqrt{z(1-z)}\,\delta_{ij}\Bigg[(1-\delta_{\sigma\sigma'})(1-2z-\sigma\lambda)\,ia_f\frac{\vec{\epsilon}_\perp^{\,\lambda}\cdot\vec{x}_\perp}{x_\perp}K_1(x_\perp a_f) + \delta_{\sigma\sigma'}\frac{m_f}{\sqrt{2}}(1+\sigma\lambda)K_0(x_\perp a_f)\Bigg], \quad (4.16)$$

where

$$a_f^2 = Q^2z(1-z)+m_f^2. \quad (4.17)$$

The square of the absolute value of the transverse wave function (4.16), summed over all the outgoing quantum numbers and averaged over the possible polarizations of the incoming transverse photon is (Bjorken, Kogut, and Soper 1971, Nikolaev and Zakharov 1991) given by

$$|\Psi_T^{\gamma^*\to q\bar{q}}(\vec{x}_\perp, z)|^2 = 2N_c\sum_f\frac{\alpha_{EM}Z_f^2}{\pi}z(1-z) \times \left\{a_f^2\left[K_1(x_\perp a_f)\right]^2\left[z^2+(1-z)^2\right]+m_f^2\left[K_0(x_\perp a_f)\right]^2\right\}. \quad (4.18)$$

To calculate the longitudinal wave function $\Psi_L^{\gamma^*\to q\bar{q}}(\vec{x}_\perp, z)$ we repeat the above steps, now using the longitudinal polarization vector (4.7b) in Eq. (4.13). The transverse momentum space longitudinal wave function is

$$\Psi_L^{\gamma^*\to q\bar{q}}(\vec{k}_\perp, z) = \frac{eZ_f[z(1-z)]^{3/2}\,\delta_{ij}\,2Q(1-\delta_{\sigma\sigma'})}{\vec{k}_\perp^2+m_f^2+Q^2z(1-z)}. \quad (4.19)$$

In arriving at Eq. (4.19) we have neglected a term that would have given us a delta function, $\delta^2(\vec{x}_\perp)$, in the transverse coordinate-space wave function; as we will shortly see,

https://doi.org/10.1017/9781009291446.005 Published online by Cambridge University Press

zero-transverse-size dipoles do not interact with the nucleus (they have zero scattering cross section) and so such configurations do not contribute to the DIS structure functions.

Fourier-transforming Eq. (4.19) into transverse coordinate space yields

$$\Psi_L^{\gamma^* \to q\bar{q}}(\vec{x}_\perp, z) = \frac{eZ_f}{2\pi}[z(1-z)]^{3/2}\,\delta_{ij}\,2Q(1-\delta_{\sigma\sigma'})K_0(x_\perp a_f), \tag{4.20}$$

so that the longitudinal wave function squared, again with all summations performed, is (Bjorken, Kogut, and Soper 1971, Nikolaev and Zakharov 1991)

$$|\Psi_L^{\gamma^* \to q\bar{q}}(\vec{x}_\perp, z)|^2 = 2N_c \sum_f \frac{\alpha_{EM} Z_f^2}{\pi} 4Q^2 z^3 (1-z)^3 \left[K_0(x_\perp a_f)\right]^2. \tag{4.21}$$

To obtain the phase-space integral in Eqs. (4.6) or (4.12) we remember that the two-particle momentum phase space given in Eq. (1.82) is (remembering that in our case the quarks are not identical)

$$\int \frac{dz}{2z(1-z)} \frac{d^2k_\perp}{(2\pi)^3}. \tag{4.22}$$

After Fourier-transforming the wave function into transverse coordinate space the integral becomes

$$\int \frac{dz}{2z(1-z)} \frac{d^2x_\perp}{2\pi}, \tag{4.23}$$

in agreement with Eqs. (4.6) and (4.12).

We have now completed the calculation of the QED part of DIS in the dipole picture. Equations (4.18) and (4.21), when used in Eq. (4.12), give us the transverse and longitudinal DIS cross sections, which, in turn, when used in Eqs. (4.10) and (4.11) give us the structure functions. The interesting physics of strong interactions is contained in the dipole–nucleus scattering cross section $\sigma_{tot}^{q\bar{q}A}(\vec{x}_\perp, Y)$: most of this chapter is dedicated to calculating this quantity.

4.2 Glauber–Gribov–Mueller multiple-rescatterings formula

We begin by employing Eq. (3.119a) to rewrite the total dipole–nucleus scattering cross section as

$$\sigma_{tot}^{q\bar{q}A}(\vec{x}_\perp, Y) = 2\int d^2b\, N(\vec{x}_\perp, \vec{b}_\perp, Y), \tag{4.24}$$

where $N(\vec{x}_\perp, \vec{b}_\perp, Y)$ is the imaginary part of the forward scattering amplitude for a dipole of transverse size $\vec{x}_\perp$ interacting with the nucleus at impact parameter $\vec{b}_\perp$ and with net rapidity interval Y. Hence to find the cross section $\sigma_{tot}^{q\bar{q}A}$ we need to calculate $N(\vec{x}_\perp, \vec{b}_\perp, Y)$.

To find $N(\vec{x}_\perp, \vec{b}_\perp, Y)$ let us consider the following (Glauber) model. Assume that the nucleus is very large and dilute and is made out of $A \gg 1$ independent nucleons, where A is

https://doi.org/10.1017/9781009291446.005 Published online by Cambridge University Press

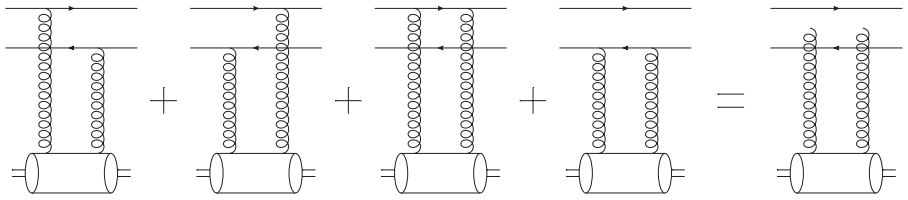

Fig. 4.3. The four diagrams contributing to dipole interaction with a single nucleon at the lowest nontrivial (two-gluon) order in the high energy approximation and an abbreviated notation for their sum.

the atomic number of the nucleus.[1] Any correlations between the nucleons are suppressed by powers of the large parameter A: hence our approximation corresponds to summing the leading powers of A. In evaluating the forward dipole–nucleus scattering amplitude $N(\vec{x}_\perp, \vec{b}_\perp, Y)$ we will follow the strategy originally outlined by Glauber and by Gribov (Glauber 1955, Franco and Glauber 1966, Gribov 1969b, Glauber and Matthiae 1970, Gribov 1970) and implemented in QCD by Mueller (1990).

4.2.1 Scattering on one nucleon

First we consider the case when the dipole interacts with only one nucleon in the nucleus. Assuming that the interaction is entirely perturbative, we see that the lowest-order contribution to the forward high energy scattering amplitude comes from a two-gluon exchange. The relevant diagrams are shown in Fig. 4.3. This lowest-order scattering process was calculated in Sec. 3.2. Employing the results of that section (see Eq. (3.25)) we can write down the total dipole–nucleon cross section as

$$\sigma^{q\bar{q}N} \approx \frac{2\pi\alpha_s^2 C_F}{N_c} x_\perp^2 \ln\frac{1}{x_\perp^2\Lambda^2}. \tag{4.25}$$

In arriving at Eq. (4.25) we have assumed that the dipole is perturbatively small, $x_\perp \ll 1/\Lambda_{QCD}$, and that the nucleon can be modeled as another dipole of transverse size $1/\Lambda \gg x_\perp$, with Λ some soft QCD scale of order Λ_{QCD}. We have also assumed that the nucleus is sufficiently large that the cross section does not depend on the dipole's orientation in the transverse plane, over which we therefore average.

At the same two-gluon order the unintegrated gluon distribution function of the nucleon can be found using Eq. (3.92) with the lowest-order BFKL Green function (3.59). This gives

$$\phi_{LO}^{onium}(x, k_\perp^2) = \frac{\alpha_s C_F}{\pi}\frac{2}{k_\perp^2}, \tag{4.26}$$

where we have assumed that $k_\perp \gg \Lambda$. The factor 2 on the right-hand side of Eq. (4.26) simply counts the number of quarks in the dipole representing the nucleon. It should be

[1] Strictly speaking A is called the mass number of the nucleus; nevertheless, we will follow the standard jargon in the high energy field and refer to it as the atomic number.

https://doi.org/10.1017/9781009291446.005 Published online by Cambridge University Press

replaced by N_c if one wanted to model the nucleon more realistically, as consisting of N_c valence quarks. Using Eq. (3.93) the corresponding lowest-order gluon distribution of an onium (a nucleon) turns out to be

$$xG_{LO}^{onium}(x, Q_\perp^2) = \frac{\alpha_s C_F}{\pi} 2 \ln \frac{Q^2}{\Lambda^2}. \tag{4.27}$$

Comparing Eq. (4.27) and Eq. (4.25), we can rewrite the latter as

$$\sigma^{q\bar{q}N} \approx \frac{\alpha_s \pi^2}{N_c} x_\perp^2 x G_N \left(x, \frac{1}{x_\perp^2} \right), \tag{4.28}$$

where xG_N is the gluon distribution in the nucleon (presently modeled as an onium).[2] Equation (4.28) has an advantage over Eq. (4.25): it is valid for any nonperturbative gluon distribution in the nucleon and is therefore more general. We will use these equations interchangeably, though.

To find the dipole–nucleus scattering cross section at a given impact parameter we need to average the dipole–nucleon scattering amplitude over all possible positions of the nucleon inside the nucleus and to sum over the A nucleons in the nucleus, all of which may participate in the interaction. We have

$$\frac{d\sigma_{LO}^{q\bar{q}A}}{d^2b} = \int db_3' d^2b_\perp' \rho_A(\vec{b}_\perp - \vec{b}_\perp', b_3') \frac{d\sigma^{q\bar{q}N}}{d^2b'}, \tag{4.29}$$

where $db_3' d^2b_\perp' = d^3b$ is the three-dimensional volume element and $\rho_A(\vec{b}_\perp, b_3)$ is the nucleon number density, with $\vec{b}_\perp = (b_1, b_2)$. In a simplified model, the nucleus has a constant nucleon number density $\rho_A = A/V$, where V is the volume of the nucleus in its rest frame. In the general case $\rho_A(\vec{b}_\perp, b_3)$ is given by the Woods–Saxon parametrization of the nuclear density (Woods and Saxon 1954).

Equation (4.29) gives the cross section for a dipole at impact parameter $\vec{b}_\perp$ scattering on a nucleon at impact parameter $\vec{b}_\perp - \vec{b}_\perp'$ (where $\vec{b}_\perp'$ is its transverse distance from the dipole), convoluted with the nucleon density ρ, which, in turn, is proportional to the probability of finding a nucleon at $\vec{b}_\perp - \vec{b}_\perp'$ (see Fig. 4.4). To simplify Eq. (4.29) we note that the perturbative scattering cross section falls off as $d\sigma^{q\bar{q}N}/d^2b' \sim 1/b_\perp'^4$ at large impact parameter, as can be seen for instance from Eq. (3.139) in Exercise 3.3 (after averaging over the azimuthal orientations of one dipole; this mimics an unpolarized nucleon, without any preferred direction). At nonperturbatively large impact parameter $b_\perp' \gtrsim 1/\Lambda_{QCD}$ one expects an even steeper falloff, $d\sigma^{q\bar{q}N}/d^2b' \sim \exp(-2m_\pi b_\perp')$ (cf. Eq. (3.113)). Hence the cross section $d\sigma^{q\bar{q}N}/d^2b'$ is localized at small impact parameters $b_\perp' \lesssim 1/\Lambda_{QCD}$.

In the large-A approximation that we are employing, one assumes that the nuclear wave function and hence the density $\rho_A(\vec{b}_\perp, b_3)$ does not change significantly over distances of order $1/\Lambda_{QCD}$, which is small compared with the size of the nucleus, so that the nucleon has an approximately equal probability of being anywhere within this transverse range.

[2] We would like to stress here that in order to conform to the standard notation we write the gluon distribution with Bjorken x in its argument, but throughout this section the gluon distribution is taken at the lowest (two-gluon) order and is therefore x-independent.

https://doi.org/10.1017/9781009291446.005 Published online by Cambridge University Press

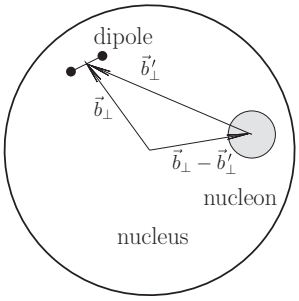

Fig. 4.4. The geometry of dipole–nucleus scattering in the transverse coordinate plane. To illustrate the notation of Eq. (4.29) the dipole is placed far from the nucleon; in reality $b'_\perp \lesssim 1/\Lambda_{QCD}$.

Therefore, for large nuclei we can approximate $\rho_A(\vec{b}_\perp - \vec{b}'_\perp, b'_3)$ as $\rho_A(\vec{b}_\perp, b'_3)$ and recast Eq. (4.29) by integrating over $b'_\perp$ as

$$\frac{d\sigma_{LO}^{q\bar{q}A}}{d^2b} = T(\vec{b}_\perp)\sigma^{q\bar{q}N}, \tag{4.30}$$

where we have defined the *nuclear profile function* $T(\vec{b}_\perp)$ by

$$T(\vec{b}_\perp) \equiv \int_{-\infty}^{\infty} db_3 \rho_A(\vec{b}_\perp, b_3). \tag{4.31}$$

For a spherical nucleus of radius R with constant nucleon number density $\rho_A = A/V$ one has $T(\vec{b}_\perp) = 2\rho_A\sqrt{R^2 - \vec{b}_\perp^2}$.

Comparing Eq. (4.30) with Eq. (4.24) and employing Eq. (4.28) we obtain

$$\begin{aligned} N_{LO}(\vec{x}_\perp, \vec{b}_\perp, Y) &= \frac{\alpha_s \pi^2}{2N_c} T(\vec{b}_\perp)\, x_\perp^2 x G_N\left(x, \frac{1}{x_\perp^2}\right) \\ &= \frac{\pi \alpha_s^2 C_F}{N_c} T(\vec{b}_\perp)\, x_\perp^2 \ln\frac{1}{x_\perp \Lambda}, \end{aligned} \tag{4.32}$$

where in the last line we have modeled the nucleon by a single quark with gluon distribution

$$x G(x, Q_\perp^2) = \frac{\alpha_s C_F}{\pi} \ln\frac{Q^2}{\Lambda^2}.$$

We now have the forward dipole–nucleus scattering amplitude for the case when only one nucleon in the nucleus interacts with the dipole. This case has a problem akin to that of linear BFKL evolution: if we increase the dipole size $x_\perp$ in Eq. (4.32), at some point we get $N_{LO} > 1$, violating the *black-disk limit*, which states that

$$N(\vec{x}_\perp, \vec{b}_\perp, Y) \leq 1 \tag{4.33}$$

(see Eq. (B.37) in Appendix B).

https://doi.org/10.1017/9781009291446.005 Published online by Cambridge University Press

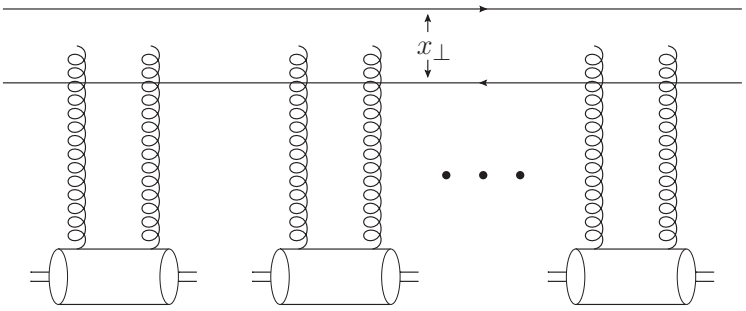

Fig. 4.5. Dipole–nucleus scattering in the Glauber–Gribov–Mueller approximation in the Feynman gauge. The disconnected gluon lines at the top denote the sum over all possible connections of the gluon lines to the dipole, as depicted in Fig. 4.3.

Let us stress again here that the transverse dipole size $x_\perp$ is preserved in high energy interactions. This makes the S-matrix diagonal not only in the impact parameter $\vec{b}_\perp$, as we saw in Eqs. (3.119) and also in Appendix B, but also in the dipole size $\vec{x}_\perp$. Therefore, the relations (3.119) between the cross sections and the S-matrix can also be written down for dipole–nucleus scattering with a fixed dipole size $\vec{x}_\perp$. The unitarity conditions (the optical theorem), which in momentum space are written as complicated convolutions (see e.g. Eq. (B.19)), become simple products of the amplitudes in $(\vec{x}_\perp, \vec{b}_\perp)$-space (see e.g. Eq. (B.30)). For this reason we think of color dipoles (or any other objects in the transverse coordinate representation) as the correct degrees of freedom for high energy scattering.

4.2.2 Scattering on many nucleons

When the probability of interaction with one nucleon becomes large, interactions with multiple nucleons also becomes likely and should be taken into account. Now we will see how multiple rescatterings of the dipole on different nucleons cure the problem of black-disk-limit violation by Eq. (4.32).

Let us consider the case when any number of nucleons can interact, restricting the interaction with each nucleon to the lowest nontrivial order. For this calculation we will be working in the standard Feynman perturbation theory using the Lorenz $\partial_\mu A^\mu = 0$ (Feynman) gauge. (Once we have separated the DIS cross section into the light cone wave function squared and the dipole–nucleus cross section, we can calculate the latter using any technique that is convenient.) We start by stating the diagrammatic answer for the many-nucleon interaction case: in the Feynman gauge, the dipole–nucleus interaction becomes a series of successive independent dipole–nucleon rescatterings, as shown in Fig. 4.5. There each nucleon (denoted by an oval at the bottom, just as in Fig. 4.3) interacts with the dipole via a two-gluon exchange: the disconnected gluon lines at the top of the diagram denote all possible connections to the quark and the antiquark lines in the dipole, as defined in Fig. 4.3.

The diagram in Fig. 4.5 implies that in the covariant gauge there is no direct "cross-talk" between the nucleons and that all the nucleons interact sequentially in the order in which

https://doi.org/10.1017/9781009291446.005 Published online by Cambridge University Press

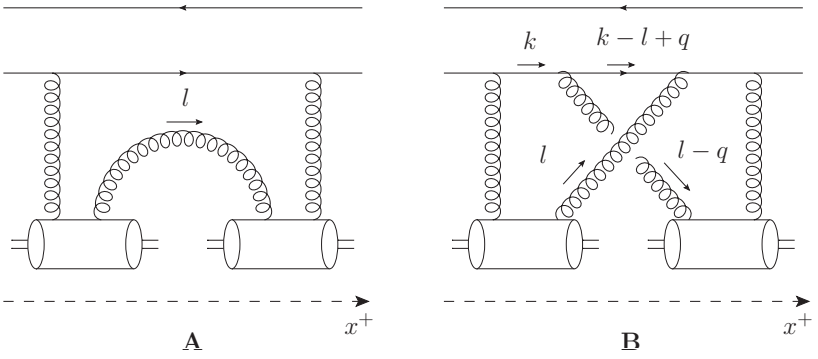

Fig. 4.6. Examples of diagrams that can be neglected for dipole–nucleus scattering in the covariant (Feynman) gauge.

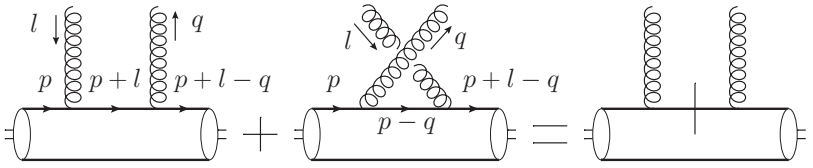

Fig. 4.7. Diagrammatic illustration that for a color-singlet object such as a nucleon, the coupling of two gluons to a single quark line is equivalent to the coupling of each gluon to a quark line that is on mass shell both before and after the quark–gluon interaction. The solid vertical line in the rightmost graph indicates an effective cut.

the dipole encounters them, i.e., according to their ordering along the x^+-axis. The dipole–nucleon interactions in the covariant gauge of Fig. 4.5 are localized inside the nucleons, on distance scales much shorter than the nuclear radius. While for a large dilute nucleus these assertions seem natural, we still need to prove them. To do so, it is convenient to change the frame slightly by giving the nucleus a slight boost, so that it moves along the light cone in the minus direction with a large P^- momentum. At the same time the boost preserves the virtual photon's motion along the plus light cone, with four-momentum as shown in Eq. (4.1). Thus both the dipole and nucleus in this new frame move along their respective light cones, as shown in Fig. 4.8. In the calculations below we will assume that the gluon–nucleon coupling is perturbatively small.

To illustrate why the graphs in Fig. 4.5 dominate the scattering, let us show that the diagrams in Fig. 4.6, demonstrating "cross-talk" (A) and the violation of x^+-ordering (B), are suppressed and can be neglected. Before we do that, let us carry out a simple exercise elucidating the nature of the coupling of two gluons to a nucleon. Consider two gluons coupling to a quark line in a nucleon, as shown in Fig. 4.7. This can be a part of any diagram in Figs. 4.6 and 4.5. Note that one has to include a crossed diagram, as illustrated in Fig. 4.7. Since the nucleon is a color singlet, the color factors of the two graphs on the left in Fig. 4.7 are identical (say, owing to a color trace), so that the difference between the two diagrams is only in the propagators for the internal quark line. Adding the two propagators (using the momentum labels from Fig. 4.7) and remembering that p^- is the largest momentum in the

https://doi.org/10.1017/9781009291446.005 Published online by Cambridge University Press

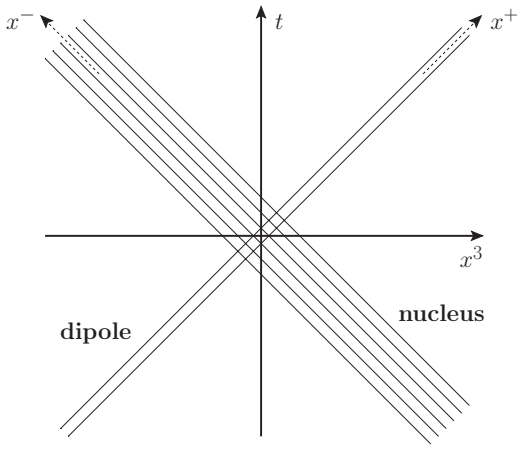

Fig. 4.8. Space–time picture of the dipole–nucleus scattering.

problem, we obtain

$$\frac{i(\not p + \not l + m_q)}{(p+l)^2 - m_q^2 + i\epsilon} + \frac{i(\not p - \not q + m_q)}{(p-q)^2 - m_q^2 + i\epsilon}$$
$$\approx i\not p \left(\frac{1}{p^- l^+ + i\epsilon} + \frac{1}{-p^- q^+ + i\epsilon} \right) = -i\not p 2\pi i \delta(p^- l^+). \tag{4.34}$$

We have used the fact that the outgoing quark is on mass shell, $(p + l - q)^2 = m_q^2$, so that $q^+ = l^+$ with eikonal accuracy (see Sec. 3.2 for similar estimates). We conclude that (with eikonal accuracy) $l^+ = q^+ = 0$. The δ-function in Eq. (4.34) puts the internal quark line in the leftmost diagram of Fig. 4.7 on mass shell. The result (4.34) can be summarized by replacing the internal quark line by the cut line, as shown in the rightmost graph of Fig. 4.7: the cut enforces $l^+ = 0$. What is essential to us is that neither gluon carries any plus momentum.

Now we are ready to evaluate the diagrams in Fig. 4.6. Note that, owing to the large size of the nucleus we are considering, even after the boost the nucleus is still somewhat spread out in the x^+-direction, as demonstrated in Fig. 4.8, where different nucleons correspond to different straight lines parallel to the x^- light cone. Hence each nucleon in the nucleus is located at a different x^+ coordinate. We thus need to Fourier-transform the diagrams in Fig. 4.6 into coordinate x^+-space by integrating over l^-.

Starting with Fig. 4.6A we see that the l^--dependence can be contained only in the propagator of the gluon carrying momentum l that is exchanged between the nucleons there. However, as we have just shown when considering the diagrams in Fig. 4.7, $l^+ = 0$ with eikonal accuracy, so that the diagram in Fig. 4.6A is proportional to

$$\int_{-\infty}^{\infty} dl^- \frac{e^{-il^-\Delta x^+}}{l^2 + i\epsilon} \approx \int_{-\infty}^{\infty} dl^- \frac{e^{-il^-\Delta x^+}}{-\vec{l}_\perp^2} = 0 \tag{4.35}$$

https://doi.org/10.1017/9781009291446.005 Published online by Cambridge University Press

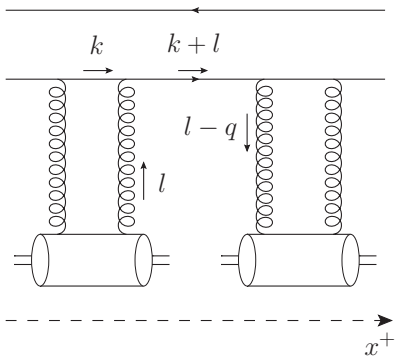

Fig. 4.9. Forward amplitude for a dipole scattering on two nucleons.

for nonzero light cone separations between the two nucleons, i.e., $\Delta x^+ \neq 0$. Hence diagram A is negligible in the covariant gauge in which we are working.[3] Let us stress that in arriving at the result (4.35) we have restricted ourselves to $l^- \ll p^-$: if we relaxed this constraint then the integral in Eq. (4.35) would be nonzero, though it would still be suppressed for large atomic numbers A (Kovchegov 1997).

Similarly, in Fig. 4.6B one has $l^+ = q^+ = 0$, so that the l^--dependence can be contained only in the quark propagator of the $(k - l + q)$-line. Since the light cone momentum of the quark k^+ is large, we see that the diagram in Fig. 4.6B is proportional to

$$\int\limits_{-\infty}^{\infty} dl^- \frac{e^{-il^-\Delta x^+}}{(k-l+q)^2 + i\epsilon} \approx \int\limits_{-\infty}^{\infty} dl^- \frac{e^{-il^-\Delta x^+}}{k^+(k^- - l^- + q^-) - (\vec{k}_\perp - \vec{l}_\perp + \vec{q}_\perp)^2 + i\epsilon} = 0 \tag{4.36}$$

for $\Delta x^+ > 0$, as the pole of the propagator is in the upper half-plane while the contour needs to be closed in the lower half-plane. For $\Delta x^+ < 0$ the integral in Eq. (4.36) is not zero, but then we would obtain zero from the integral over the minus momentum carried by the other pair of t-channel gluon lines. We thus can neglect diagram B as well.

The arguments used in proving that diagrams A and B in Fig. 4.6 are zero can be generalized to more complicated diagrams in the same general categories. We have succeeded in demonstrating that in the covariant gauge and in the approximation of two gluon exchanges per nucleon the dipole–nucleus interaction is given by the graphs in Fig. 4.5. We now need to resum these diagrams. To do this, we first consider dipole scattering on two nucleons ordered in x^+, as shown in Fig. 4.9. Unlike the diagram in Fig. 4.6B, the graph in Fig. 4.9 has the correct x^+-ordering of the nucleons. Instead of giving zero it yields (note that k^- is very small for a quark on a plus light cone)

$$\int\limits_{-\infty}^{\infty} \frac{dl^-}{2\pi} \frac{ie^{-il^-\Delta x^+}}{(k+l)^2 + i\epsilon} \approx \int\limits_{-\infty}^{\infty} \frac{dl^-}{2\pi} \frac{ie^{-il^-\Delta x^+}}{k^+l^- - (\vec{k}_\perp + \vec{l}_\perp)^2 + i\epsilon} = \frac{1}{k^+}, \tag{4.37}$$

[3] Note that the diagram in Fig. 4.6A is nonzero in the $A^- = 0$ light cone gauge even in the eikonal approximation.

https://doi.org/10.1017/9781009291446.005 Published online by Cambridge University Press

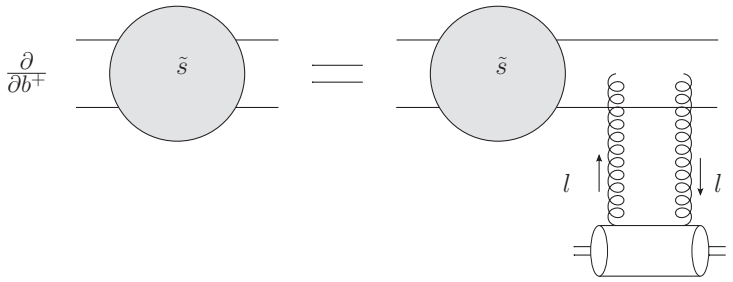

Fig. 4.10. Diagrammatic representation of Eq. (4.40) resumming all the diagrams from Fig. 4.5.

where at the end of the calculation we have neglected the phase of the exponential since it is proportional to $\Delta x^+/k^+ \sim 1/(k^+p^-)$, which is suppressed by the center-of-mass energy. It is important to note that in picking up the pole in Eq. (4.37) we put the propagator of the quark carrying momentum $k+l$ on mass shell. Therefore, the diagram factorizes into a product of two independent dipole–nucleon scatterings; the quark and the antiquark in the dipole effectively go on shell between the scatterings. (The factor $1/k^+$ left in Eq. (4.37) serves to normalize the dipole–nucleon cross section for the nucleon on the right.) The numerator of the quark propagator can be absorbed into two separate scattering amplitudes using the property that (neglecting the quark mass) $\not{k}+\not{l} = \sum_\sigma u_\sigma(k+l)\bar{u}_\sigma(k+l)$: the factor $u_\sigma(k+l)$ is absorbed into one amplitude, while $\bar{u}_\sigma(k+l)$ is absorbed into the other. Comparing this result with the standard normalization factor for the $2 \to 2$ cross section at high energy (see Eqs. (B.22) and (B.23)), we conclude that to resum the diagrams in Fig. 4.5 we simply need to iterate the dipole–nucleus cross section.

Define the forward matrix element of the S-matrix for the dipole–nucleus scattering by (cf. Eq. (B.34))

$$S(\vec{x}_\perp, \vec{b}_\perp, Y) = 1 - N(\vec{x}_\perp, \vec{b}_\perp, Y). \tag{4.38}$$

Suppressing the arguments $\vec{b}_\perp$ and Y, we can define the S-matrix (the "propagator") $s(\vec{x}_\perp, b^+)$ for a dipole to travel through the nucleus up to a point b^+, so that $S(\vec{x}_\perp) = s(\vec{x}_\perp, L)$ with $b^+ \in (0, L)$, which defines the extent of the nucleus along the x^+ axis. Going to transverse momentum space we have

$$\tilde{s}(\vec{k}_\perp, b^+) = \int d^2x_\perp e^{-i\vec{k}_\perp\cdot\vec{x}_\perp} s(\vec{x}_\perp, b^+), \tag{4.39}$$

with $\vec{k}_\perp$ the relative transverse momentum of the quark and the antiquark in the dipole. As we demonstrated above, all the integrations over the minus momenta in the diagrams in Fig. 4.5 are done straightforwardly. Hence the b^+-evolution of $\tilde{s}(\vec{k}_\perp, b^+)$ is also clear: in one step in b^+ the dipole may interact with one nucleon. Denoting $\tilde{s}(\vec{k}_\perp, b^+)$ by a circle, we illustrate this statement in Fig. 4.10.

https://doi.org/10.1017/9781009291446.005 Published online by Cambridge University Press

Summing over all possible connections of the t-channel gluons to the dipole in Fig. 4.10 we obtain the following equation (Mueller (1990), see also Baier *et al.* (1997)):

$$\frac{\partial \tilde{s}(\vec{k}_\perp, b^+)}{\partial b^+} = -\frac{\rho_A(\vec{b}_\perp, b^+)}{2} \int \frac{d^2 l_\perp}{(2\pi)^2} \frac{d\sigma^0_{qq\to qq}}{d^2 l} \times \left[2\,\tilde{s}(\vec{k}_\perp, b^+) - \tilde{s}(\vec{k}_\perp - \vec{l}_\perp, b^+) - \tilde{s}(\vec{k}_\perp + \vec{l}_\perp, b^+) \right], \tag{4.40}$$

where the minus signs outside the last two terms come from the coupling of one gluon to the quark and the other to the antiquark. The differential cross section $d\sigma^0_{qq\to qq}/d^2 l$ is the momentum-space expression for the two-gluon exchange cross section in quark–quark scattering, as given in Eq. (3.18), and the factor $1/2$ is needed to convert it to the forward amplitude. (Again we are modeling the nucleons as single valence quarks.) The nucleon density factor $\rho_A(\vec{b}_\perp, b^+)$ (now, in the boosted-nucleus frame, equal to the number of nucleons per unit volume element $db^+ d^2 b_\perp$) gives the probability of finding a nucleon at a given location in the nucleus. Again we assume $\rho_A(\vec{b}_\perp, b^+)$ to be constant on the perturbatively short transverse distance scales relevant to Eq. (4.40). The overall minus sign in Eq. (4.40) reflects the fact that we are calculating a variation of the S-matrix that differs from the variation of the forward amplitude by a sign, as follows from Eq. (4.38).

Fourier-transforming Eq. (4.40) into transverse coordinate space we obtain

$$\frac{\partial s(\vec{x}_\perp, b^+)}{\partial b^+} = -\frac{\rho_A(\vec{b}_\perp, b^+)}{2}\, \sigma^{q\bar{q}N} s(\vec{x}_\perp, b^+), \tag{4.41}$$

$$\sigma^{q\bar{q}N} = \int \frac{d^2 l_\perp}{(2\pi)^2} \frac{d\sigma^0_{qq\to qq}}{d^2 l} \left(2 - e^{i\vec{l}_\perp \cdot \vec{x}_\perp} - e^{-i\vec{l}_\perp \cdot \vec{x}_\perp} \right), \tag{4.42}$$

exactly the dipole–nucleus cross section of Eqs. (4.25) and (4.28). (The factor 2 difference in comparison to Eq. (4.25) is due to the fact that in Eq. (4.25) the nucleon is modeled as a dipole whereas in our present calculation it is taken to be a single quark for simplicity.)

One can readily see from Eq. (4.41) that in transverse coordinate space Eq. (4.40) becomes trivial. An important consequence of this triviality is that, for the first time, we see explicitly that the transverse size of the dipole $x_\perp$ does not change in the interactions with the nucleons (and the nucleus). This demonstrates the argument presented in Sec. 4.1.

Equation (4.41) has the following simple physical meaning: as the dipole propagates through the nucleus it may encounter nucleons, with the probability of interaction per unit path length db^+ given by the product of the nucleon density ρ_A and the interaction probability $\sigma^{q\bar{q}N}$ from Eq. (4.28), with another factor one-half inserted owing to the optical theorem (B.23). The initial condition for Eq. (4.41) is given by a freely propagating dipole without interactions, for which $s(\vec{x}_\perp, b^+ = 0) = 1$. Solving Eq. (4.41) with this initial condition yields

$$s(\vec{x}_\perp, b^+) = \exp\left\{ -\int_0^{b^+} db'^+ \frac{\rho_A(\vec{b}_\perp, b'^+)}{2} \sigma^{q\bar{q}N} \right\}. \tag{4.43}$$

https://doi.org/10.1017/9781009291446.005 Published online by Cambridge University Press

Going back to the nuclear rest frame and remembering that $S(\vec{x}_\perp) = s(\vec{x}_\perp, L)$, we obtain

$$S(\vec{x}_\perp, \vec{b}_\perp, Y = 0) = \exp\left\{-\frac{\sigma^{q\bar{q}N}}{2} T(\vec{b}_\perp)\right\}. \tag{4.44}$$

Note that $\sigma^{q\bar{q}N}$ does not depend on the energy of the collision (and therefore on its net rapidity): to underscore this we have put $Y = 0$ in the argument of the S-matrix in Eq. (4.44). This will delineate this expression from the energy-dependent version that results from incorporating small-x evolution into this picture.

Using Eq. (4.44) along with Eq. (4.28) in Eq. (4.38), the imaginary part of the forward scattering amplitude in the Glauber–Gribov–Mueller (GGM) model (Mueller 1990) is given by

$$N(\vec{x}_\perp, \vec{b}_\perp, Y = 0) = 1 - \exp\left\{-\frac{\alpha_s \pi^2}{2N_c} T(\vec{b}_\perp)\, x_\perp^2 x G_N\left(x, \frac{1}{x_\perp^2}\right)\right\}. \tag{4.45}$$

This is the GGM multiple–rescattering formula. Note again that the nucleon's gluon distribution function xG_N in Eq. (4.45) is taken at the lowest, two-gluon, level and is thus independent of x, so that the amplitude N in Eq. (4.45) is independent of energy.

Equation (4.45) has a remarkable property: one can see that it implies $N \leq 1$ for all (perturbative) $x_\perp$. This means that the resulting forward scattering amplitude obeys the black-disk limit constraint (4.33), correcting the problem of the single rescattering amplitude from Eq. (4.32). We see that multiple rescatterings unitarize the scattering cross section, preserving the black-disk limit. The lesson we learn from the Glauber–Gribov–Mueller model is that to unitarize a cross section it is important to include multiple rescatterings!

Equation (4.45) allows us to determine the parameter corresponding to resummation of the diagrams like that shown in Fig. 4.5. Using the gluon distribution from Eq. (4.27) in Eq. (4.45), and noting that for large nuclei the profile function $T(\vec{b}_\perp)$ scales as $A^{1/3}$, we conclude that the resummation parameter of multiple rescatterings is (Kovchegov 1997)

$$\alpha_s^2 A^{1/3}. \tag{4.46}$$

The physical meaning of the parameter $\alpha_s^2 A^{1/3}$ is rather straightforward: at a given impact parameter the dipole interacts with $\sim A^{1/3}$ nucleons, exchanging two gluons with each. Since two-gluon exchange is parametrically of order α_s^2 we obtain $\alpha_s^2 A^{1/3}$ as the resummation parameter.

4.2.3 Saturation picture from the GGM formula

Multiple nucleon interactions become important in Eq. (4.45) when the dipole size becomes of order $x_\perp \sim 1/Q_s$, where the *saturation* scale Q_s is defined by the following implicit equation (cf. Eq. (3.133)):

$$Q_s^2(\vec{b}_\perp) = \frac{\alpha_s \pi^2}{2N_c} T(\vec{b}_\perp) x G_N(x, Q_s^2). \tag{4.47}$$

Note that for a cylindrical nucleus, as considered in Sec. 3.4.2, one has $T(\vec{b}_\perp) = A/S_\perp$ so that, taking into account that the nuclear gluon distribution is $xG_A = A x G_N$ (which is

https://doi.org/10.1017/9781009291446.005 Published online by Cambridge University Press

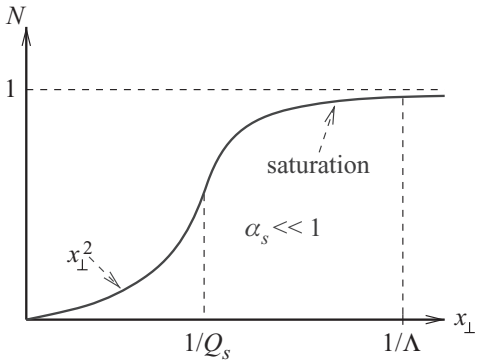

Fig. 4.11. The imaginary part of the forward amplitude of the dipole–nucleus scattering N plotted as a function of the transverse separation between the quark and the anti-quark in a dipole $x_\perp$, using Eq. (4.51). (Reprinted from Jalilian-Marian and Kovchegov (2006), with permission from Elsevier.) A color version of this figure is available online at www.cambridge.org/9780521112574.

true at the two-gluon level considered here), one can recast Eq. (4.47) in almost the exact form of Eq. (3.133). The difference N_c/C_F between the saturation scales in (4.47) and in (3.133) is due to the fact that the saturation scale (4.47) we have just found is that for a quark dipole, whereas the saturation scale in Eq. (3.133) was obtained solely for gluons. If we were to replace the quark dipole in Fig. 4.5 with a gluon dipole, we would need to modify the exponent in Eq. (4.45) by the ratio of the adjoint and fundamental Casimir operators N_c/C_F, putting Eq. (4.47) in exact agreement with Eq. (3.133). With this proviso, we see that, at least at the lowest order considered, Eq. (4.47) gives the same saturation scale as what follows from the GLR–MQ equation.

Inserting the lowest-order single-quark gluon distribution function,

$$xG_{LO}^{quark}(x, Q_\perp^2) = \frac{\alpha_s C_F}{\pi} \ln \frac{Q^2}{\Lambda^2}, \tag{4.48}$$

into Eq. (4.45), we can rewrite it as

$$N(\vec{x}_\perp, \vec{b}_\perp, Y = 0) = 1 - \exp\left\{-\frac{\alpha_s^2 C_F \pi}{N_c} T(\vec{b}_\perp)\, x_\perp^2 \ln \frac{1}{x_\perp \Lambda}\right\}. \tag{4.49}$$

Defining the quark *saturation* scale (note the factor 4 difference compared with Eq. (4.47) and the absence of a gluon distribution in this definition),

$$Q_s^2(\vec{b}_\perp) \equiv \frac{4\pi\alpha_s^2 C_F}{N_c} T(\vec{b}_\perp), \tag{4.50}$$

we rewrite Eq. (4.49) as

$$N(\vec{x}_\perp, \vec{b}_\perp, Y = 0) = 1 - \exp\left\{-\frac{x_\perp^2 Q_s^2(\vec{b}_\perp)}{4} \ln \frac{1}{x_\perp \Lambda}\right\}. \tag{4.51}$$

The dipole amplitude N from Eq. (4.51) is plotted schematically in Fig. 4.11 as a function of $x_\perp$. One can see that, at small $x_\perp$, i.e., $x_\perp \ll 1/Q_s$, we have $N \sim x_\perp^2$ so that the amplitude

https://doi.org/10.1017/9781009291446.005 Published online by Cambridge University Press

is zero for zero dipole size. This result is natural, since in a zero-size dipole the color charges of the quark and the antiquark cancel each other, leading to the disappearance of interactions with the target. This effect is known as *color transparency* (Kopeliovich, Lapidus, and Zamolodchikov 1981, Nikolaev and Zakharov 1991, Heiselberg *et al.* 1991, Blaettel *et al.* 1993, Frankfurt, Miller, and Strikman 1993).

The amplitude (4.51) is a rising function of $x_\perp$ at small dipole size. However, at large dipole size $x_\perp \gtrsim 1/Q_s$, growth stops and the amplitude levels off (*saturates*) at $N = 1$. As mentioned earlier, this regime corresponds to the black-disk limit for dipole–nucleus scattering: for large dipoles the nucleus appears as a black disk. The transition from $N \sim x_\perp^2$ to the black disk-like ($N = 1$) behavior in Fig. 4.11 occurs at around $x_\perp \sim 1/Q_s$. For dipole sizes $x_\perp \gtrsim 1/Q_s$ the amplitude N *saturates* to a constant. This translates into saturation of the quark distribution functions in the nucleus, since $xq + x\bar{q} \sim F_2$ (see Eq. (2.46)) and the saturation of N implies the saturation of F_2, as follows from Eqs. (4.10a), (4.12), and (4.24). Thus the saturation of N can be identified with parton saturation, justifying the name *saturation scale* for Q_s, Eq. (4.50).

Note that since $T(\vec{b}_\perp) \sim A^{1/3}$ the saturation scale grows as

$$Q_s^2 \sim A^{1/3} \tag{4.52}$$

with atomic number A. If A is large enough, Q_s becomes perturbatively large, $Q_s \gg \Lambda_{QCD}$, justifying the use of perturbation theory. The scaling in Eq. (4.52) is consistent with Eq. (3.135), which we obtained from analyzing the GLR equation.

4.3 Mueller's dipole model

The amplitude N given by the Glauber–Gribov–Mueller formula (4.51) is independent of the energy of the collision (see also Eq. (4.49)) and therefore cannot be the final answer for the high energy scattering problem at hand. It turns out that the energy dependence comes into the dipole–nucleus scattering amplitude through quantum evolution corrections, much as the two-gluon exchange amplitude in the onium–onium scattering in Sec. 3.2 acquires energy dependence through the BFKL evolution of Sec. 3.3. To incorporate small-x evolution into dipole–nucleus scattering we begin by rewriting the evolution in the language of LCPT, in which it can be completely absorbed into the light cone wave function, with the help of Mueller's dipole model (Mueller 1994, 1995, Mueller and Patel 1994).

4.3.1 Dipole wave function and generating functional

Let us consider the light cone wave function of an ultrarelativistic meson consisting of a heavy quark and antiquark (an onium), with no sea quarks and gluons present before the small-x evolution, as shown in Fig. 4.12. We can safely apply perturbative QCD to the onium wave function since here typical transverse distance $x_\perp$ is about $1/m_Q$, where m_Q is the large mass of the heavy quark; the strong coupling constant is clearly small at such distances.

We will denote the "bare" onium light cone wave function by $\Psi^{(0)}_{\sigma\sigma'}(\vec{k}_\perp, z)$, where $\vec{k}_\perp$ is the relative transverse momentum of the $q\bar{q}$ pair, $z = k^+/p^+$ is the fraction of the light cone momentum p^+ of the whole onium carried by the quark, while σ and σ' are the

https://doi.org/10.1017/9781009291446.005 Published online by Cambridge University Press

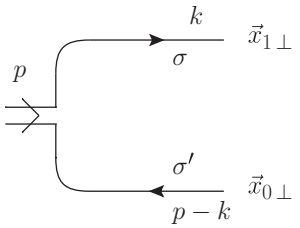

Fig. 4.12. The onium light cone wave function before small-x evolution.

polarizations of the quark and the antiquark (see Fig. 4.12). The onium is moving in the light cone plus direction. As usual we suppress the color and flavor indices, assuming that they will be properly summed over when necessary. As we will shortly see, the transverse size of the dipole remains invariant during the small-x evolution: therefore we will work in a mixed representation where we use the transverse coordinates and longitudinal momenta to describe dipoles. We thus Fourier-transform the onium wave function, using

$$\Psi^{(0)}_{\sigma\sigma'}(\vec{x}_{10}, z) = \int \frac{d^2k_\perp}{(2\pi)^2} e^{i\vec{k}_\perp\cdot\vec{x}_{10}} \Psi^{(0)}_{\sigma\sigma'}(\vec{k}_\perp, z), \tag{4.53}$$

where $\vec{x}_{10\perp} = \vec{x}_{1\perp} - \vec{x}_{0\perp}$ is the transverse size of dipole, the quark being located at $\vec{x}_{1\perp}$ and the antiquark at $\vec{x}_{0\perp}$ (see Fig. 4.12).

As the initial onium state contains only the $q\bar{q}$ pair its normalization is (cf. Eqs. (1.70) and (1.82))

$$\int_0^1 \frac{dz}{z(1-z)} \int \frac{d^2k_\perp}{2(2\pi)^3} \sum_{\sigma,\sigma'} \left|\Psi^{(0)}_{\sigma\sigma'}(\vec{k}_\perp, z)\right|^2 = 1, \tag{4.54}$$

which, in transverse coordinate space becomes

$$\int_0^1 \frac{dz}{z(1-z)} \int \frac{d^2x_{10}}{4\pi} \sum_{\sigma,\sigma'} \left|\Psi^{(0)}_{\sigma\sigma'}(\vec{x}_{10}, z)\right|^2 = 1. \tag{4.55}$$

We are interested in modifications to this wave function under small-x evolution in the LLA approximation; thus we need to resum the terms containing $\alpha_s \ln 1/x$ corrections. Throughout this section we will work in the $A^+ = 0$ light cone gauge. As for the DGLAP evolution of Sec. 2.4.2, one step of LLA small-x evolution consists of the appearance of a single gluon in the wave function: the gluon can be emitted either from the quark line or from the antiquark line, as shown in Fig. 4.13. (Just as in the case of BFKL evolution, quark loops and the emission of $q\bar{q}$ pairs are beyond the LLA, contributing subleading corrections of order $\alpha_s^2 \ln 1/x$.) The corresponding modification of the onium wave function due to the gluon emissions in Fig. 4.13 is easier to calculate than in the DGLAP case. We assume that the light cone momentum k_2^+ of the emitted gluon is small, $k_2^+ \ll k_1^+, p^+ - k_1^+$ (see

https://doi.org/10.1017/9781009291446.005 Published online by Cambridge University Press

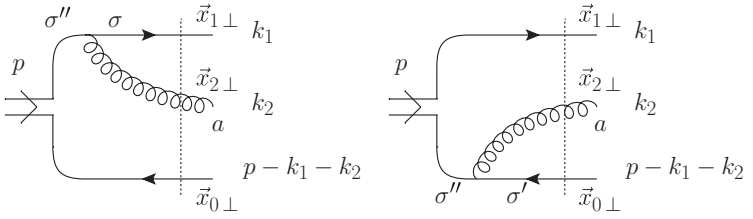

Fig. 4.13. One step of small-x evolution in the onium wave function. The dotted lines denote the intermediate states.

Fig. 4.13 for the explanation of the momentum and coordinate labeling). At the same time we impose no ordering on the transverse momenta of the quarks and the gluon. The kinematics is different from the DGLAP case (cf. Sec. 2.4.2): here the longitudinal momenta are ordered while in the DGLAP case the transverse momenta were ordered. In analogy with Eq. (2.68), we can write down the following expression for the $q\bar{q}G$ (one-gluon) contribution to the onium light cone wave function in the $A^+ = 0$ gauge at order g:

$$\begin{aligned}
&\Psi^{(1)}_{\sigma\sigma'}(\vec{k}_{1\perp}, \vec{k}_{2\perp}, z_1, z_2) \\
&\quad = \frac{g t^a \theta(k_2^+)}{k_2^- + k_1^- + (p-k_1-k_2)^- - p^-} \\
&\qquad \times \sum_{\sigma''=\pm 1} \left[\frac{\bar{u}_\sigma(k_1) \gamma \cdot \epsilon^*_\lambda(k_2) u_{\sigma''}(k_1+k_2)}{k_1^+ + k_2^+} \, \Psi^{(0)}_{\sigma''\sigma'}(\vec{k}_{1\perp} + \vec{k}_{2\perp}, z_1 + z_2) \right. \\
&\qquad\qquad \left. - \frac{\bar{v}_{\sigma''}(p-k_1) \gamma \cdot \epsilon^*_\lambda(k_2) v_{\sigma'}(p-k_1-k_2)}{p^+ - k_1^+} \, \Psi^{(0)}_{\sigma\sigma''}(\vec{k}_{1\perp}, z_1) \right].
\end{aligned} \tag{4.56}$$

Here a is the gluon color index, σ, σ', and σ'' are the quark and antiquark polarizations, and λ is the gluon polarization, while $z_2 = k_2^+/p^+$ and $z_1 = k_1^+/p^+$.

To simplify Eq. (4.56) we first remember that we have assumed that $k_2^+ \ll k_1^+, \, p^+ - k_1^+$ (that is $z_2 \ll z_1, \, 1 - z_1$) and that all the transverse momenta are comparable. In this kinematics the light cone energy of the gluon, $k_2^- = k_{2\perp}^2/k_2^+$, dominates the energy denominator, just as in the DGLAP case (cf. Eq. (2.69)), only now this is due to longitudinal momentum ordering. We can write

$$\frac{1}{k_2^- + k_1^- + (p-k_1-k_2)^- - p^-} \approx \frac{1}{k_2^-} = \frac{k_2^+}{k_{2\perp}^2}. \tag{4.57}$$

To evaluate the Dirac matrix elements in Eq. (4.56) we use Table A.1 along with Eq. (A.2), again keeping in mind that $k_2^+ \ll k_1^+, \, p^+ - k_1^+$. For instance, the first matrix element in the

https://doi.org/10.1017/9781009291446.005 Published online by Cambridge University Press

square brackets of Eq. (4.56) simplifies to

$$\bar{u}_\sigma(k_1)\gamma\cdot\epsilon^*_\lambda(k_2)u_{\sigma''}(k_1+k_2)\approx\frac{1}{2}\bar{u}_\sigma(k_1)\gamma^+u_{\sigma''}(k_1+k_2)\,\epsilon^-_\lambda(k_2)^*$$
$$=2\delta_{\sigma\sigma''}\sqrt{k_1^+(k_1^++k_2^+)}\,\frac{\vec{\epsilon}^{\,\lambda*}_\perp\cdot\vec{k}_{2\perp}}{k_2^+}\approx 2\delta_{\sigma\sigma''}k_1^+\frac{\vec{\epsilon}^{\,\lambda*}_\perp\cdot\vec{k}_{2\perp}}{k_2^+}. \tag{4.58}$$

Performing a similar approximation for the second matrix element in Eq. (4.56) and inserting the result along with Eqs. (4.57) and (4.58) back into Eq. (4.56) yields

$$\Psi^{(1)}_{\sigma\sigma'}(\vec{k}_{1\perp},\vec{k}_{2\perp},z_1,z_2)$$
$$\approx 2gt^a\theta(z_2)\frac{\vec{\epsilon}^{\,\lambda*}_\perp\cdot\vec{k}_{2\perp}}{k^2_{2\perp}}\left[\Psi^{(0)}_{\sigma\sigma'}(\vec{k}_{1\perp}+\vec{k}_{2\perp},z_1)-\Psi^{(0)}_{\sigma\sigma'}(\vec{k}_{1\perp},z_1)\right], \tag{4.59}$$

where we have also neglected z_2 in comparison with z_1 in the argument of one wave function.

In the transverse coordinate space representation, Eq. (4.59) has the form

$$\Psi^{(1)}_{\sigma\sigma'}(\vec{x}_{10},\vec{x}_{20},z_1,z_2)=\int\frac{d^2k_{1\perp}d^2k_{2\perp}}{(2\pi)^4}e^{i\vec{k}_{1\perp}\cdot\vec{x}_{10}+i\vec{k}_{2\perp}\cdot\vec{x}_{20}}\Psi^{(1)}_{\sigma\sigma'}(\vec{k}_{1\perp},\vec{k}_{2\perp},z_1,z_2)$$
$$=i\frac{gt^a}{\pi}\Psi^{(0)}_{\sigma\sigma'}(\vec{x}_{10},z_1)\,\vec{\epsilon}^{\,\lambda*}_\perp\cdot\left(\frac{\vec{x}_{21}}{x^2_{21}}-\frac{\vec{x}_{20}}{x^2_{20}}\right), \tag{4.60}$$

where $\vec{x}_{20}=\vec{x}_{2\perp}-\vec{x}_{0\perp}$, $\vec{x}_{21}=\vec{x}_{2\perp}-\vec{x}_{1\perp}$, and $x_{ij}=|\vec{x}_{ij}|$ as defined after Eq. (1.87). The gluon has transverse coordinate $\vec{x}_{2\perp}$, as illustrated in Fig. 4.13. We have used Eq. (A.10) to obtain Eq. (4.60) from Eq. (4.59).

Squaring the coordinate-space one-gluon wave function from Eq. (4.60) and summing over the quark and gluon polarizations and colors yields

$$\sum_{\sigma,\sigma',\lambda,a}\left|\Psi^{(1)}_{\sigma\sigma'}\right|^2=\frac{4\alpha_sC_F}{\pi}\frac{x^2_{10}}{x^2_{20}x^2_{21}}\sum_{\sigma,\sigma'}\left|\Psi^{(0)}_{\sigma\sigma'}\right|^2. \tag{4.61}$$

To calculate the probability of finding one extra gluon in the onium wave function we have to integrate Eq. (4.61) over the gluon's phase space, which, in the $z_2\ll z_1$, $1-z_1\ll 1$ approximation, is (cf. Eq. (4.23))[4]

$$\int_{z_0}^{\min\{z_1,1-z_1\}}\frac{dz_2}{z_2}\int\frac{d^2x_2}{4\pi}, \tag{4.62}$$

where z_0 is some lower cutoff on the z_2-integral, imposed to make the integration finite; the exact value of z_0 depends on the physical process incorporating to the wave function we are constructing. The order-α_s contribution to the probability of finding one gluon in

[4] One may ask why, if our calculation is valid for $z_2\ll z_1$, $1-z_1$, we can extend the z_2-integral all the way up to z_1 or $1-z_1$. While indeed our approximation breaks down for z_2 close to z_1 or $1-z_1$, putting z_1 or $1-z_1$ as the upper integration limit gives the correct leading-logarithmic contribution.

https://doi.org/10.1017/9781009291446.005 Published online by Cambridge University Press

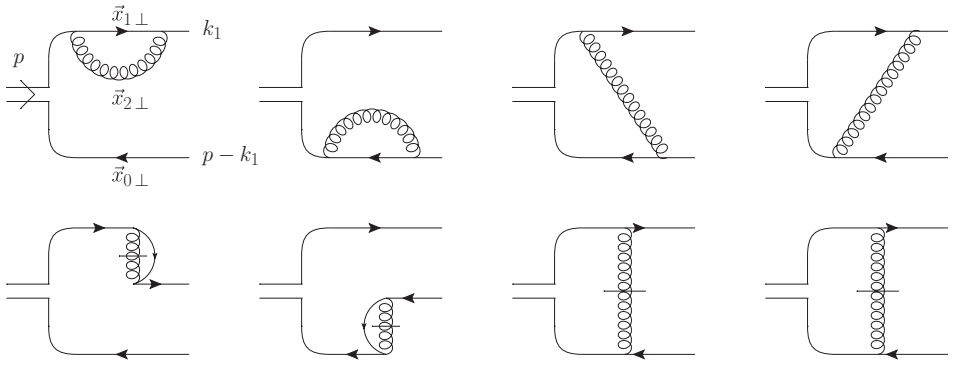

Fig. 4.14. Virtual contribution to small-x evolution in the onium wave function. The quark transverse coordinates in the onium are not changed by the corrections.

the onium wave function is then (Mueller 1994)

$$\int\limits_{z_0}^{\min\{z_1,1-z_1\}} \frac{dz_2}{z_2} \int \frac{d^2x_2}{4\pi} \sum_{\sigma,\sigma',\lambda,a} \left|\Psi^{(1)}_{\sigma\sigma'}\right|^2 = \int\limits_{z_0}^{\min\{z_1,1-z_1\}} \frac{dz_2}{z_2} \int d^2x_2 \frac{\alpha_s C_F}{\pi^2} \frac{x_{10}^2}{x_{20}^2 x_{21}^2} \sum_{\sigma,\sigma'} \left|\Psi^{(0)}_{\sigma\sigma'}\right|^2 . \tag{4.63}$$

Note that the modified wave function in Eq. (4.63) contains a power of α_s and a logarithmic integral over z_2, which would give us finally $\ln 1/x$. We see that the modification we have calculated brings in a factor $\alpha_s \ln 1/x$. Another feature of Eq. (4.63) is that the $\vec{x}_{2\perp}$-integral in it contains UV divergences at $x_{20} \approx 0$ and $x_{21} \approx 0$. For now we will regulate these divergences by a UV cutoff ρ, such that $x_{20}, x_{21} > \rho$: in the end no physical quantity depends on the value of this cutoff.

Before we proceed let us point out that, as for the Glauber–Gribov–Mueller model (see e.g. Eq. (4.41)), the expression (4.63) completely factorizes transverse coordinate space into the square of the "bare" onium wave function times the probability of emission of the extra gluon. The emission of an extra gluon does not change the coordinates of the initial quark and the antiquark, yet again illustrating our above argument about the convenience of the transverse coordinate representation. This property also gives Eq. (4.61) a very simple physical meaning, resulting from the probabilistic interpretation of the light cone wave functions: the contribution to the onium wave function due to the emission of an extra gluon is equal to the product of the probability of finding a dipole with size x_{10} inside the onium ($\sim |\Psi^{(0)}_{\sigma\sigma'}|^2$) multiplied by the probability that the dipole emits a gluon at $\vec{x}_{2\perp}$.

The one-gluon corrections to the dipole wave function need not be limited to the "real" gluon shown in Fig. 4.13; they should also include virtual corrections, where the gluon is both emitted and absorbed in the onium wave function, again like in the DGLAP case in Sec. 2.4.2. The virtual diagrams giving the LLA contributions are shown in Fig. 4.14, where, in accordance with the LCPT rules introduced in Sec. 1.3, the crossed lines denote instantaneous terms. From the sheer number of graphs in Fig. 4.14 one can see that direct calculation of all the virtual corrections can be a daunting task (see Chen and Mueller

https://doi.org/10.1017/9781009291446.005 Published online by Cambridge University Press

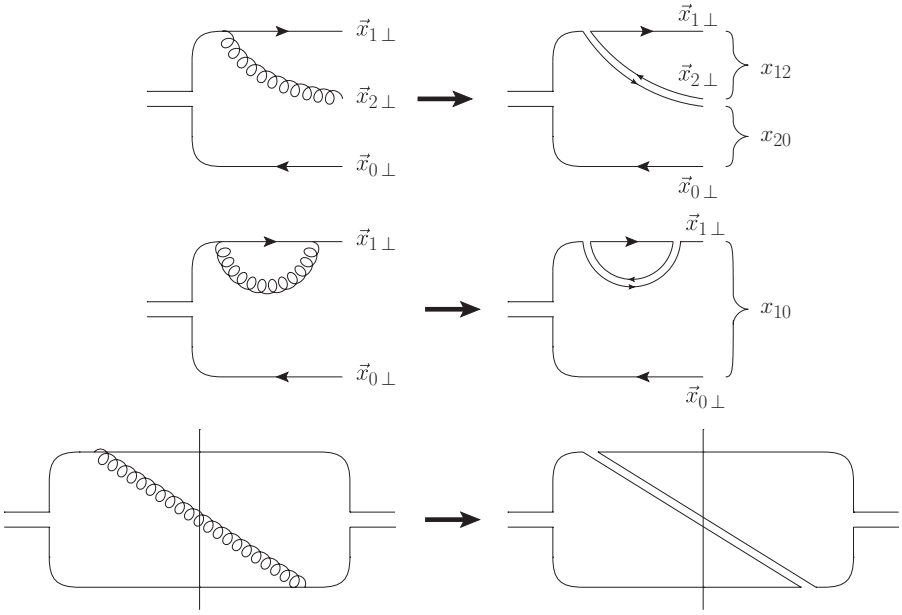

Fig. 4.15. Large-N_c limit in the onium wave function (top two panels) and the wave function squared (bottom panel). The curly brackets in the top panel denote the daughter dipoles generated by the gluon emission. The right-hand brace in the middle panel denotes the parent dipole remaining intact after a virtual correction. The thin vertical line in the bottom panel separates the wave function from its complex conjugate.

(1995) for an outline of the calculation). Instead we will follow Mueller (1994) and use the unitarity argument presented in Sec. 2.4.2 (see Eq. (2.86)) to write down the following expression for the order-α_s virtual correction to the onium wave function:

$$\Psi^{(0)}_{\sigma\sigma'}(\vec{x}_{10}, z_1)\Big|_{O(\alpha_s)} = -\frac{1}{2}\int_{z_0}^{\min\{z_1,1-z_1\}} \frac{dz_2}{z_2}\int d^2x_2 \frac{\alpha_s C_F}{\pi^2}\frac{x_{10}^2}{x_{20}^2 x_{21}^2}\,\Psi^{(0)}_{\sigma\sigma'}(\vec{x}_{10}, z_1)\Big|_{O(\alpha_s^0)}$$

$$= -\frac{2\alpha_s C_F}{\pi}\ln\frac{x_{01}}{\rho}\int_{z_0}^{\min\{z_1,1-z_1\}}\frac{dz_2}{z_2}\,\Psi^{(0)}_{\sigma\sigma'}(\vec{x}_{10}, z_1)\Big|_{O(\alpha_s^0)}. \qquad (4.64)$$

The integral over $\vec{x}_{2\perp}$ is carried out in appendix section A.3 with ρ the UV regulator introduced above.

Having obtained the one-gluon corrections we would now like to derive an equation resumming the higher-order gluon emissions and virtual gluon corrections that bring powers of $\alpha_s \ln 1/x$ into the wave function. (Remember that quark loops do not contribute leading logarithms of x.) This turns out to be a rather difficult problem. A major simplification occurs if we consider the onium wave function in the 't Hooft large-N_c limit ('t Hooft 1974), taking N_c to be very large while keeping $\alpha_s N_c$ constant. In the large-N_c limit the single gluon line is replaced by a double line, corresponding to replacing the gluon by a quark–antiquark pair in the color-octet configuration. This is illustrated in Fig. 4.15. In the

https://doi.org/10.1017/9781009291446.005 Published online by Cambridge University Press

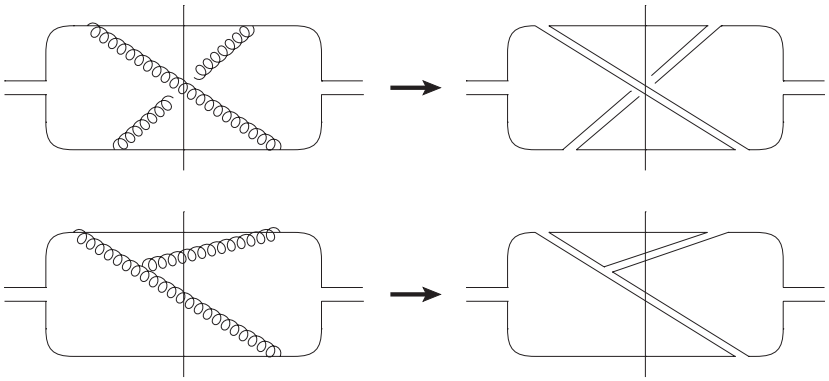

Fig. 4.16. Two steps of small-x evolution in the onium wave function squared (left) and their large-N_c limits (right). The top panel shows a nonplanar diagram, which is N_c^2-suppressed compared with the leading-N_c planar diagram shown in the bottom panel.

large-N_c limit it is convenient to talk about color dipoles instead of gluons. The original onium is a color dipole consisting of a quark at $\vec{x}_{1\perp}$ and an antiquark at $\vec{x}_{0\perp}$. The emission of a gluon in the onium wave function, taken in the large-N_c limit, corresponds to the splitting of the original dipole with size x_{10} into two dipoles with sizes x_{12} and x_{20}: the dipole the size x_{12} consists of the original quark at $\vec{x}_{1\perp}$ and the antiquark part of the gluon line at $\vec{x}_{2\perp}$, while the quark part of the gluon line at $\vec{x}_{2\perp}$ along with the original antiquark at $\vec{x}_{0\perp}$ form the dipole with size x_{20} (see the top and bottom panels of Fig. 4.15). The virtual gluon corrections leave the original dipole intact, as can be seen in the middle panel of Fig. 4.15.

Another important feature of the large-N_c limit is that only *planar diagrams* contribute; the nonplanar diagrams are suppressed by powers of N_c for fixed $\alpha_s N_c$. This means that different color dipoles generated by gluon emissions do not "talk" to each other: subsequent emissions happen independently in each dipole. This is illustrated in Fig. 4.16, where in the top panel we show an example of a diagram where a gluon emitted in one dipole in the amplitude connects to another dipole in the complex conjugate amplitude. As can be seen from the upper panel of Fig. 4.16, such a diagram is indeed nonplanar; hence, it is $1/N_c^2$-suppressed (as can be checked explicitly) and can be neglected in the large-N_c limit. At the same time, the diagram in the lower panel of Fig. 4.16, while of the same order in $\alpha_s \ln 1/x$, is also planar: in it the gluon from one dipole does not interact with the other dipole, remaining instead in its own dipole. This second diagram in Fig. 4.16 is of leading order in N_c and has to be resummed by large-N_c dipole evolution. (Strictly speaking, the diagram in the lower left panel of Fig. 4.16, when written in double-line notation, also contains a nonplanar subleading-N_c correction, in which the quark line in the longer gluon interacts with the quark of the original dipole: this correction is not shown in Fig. 4.16.)

Note that, in order to obtain the leading-$\ln 1/x$ contribution to the wave function, the softer gluons (those with smaller z) have to be emitted later (to the right in our LCPT diagrams) than the harder gluons, with larger values of z. For instance, let us consider an onium wave function with two gluon emissions, as shown in Fig. 4.17. Assume further that the gluon emitted earlier is softer than the gluon emitted later, i.e., that $z_3 \ll z_2$,

https://doi.org/10.1017/9781009291446.005 Published online by Cambridge University Press

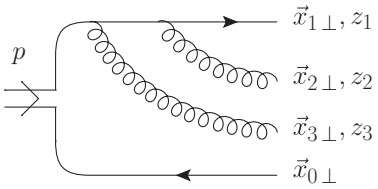

Fig. 4.17. Two gluons emitted in the onium wave function: if one assumes that the gluon emitted earlier is softer, $z_3 \ll z_2$, then the square of this diagram will not give a leading-$\ln 1/x$ contribution.

where, as usual,

$$z_i = \frac{k_i^+}{p^+}. \tag{4.65}$$

A simple calculation of the wave function in Fig. 4.17, in the $z_3 \ll z_2$ approximation, carried out along the steps outlined above for a single emission would yield a wave function proportional to z_3/z_2 as far as the longitudinal momentum dependence is concerned. Squaring this wave function and integrating the result over z_2 and z_3 with $z_1 \gg z_2 \gg z_3 \gg z_0$ yields an answer proportional to

$$\alpha_s^2 \int_{z_0}^{z_1} \frac{dz_2}{z_2} \int_{z_0}^{z_2} \frac{dz_3}{z_3} \frac{z_3^2}{z_2^2} \approx \frac{1}{2}\alpha_s^2 \ln \frac{z_1}{z_0}. \tag{4.66}$$

We see that we have only one longitudinal logarithm per two powers of the coupling α_s: this is not a leading logarithmic contribution. Hence the square of the diagram in Fig. 4.17 is subleading in $\ln 1/x$ and does not contribute to the leading-$\ln 1/x$ evolution we are considering here. It does contribute when one attempts to calculate the NLO corrections to the evolution we are about to construct (see Chapter 6). Using similar arguments, one can show that the diagram in Fig. 4.17 does not contribute to the LLA, even when we take its overlap with the wave function resulting when gluon 3 is emitted after gluon 2. In fact one can also show that no diagram with inverse time-ordering like that in Fig. 4.17 contributes in the LLA approximation. We thus come to another important conclusion: to obtain LLA evolution in the wave function, the gluon emissions with

$$z_2 \gg z_3 \gg \cdots \gg z_n \tag{4.67}$$

must be ordered in time, with the harder (larger-z) gluons emitted *before* the softer (small-z) gluons.

Now the structure of the small-x light cone wave function becomes manifest: in one step of evolution a gluon is emitted. It can be a real gluon, like those in the top and bottom panels of Fig. 4.15, which would split the initial (parent) dipole 10 ("one-zero") into two new (daughter) dipoles 12 and 20. The subsequent $\alpha_s \ln 1/x$ evolution is driven by further gluon emission: this would happen independently (and in parallel) in both daughter dipoles. An example of two-gluon emission is shown in the second panel of Fig. 4.16. Alternatively, the emission in the initial dipole can be virtual, as shown in the middle panel of Fig. 4.15;

https://doi.org/10.1017/9781009291446.005 Published online by Cambridge University Press

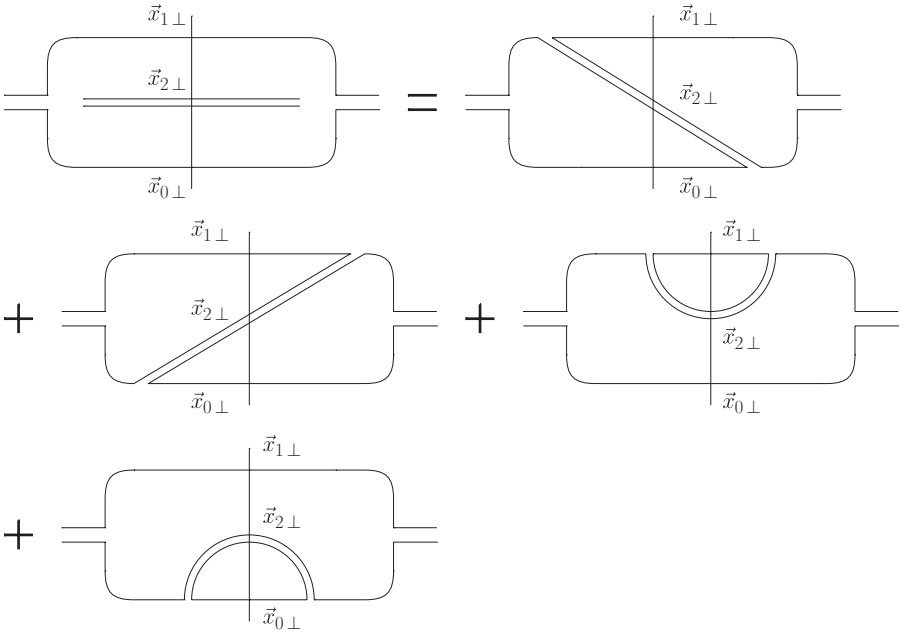

Fig. 4.18. Definition of an abbreviated notation for the sum of all large-N_c diagrams contributing to the real-gluon emission in the square of an onium wave function.

then the initial dipole remains intact, any subsequent evolution occurring within the initial dipole at later times.

As we can see from Eqs. (4.63) and (4.64), in the mixed representation in which we are working, each step of the evolution factorizes from the previous one, simplifying the construction of the gluon wave function. To illustrate this, let us consider two steps of small-x evolution due to two consecutive real-gluon emissions, including all possible LLA diagrams. It is convenient to introduce the shorthand diagram notation presented in Fig. 4.18, where the sum of all four (large-N_c) diagrams corresponding to real-gluon emission in the onium wave function comprises one diagram, that in the upper left of the figure. The diagrams in Fig. 4.18 give us the correction to the dipole wave function in Eq. (4.63). The kernel of this correction can be decomposed as follows:

$$\frac{\alpha_s C_F}{\pi^2}\frac{x_{10}^2}{x_{20}^2 x_{21}^2} = \frac{\alpha_s C_F}{\pi^2}\left(\frac{1}{x_{21}^2} - 2\frac{\vec{x}_{21}\cdot\vec{x}_{20}}{x_{21}^2 x_{20}^2} + \frac{1}{x_{20}^2}\right), \tag{4.68}$$

where the first and the last terms on the right-hand side of Eq. (4.68) correspond to the last two graphs in Fig. 4.18, while the first two (interference) diagrams on the right of Fig. 4.18 give the second term on the right of Eq. (4.68). The very first diagram in Fig. 4.18 corresponds to the full emission kernel on the left of Eq. (4.68).

Using the notation of Fig. 4.18, the square of the large-N_c onium wave function with two real gluons in it in the LLA approximation can be represented simply by the two diagrams depicted in Fig. 4.19, with the gluons ordered in longitudinal momenta such that $z_2 \gg z_3$.

https://doi.org/10.1017/9781009291446.005 Published online by Cambridge University Press

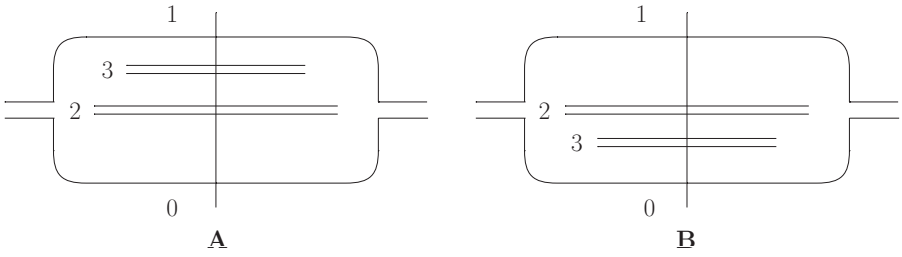

Fig. 4.19. Two real gluons in the LLA approximation and in the large-N_c limit contributing to the square of an onium wave function. The length of the lines is driven by light cone time-ordering.

According to the rules outlined above, the gluon carrying momentum fraction z_2 has to be emitted before the gluon carrying z_3, as shown in Fig. 4.19. The emission of gluon 2 splits the original dipole 10 into two dipoles. The subsequent emission of gluon 3 can occur either in dipole 12 (Fig. 4.19A) or in dipole 20 (Fig. 4.19B). (Note that gluon 3 is emitted from gluon 2 via a three-gluon vertex.) Iterating Eq. (4.63) twice, we see that the sum of the graphs A and B in Fig. 4.19 brings into the onium wave function squared the following factor:

$$\int_{z_0}^{z_1} \frac{dz_2}{z_2} \int_{z_0}^{z_2} \frac{dz_3}{z_3} \int d^2x_2\, d^2x_3 \left(\frac{\alpha_s C_F}{\pi^2}\right)^2 \frac{x_{10}^2}{x_{20}^2 x_{21}^2} \left(\frac{x_{12}^2}{x_{31}^2 x_{32}^2} + \frac{x_{20}^2}{x_{32}^2 x_{30}^2}\right). \tag{4.69}$$

(For simplicity of notation we have put z_1 as the upper cutoff of the z_2-integration, since at LLA accuracy one cannot see any significant difference between z_1 and $1 - z_1$.) Equation (4.69) demonstrates that the small-x evolution in the onium wave function consists of consecutive emissions ordered in rapidity and light cone time, with the transverse dynamics included in a factorized way.

To describe the onium wave function formally including $\alpha_s \ln 1/x$ corrections to all orders it is convenient to define the *dipole generating functional* $Z(\vec{x}_{10}, \vec{b}_{0\perp}, Y; u)$ by

$$\begin{aligned} Z(\vec{x}_{10}, \vec{b}_{0\perp}, Y; u) &\sum_{\sigma\sigma'} |\Psi^{(0)}_{\sigma\sigma'}(\vec{x}_{10}, z_1)|^2 \Big|_{O(\alpha_s^0)} \\ &= \int d^2r_1 d^2b_1 |\Psi^{[1]}(\vec{r}_{1\perp}, \vec{b}_{1\perp}, Y)|^2 u(\vec{r}_{1\perp}, \vec{b}_{1\perp}) \\ &\quad + \frac{1}{2!} \int d^2r_1 d^2b_1 d^2r_2 d^2b_2 |\Psi^{[2]}(\vec{r}_{1\perp}, \vec{b}_{1\perp}, \vec{r}_{2\perp}, \vec{b}_{2\perp}, Y)|^2 \\ &\qquad \times u(\vec{r}_{1\perp}, \vec{b}_{1\perp}) u(\vec{r}_{2\perp}, \vec{b}_{2\perp}) + \cdots \\ &= \sum_{n=1}^{\infty} \frac{1}{n!} \int d^2r_1 d^2b_1 \cdots d^2r_n d^2b_n |\Psi^{[n]}(\vec{r}_{1\perp}, \vec{b}_{1\perp}, \ldots, \vec{r}_{n\perp}, \vec{b}_{n\perp}, Y)|^2 \\ &\qquad \times u(\vec{r}_{1\perp}, \vec{b}_{1\perp}) \cdots u(\vec{r}_{n\perp}, \vec{b}_{n\perp}). \end{aligned} \tag{4.70}$$

https://doi.org/10.1017/9781009291446.005 Published online by Cambridge University Press

We have defined the rapidity variable $Y = \ln(z_1/z_0)$, where now z_0 is the smallest momentum fraction carried by a gluon in the wave function. In Eq. (4.70) the light cone wave functions $\Psi^{[n]}(\vec{r}_{1\perp}, \vec{b}_{1\perp}, \ldots, \vec{r}_{n\perp}, \vec{b}_{n\perp}, Y)$ correspond to the onium state consisting of n dipoles with sizes $\vec{r}_{1\perp}, \ldots, \vec{r}_{n\perp}$ whose centers (in the transverse plane) are located at impact parameters $\vec{b}_{1\perp}, \ldots, \vec{b}_{n\perp}$ (e.g. $\vec{b}_{0\perp} = (1/2)(\vec{x}_{1\perp} + \vec{x}_{0\perp})$). The rapidity interval between these daughter dipoles and the original parent dipole 1 0 is less than or equal to Y, i.e., the wave functions squared $|\Psi^{[n]}|^2$ are implicitly integrated over dipole rapidities from 0 to Y. Summation over all appropriate quantum numbers is implied in the square of the wave function $\Psi^{[n]}$. Note that $\Psi^{(0)}_{\sigma\sigma'}(\vec{x}_{10}, z_1)$ taken at order α_s^0 is the bare wave function of the onium before any emissions have taken place. In going from gluons to color dipoles we have changed the notation for the wave functions: while $\Psi^{(n)}$ denotes a wave function with n real gluons in it, $\Psi^{[n]}$ is a wave function with n dipoles (note the use of square brackets rather than parentheses). Since we always have at least one dipole (the original onium), the sum over n in Eq. (4.70) starts at $n = 1$.

The dummy functions $u(\vec{r}_{n\perp}, \vec{b}_{n\perp})$ are introduced so that one can extract the squares of different multi-dipole onium wave functions from the generating functional Z, using

$$|\Psi^{[n]}(\vec{r}_{1\perp}, \vec{b}_{1\perp}, \ldots, \vec{r}_{n\perp}, \vec{b}_{n\perp}, Y)|^2 = \sum_{\sigma\sigma'} |\Psi^{(0)}_{\sigma\sigma'}(\vec{x}_{10}, z_1)|^2 \Big|_{O(\alpha_s^0)} \times \frac{\delta^n}{\delta u(\vec{r}_{1\perp}, \vec{b}_{1\perp}) \cdots \delta u(\vec{r}_{n\perp}, \vec{b}_{n\perp})} Z(\vec{x}_{10}, \vec{b}_{0\perp}, Y; u)\Big|_{u=0}, \tag{4.71}$$

where $\delta/\delta u(\vec{r}_\perp, \vec{b}_\perp)$ is a functional derivative. As usual this derivative is defined such that (see e.g. Peskin and Schroeder (1995) for details)

$$\frac{\delta}{\delta u(\vec{r}_\perp, \vec{b}_\perp)} u(\vec{r}'_\perp, \vec{b}'_\perp) = \delta^{(2)}\left(\vec{r}_\perp - \vec{r}'_\perp\right) \delta^{(2)}\left(\vec{b}_\perp - \vec{b}'_\perp\right), \tag{4.72}$$

which leads to

$$\frac{\delta}{\delta u(\vec{r}_\perp, \vec{b}_\perp)} \int d^2r' d^2b' \, f(\vec{r}'_\perp, \vec{b}'_\perp) \, u(\vec{r}'_\perp, \vec{b}'_\perp) = f(\vec{r}_\perp, \vec{b}_\perp) \tag{4.73}$$

for an arbitrary function $f(\vec{r}_\perp, \vec{b}_\perp)$.

Since $|\Psi^{[n]}|^2$ gives the probability of having n dipoles in the onium wave function in a given transverse space configuration, and since the sum over probabilities of having any number of dipoles in all transverse configurations is 1, we conclude that (see Eq. (1.70))

$$Z(\vec{x}_{10}, \vec{b}_{0\perp}, Y; u = 1) = 1. \tag{4.74}$$

We want to write down an evolution equation for the generating functional Z summing all powers of $\alpha_s Y$. Before we do so, let us set up the initial condition for such an evolution. When $Y = 0$ we have no evolution and no gluon emissions (neither real nor virtual). Hence

https://doi.org/10.1017/9781009291446.005 Published online by Cambridge University Press

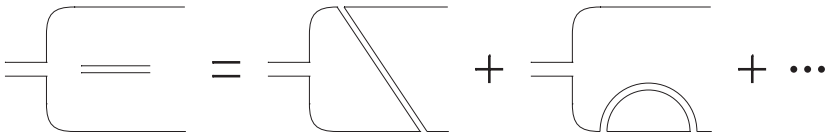

Fig. 4.20. An abbreviated notation for the sum of all large-N_c diagrams contributing to the virtual gluon correction to the onium wave function.

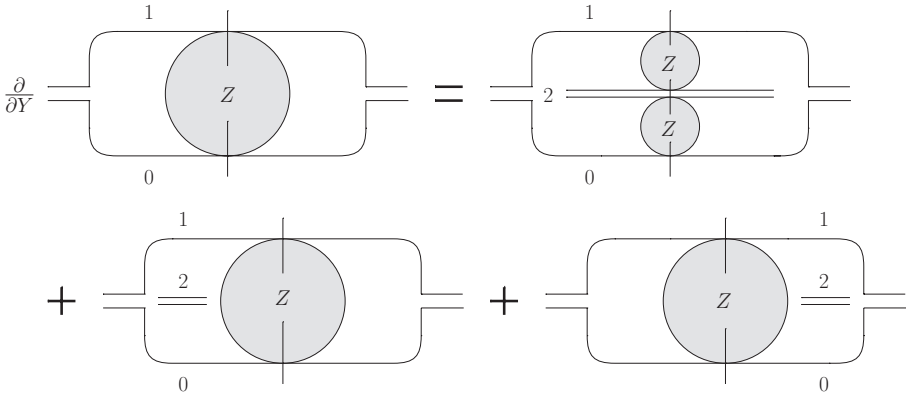

Fig. 4.21. Diagrammatic representation for the evolution equation of the generating functional Z (denoted by a shaded circle).

$|\Psi^{[n>1]}(Y=0)|^2 = 0$ and

$$|\Psi^{[1]}(\vec{r}_{1\perp}, \vec{b}_{1\perp}, Y=0)|^2 = \delta^2\left(\vec{b}_{1\perp} + \frac{\vec{r}_{1\perp}}{2} - \vec{x}_{1\perp}\right)\delta^2\left(\vec{b}_{1\perp} - \frac{\vec{r}_{1\perp}}{2} - \vec{x}_{0\perp}\right), \qquad (4.75)$$

such that

$$Z(\vec{x}_{10}, \vec{b}_{0\perp}, Y=0; u) = u(\vec{x}_{10}, \vec{b}_{0\perp}). \qquad (4.76)$$

Now that we have the initial conditions for Z-evolution, it is straightforward to write down an evolution equation for Z. The main principle was stated several pages ago: in one step of evolution a gluon is emitted in the dipole wave function: the gluon may be real, splitting the parent dipole into two daughter dipoles, or it may be virtual, leaving the parent dipole intact. In the former case the subsequent evolution continues independently in the two daughter dipoles, while in the latter case evolution continues in the parent dipole. This statement is illustrated diagrammatically in Fig. 4.21, where the generating functional Z is represented by a shaded circle. The first graph on the right of Fig. 4.21 corresponds to real-gluon emission, while the remaining two graphs represent the sum of all virtual corrections, as shown in Fig. 4.20.

Guided by Fig. 4.21, and employing Eqs. (4.63) and (4.64) while replacing C_F by $N_c/2$ in the large-N_c limit, we can write down the following evolution equation for the generating

https://doi.org/10.1017/9781009291446.005 Published online by Cambridge University Press

functional Z (Mueller 1994, 1995):

$$\frac{\partial}{\partial Y} Z(\vec{x}_{10}, \vec{b}_{0\perp}, Y; u) = \frac{\alpha_s N_c}{2\pi^2} \int d^2x_2 \frac{x_{10}^2}{x_{20}^2 x_{21}^2} \times \left[Z\left(\vec{x}_{12}, \vec{b}_{0\perp} + \frac{\vec{x}_{20}}{2}, Y; u\right) Z\left(\vec{x}_{20}, \vec{b}_{0\perp} + \frac{\vec{x}_{21}}{2}, Y; u\right) - Z(\vec{x}_{10}, \vec{b}_{0\perp}, Y; u) \right]. \tag{4.77}$$

The first term on the right-hand side of Eq. (4.77) corresponds to the first term on the right of Fig. 4.21, while the last two terms in Fig. 4.21 give rise to the second term on the right of Eq. (4.77). The minus sign in this second term is due to the minus sign in the virtual correction in Eq. (4.64).

Equation (4.77) is a nonlinear evolution equation whose initial condition is given in Eq. (4.76). Solving this evolution equation would allow one to construct the squares of the multi-dipole onium wave functions using Eq. (4.71). Unfortunately the exact analytical solution of Eq. (4.77) is not known. So, let us first connect Eq. (4.77) with results that are already familiar to the reader, such as the BFKL equation.

4.3.2 The BFKL equation in transverse coordinate space

Consider the following functional derivative taken at $u = 1$:

$$\left.\frac{\delta Z(\vec{x}_{10}, \vec{b}_{0\perp}, Y; u)}{\delta u(\vec{r}_\perp, \vec{b}_\perp)}\right|_{u=1} = \sum_{n=1}^{\infty} \frac{n}{n!} \int d^2r_2 d^2b_2 \cdot\cdots\cdot d^2r_n d^2b_n \times \frac{|\Psi^{[n]}(\vec{r}_\perp, \vec{b}_\perp, \vec{r}_{2\perp}, \vec{b}_{2\perp}, \ldots, \vec{r}_{n\perp}, \vec{b}_{n\perp}, Y)|^2}{\sum_{\sigma\sigma'} |\Psi^{(0)}_{\sigma\sigma'}(\vec{x}_{10}, z_1)|^2 \Big|_{O(\alpha_s^0)}}. \tag{4.78}$$

If instead the value of the derivative had been taken at $u = 0$, the physical meaning of the above object would have been clear from Eq. (4.71): it would have been the single-dipole wave function squared, divided by the original onium's wave function. To understand the physical meaning of the actual object in Eq. (4.78) we note that the probability of having n dipoles in the onium wave function (for an onium of given size $\vec{x}_{10}$ and quark momentum fraction z_1) is given by

$$P_n(Y) = \frac{1}{n!} \int d^2r_1 d^2b_1 \cdots d^2r_n d^2b_n \frac{|\Psi^{[n]}(\vec{r}_{1\perp}, \vec{b}_{1\perp}, \ldots, \vec{r}_{n\perp}, \vec{b}_{n\perp}, Y)|^2}{\sum_{\sigma\sigma'} |\Psi^{(0)}_{\sigma\sigma'}(\vec{x}_{10}, z_1)|^2 \Big|_{O(\alpha_s^0)}}, \tag{4.79}$$

where the factorial is a symmetry factor removing the multiple counting of identical dipole configurations, and where $n > 0$. The condition (4.74) translates into $\sum_{n=1}^{\infty} P_n(Y) = 1$.

https://doi.org/10.1017/9781009291446.005 Published online by Cambridge University Press

The average number of dipoles (at rapidities up to Y) in the onium wave function is

$$\langle n(Y)\rangle = \sum_{n=1}^{\infty} n P_n(Y). \tag{4.80}$$

The series (4.80) is very similar to that in Eq. (4.78), except that in Eq. (4.78) we are keeping the transverse size and impact parameter of one dipole fixed. We have thus arrived at the physical meaning of the object in Eq. (4.78): it is the number of dipoles of size $\vec{r}_\perp$ at impact parameter $\vec{b}_\perp$ and with rapidities between 0 and Y located in the onium wave function. We denote this object by $n_1(\vec{x}_{10}, \vec{r}_\perp, \vec{b}_\perp - \vec{b}_{0\perp}, Y)$, so that

$$n_1(\vec{x}_{10}, \vec{r}_\perp, \vec{b}_\perp - \vec{b}_{0\perp}, Y) = \left.\frac{\delta Z(\vec{x}_{10}, \vec{b}_{0\perp}, Y; u)}{\delta u(\vec{r}_\perp, \vec{b}_\perp)}\right|_{u=1}. \tag{4.81}$$

To construct an equation for $n_1(\vec{x}_{10}, \vec{r}_\perp, \vec{b}_\perp - \vec{b}_{0\perp}, Y)$ we simply have to differentiate Eq. (4.77) with respect to u, putting $u = 1$ at the end using Eq. (4.74). This yields an equation that we will shortly show to be equivalent to the BFKL equation (Mueller 1994, Mueller and Patel 1994, Mueller 1995, Nikolaev, Zakharov, and Zoller (1994))[5]

$$\frac{\partial}{\partial Y} n_1(\vec{x}_{10}, \vec{r}_\perp, \vec{b}_\perp, Y) = \frac{\alpha_s N_c}{2\pi^2} \int d^2x_2 \frac{x_{10}^2}{x_{20}^2 x_{21}^2} \left[n_1\left(\vec{x}_{12}, \vec{r}_\perp, \vec{b}_\perp - \frac{\vec{x}_{20}}{2}, Y\right) + n_1\left(\vec{x}_{20}, \vec{r}_\perp, \vec{b}_\perp - \frac{\vec{x}_{21}}{2}, Y\right) - n_1(\vec{x}_{10}, \vec{r}_\perp, \vec{b}_\perp, Y)\right]. \tag{4.82}$$

We have relabeled $\vec{b}_\perp - \vec{b}_{0\perp}$ simply as $\vec{b}_\perp$, which therefore now has the meaning of the transverse space distance between the centers of the original dipole 10 and the dipole of interest, of size $\vec{r}_\perp$. The initial condition for Eq. (4.82) is obtained by differentiating Eq. (4.76) with respect to $u(\vec{r}_\perp, \vec{b}_\perp)$ and afterwards putting $u = 1$:

$$n_1(\vec{x}_{10}, \vec{r}_\perp, \vec{b}_\perp, Y = 0) = \delta^2(\vec{x}_{10} - \vec{r}_\perp)\, \delta^2\left(\vec{b}_\perp\right). \tag{4.83}$$

The distribution of pairs of dipoles in the onium wave function can be defined as a second derivative of the generating functional:

$$n_2(\vec{x}_{10}, \vec{r}_{1\perp}, \vec{b}_{1\perp} - \vec{b}_{0\perp}, \vec{r}_{2\perp}, \vec{b}_{2\perp} - \vec{b}_{0\perp}, Y) = \left.\frac{\delta^2 Z(\vec{x}_{10}, \vec{b}_{0\perp}, Y; u)}{\delta u(\vec{r}_{1\perp}, \vec{b}_{1\perp}) \delta u(\vec{r}_{2\perp}, \vec{b}_{2\perp})}\right|_{u=1}. \tag{4.84}$$

Equation (4.84) gives the number of pairs of dipoles with sizes $\vec{r}_{1\perp}$ and $\vec{r}_{2\perp}$ located at impact parameters $\vec{b}_{1\perp}$ and $\vec{b}_{2\perp}$ and in the rapidity interval $[0, Y]$. The equation for n_2 is constructed in analogy to that for n_1 by the double differentiation of Eq. (4.77) with respect to $u(\vec{r}_{1\perp}, \vec{b}_{1\perp})$ and $u(\vec{r}_{2\perp}, \vec{b}_{2\perp})$, putting $u = 1$ at the end. The main difference

[5] Nikolaev and Zakharov (1994) and Nikolaev, Zakharov, and Zoller (1994) were very close to solving these problems. Nikolaev and Zakharov (1994) rewrote the DLA DGLAP evolution in terms of color dipoles. Nikolaev, Zakharov, and Zoller (1994) obtained the BFKL equation in the dipole formulation, though several months later than Mueller (1994). Lipatov (1986) was the first to notice that the BFKL equation has a particularly elegant form in the transverse coordinate representation but his approach lacked the idea of using color dipoles instead of the transverse coordinates of the gluons.

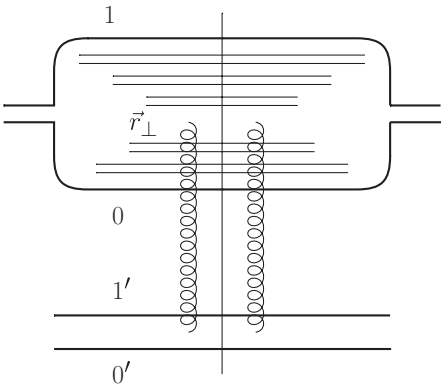

Fig. 4.22. Onium–onium scattering in the BFKL approximation in the dipole model, with the lower onium $1'0'$ at rest.

comes in the initial conditions: the second derivative of Eq. (4.76) with respect to u gives $n_2(\vec{x}_{10}, \vec{r}_{1\perp}, \vec{b}_{1\perp}, \vec{r}_{2\perp}, \vec{b}_{2\perp}, Y = 0) = 0$. The equation for n_2 is also a linear differential equation, though it also contains powers of n_1. We will not write down this equation explicitly and instead refer the reader to the papers by Mueller (1995) and Mueller and Patel (1994). Higher derivatives of the generating functional Z give the number distributions of dipole triplets, quadruplets, etc. The nth-order derivative of Z with respect to u gives the distribution of n dipoles in the onium wave function.

While dipole number distributions are interesting quantities in themselves, they also allow one to calculate scattering cross sections in a physically intuitive way. Consider onium–onium scattering at high energies, where the small-x evolution is important. This is the kinematics in which we studied the BFKL evolution in Sec. 3.3. Let us now try to reproduce the BFKL result in the dipole language. Consider a frame in which one onium is at rest while the other is incident on it at high energy. The total onium–onium scattering cross section per unit impact parameter can then be written as a convolution of the number of dipoles in the incident onium wave function and the scattering cross section of each dipole on the onium when at rest:

$$n(\vec{x}_{10}, \vec{x}_{1'0'}, \vec{b}, Y) = \int d^2r d^2b' n_1(\vec{x}_{10}, \vec{r}_\perp, \vec{b}'_\perp - \vec{b}_\perp, Y) \frac{d\hat{\sigma}_{tot}^{onium-onium}(\vec{r}_\perp, \vec{x}_{1'0'})}{d^2b'}. \quad (4.85)$$

Here the two colliding onia have transverse sizes $\vec{x}_{10}$ and $\vec{x}_{1'0'}$ (the latter is at rest), $\vec{b}$ is the impact parameter, Y is the net rapidity interval for the onium–onium scattering, and $d\hat{\sigma}_{tot}^{onium-onium}(\vec{r}_\perp, \vec{r}'_\perp)/d^2b$ is the cross section for the scattering of two onia with sizes $\vec{r}_\perp$ and $\vec{r}'_\perp$ mediated by a two-gluon exchange, as calculated in Exercise 3.3 (see Eq. (3.139)). Equation (4.85) is illustrated in Fig. 4.22, where dipole evolution in the onium 10 creates a dipole of size $\vec{r}_\perp$, which then interacts with the onium $1'0'$ via a two-gluon exchange.

Note that the dipole number density n_1 counts all dipoles with rapidities between 0 and Y (with respect to the dipole 10): any of these dipoles (if it has size $\vec{r}_\perp$, over which we will

https://doi.org/10.1017/9781009291446.005 Published online by Cambridge University Press

integrate) can interact with the dipole $1'0'$. The quantity n_1 is, therefore, integrated over the dipole rapidities. Such an integration is justified at the wave function level because the Born-level cross section $\hat{\sigma}_{tot}^{onium-onium}$ is energy independent and cannot affect the result of the integration.

It is important to stress that, while the dipole number distribution n_1 in Eq. (4.85) is a function of $\alpha_s N_c$ (see Eq. (4.82)) and is thus of order N_c^0 in the 't Hooft large-N_c limit, the two-gluon exchange cross section $\hat{\sigma}_{tot}^{onium-onium}$ is of order $\alpha_s^2 \sim (\alpha_s N_c)^2/N_c^2 \sim 1/N_c^2$, so that the whole onium–onium scattering cross section is N_c-suppressed. This is indeed in agreement with the well-known result that any interaction cross section is N_c-suppressed at large N_c (see e.g. Witten (1979)). The essential feature of the interactions in the dipole model is the factorization into light cone wave function(s) and elementary scattering cross sections. As the scattering cross sections are always N_c-suppressed, to capture the dominant contribution to the scattering one has to use the leading-N_c wave functions constructed above. The factorization presented in Fig. 4.22 is not unique: in a different reference frame, say the center-of-mass frame, the dipole wave functions of both onia contain small-x evolution; a dipole from one wave function exchanges two gluons with a dipole in another wave function (Mueller and Patel 1994). Such a factorization gives the same answer as the one we will obtain below for Fig. 4.22.

To find the scattering cross section per unit impact parameter,

$$n(\vec{x}_{10}, \vec{x}_{1'0'}, \vec{b}_\perp, Y) = \frac{d\hat{\sigma}_{tot}^{onium-onium}(\vec{x}_{10}, \vec{x}_{1'0'}, Y)}{d^2b}, \tag{4.86}$$

one can first solve Eq. (4.82) and then use the solution in Eq. (4.85) along with the cross section from Eq. (3.139). Alternatively, one may note that the cross section $n(\vec{x}_{10}, \vec{x}_{1'0'}, \vec{b}, Y)$ itself satisfies Eq. (4.82):

$$\begin{aligned}
&\frac{\partial}{\partial Y} n(\vec{x}_{10}, \vec{x}_{1'0'}, \vec{b}_\perp, Y) \\
&\quad = \frac{\alpha_s N_c}{2\pi^2} \int d^2x_2 \frac{x_{10}^2}{x_{20}^2 x_{21}^2} \\
&\qquad \times \left[n\left(\vec{x}_{12}, \vec{x}_{1'0'}, \vec{b}_\perp - \frac{\vec{x}_{20}}{2}, Y\right) + n\left(\vec{x}_{20}, \vec{x}_{1'0'}, \vec{b}_\perp - \frac{\vec{x}_{21}}{2}, Y\right) - n(\vec{x}_{10}, \vec{x}_{1'0'}, \vec{b}_\perp, Y) \right]
\end{aligned} \tag{4.87}$$

with initial condition (cf. Eq. (3.139))

$$\begin{aligned}
n(\vec{x}_{10}, \vec{x}_{1'0'}, \vec{b}_\perp, Y = 0) &= \frac{d\hat{\sigma}_{tot}^{onium-onium}(\vec{x}_{10}, \vec{x}_{1'0'})}{d^2b} \\
&= \frac{2\alpha_s^2 C_F}{N_c} \ln^2 \frac{x_{11'} x_{00'}}{x_{10'} x_{01'}}.
\end{aligned} \tag{4.88}$$

Equation (4.87) can be solved exactly: the solution is somewhat involved and will be left for the next section. Instead, we will consider here the simplified case where a cross section is integrated over all impact parameters $\vec{b}_\perp$. In momentum space this corresponds to the $t = 0$ case, of zero momentum transfer. On top of that we will average over the directions

https://doi.org/10.1017/9781009291446.005 Published online by Cambridge University Press

of $\vec{x}_{1'0'}$: the resulting cross section does not depend on the directions of $\vec{x}_{10}$ either, since there is no preferred direction left in the transverse space. Defining

$$n(x_{10}, x_{1'0'}, Y) = \int d^2b \int_0^{2\pi} \frac{d\phi_{1'0'}}{2\pi} n(\vec{x}_{10}, \vec{x}_{1'0'}, \vec{b}_\perp, Y), \tag{4.89}$$

we see that this new quantity satisfies

$$\frac{\partial}{\partial Y} n(x_{10}, x_{1'0'}, Y) = \frac{\alpha_s N_c}{2\pi^2} \int d^2x_2 \frac{x_{10}^2}{x_{20}^2 x_{21}^2} \times \left[n\left(x_{12}, x_{1'0'}, Y\right) + n\left(x_{20}, x_{1'0'}, Y\right) - n(x_{10}, x_{1'0'}, Y) \right] \tag{4.90}$$

with initial condition (cf. Eq. (3.25))

$$n(x_{10}, x_{1'0'}, Y = 0) = \frac{4\pi\alpha_s^2 C_F}{N_c} x_<^2 \left(\ln \frac{x_>}{x_<} + 1 \right), \tag{4.91}$$

where $x_{>(<)} = \max\,(\min)\{|\vec{x}_{10}|, |\vec{x}_{1'0'}|\}$.

The solution of Eq. (4.90) can be found by noticing that in the angular-averaged case the eigenfunctions of the integral kernel are simple powers of the dipole size,

$$\left(x_{01}^2\right)^{1/2+i\nu} \tag{4.92}$$

with eigenvalues

$$\frac{\alpha_s N_c}{\pi} \chi(0, \nu), \tag{4.93}$$

where (cf. Eqs. (3.81), (3.74))

$$\chi(0, \nu) = 2\psi(1) - \psi\left(\frac{1}{2} + i\nu\right) - \psi\left(\frac{1}{2} - i\nu\right). \tag{4.94}$$

To prove this we need to evaluate the following integral:

$$\int d^2x_2 \frac{x_{10}^2}{x_{20}^2 x_{21}^2} \left[\left(x_{12}^2\right)^{1/2+i\nu} + \left(x_{20}^2\right)^{1/2+i\nu} - \left(x_{10}^2\right)^{1/2+i\nu} \right]. \tag{4.95}$$

This can be done by noticing that the integral (4.95) is equivalent to that in Eq. (3.64) with $n = 0$. Alternatively, one can use the trick presented in appendix section A.3; in order to make each term in Eq. (4.95) finite we insert a UV regulator ρ. After that, with the help of Eqs. (A.18), (A.21), (A.24), and (A.29) one can rewrite Eq. (4.95) as

$$2\pi \left[2^{1+2i\nu} \frac{\Gamma\left(\frac{1}{2} + i\nu\right)}{\Gamma\left(\frac{1}{2} - i\nu\right)} x_{10}^2 \int_0^\infty dk k^{-2i\nu} \left(\ln \frac{2}{k\rho} + \psi(1) \right) J_0(kx_{10}) - x_{10}^{1+2i\nu} \ln \frac{x_{10}^2}{\rho^2} \right]. \tag{4.96}$$

Integrating over k in Eq. (4.96) using Eq. (A.18) yields

$$2\pi x_{10}^{1+2i\nu} \chi(0, \nu), \tag{4.97}$$

as desired.

https://doi.org/10.1017/9781009291446.005 Published online by Cambridge University Press

We see that, as for to the BFKL equation (3.58), the eigenfunctions of Eq. (4.90) are powers (though of the transverse dipole size instead of the transverse momentum), with exactly the same eigenvalues, (4.93) as in that case.[6] We conclude that Eq. (4.90) is equivalent to the BFKL equation!

In fact, the substitution (Levin and Ryskin 1987)

$$n(x_{10}, x_{1'0'}, Y) = \int d^2k \left(1 - e^{i\vec{k}_\perp \cdot \vec{x}_{10}}\right) \frac{1}{k_\perp^2} f(\vec{k}_\perp, x_{1'0'}, Y) \tag{4.98}$$

turns Eq. (4.90) into the BFKL equation (3.58) for the function f (Kovchegov and Weigert 2007b). Verification of this statement is left as an exercise for the reader.

Using the eigenfunctions and the eigenvalues of the integral kernel in Eq. (4.90), we can write down the solution of Eq. (4.90) as

$$n(x_{10}, x_{1'0'}, Y) = \int\limits_{-\infty}^{\infty} d\nu \, C_\nu(x_{1'0'}) x_{10}^{1+2i\nu} e^{\bar{\alpha}_s \chi(0,\nu) Y}, \tag{4.99}$$

where the coefficient $C_\nu(x_{1'0'})$ is fixed by the initial conditions (4.91) as follows:

$$C_\nu(x_{1'0'}) = \frac{16\,\alpha_s^2 C_F}{N_c} \frac{1}{(1+4\nu^2)^2} x_{1'0'}^{1-2i\nu}. \tag{4.100}$$

The general solution of Eq. (4.90) is then

$$n(x_{10}, x_{1'0'}, Y) = \frac{16\alpha_s^2 C_F}{N_c} x_{10}\, x_{1'0'} \int\limits_{-\infty}^{\infty} d\nu \left(\frac{x_{10}}{x_{1'0'}}\right)^{2i\nu} \frac{e^{\bar{\alpha}_s \chi(0,\nu) Y}}{(1+4\nu^2)^2}. \tag{4.101}$$

For $x_{10} \approx x_{1'0'}$ we can use the diffusion approximation from Sec. 3.3.4: expanding $\chi(0, \nu)$ around $\nu = 0$ using Eq. (3.84) and integrating over ν we obtain

$$n(x_{10}, x_{1'0'}, Y) = \frac{16\alpha_s^2 C_F}{N_c} x_{10} x_{1'0'} \sqrt{\frac{\pi}{14\zeta(3)\bar{\alpha}_s Y}} \times \exp\left[(\alpha_P - 1)Y - \frac{\ln^2(x_{10}/x_{1'0'})}{14\zeta(3)\,\bar{\alpha}_s Y}\right]. \tag{4.102}$$

Readers who performed Exercise 3.5 will recognize Eq. (4.102) as the answer for the onium–onium scattering cross section obtained there using the standard Feynman diagram approach. Now we see that a calculation based on LCPT wave functions gives the same result. Note that the single-dipole distribution n_1 is only one component of the onium wave function. This wave function also contains multi-dipole distributions n_2, n_3, etc. Hence, as we will shortly see, the dipole approach, while in a certain limit equivalent to BFKL, in fact contains more information.

[6] We have verified this statement so far only in the case where the angular dependence has been integrated out: we will consider the general angular-dependent case in the next section.

https://doi.org/10.1017/9781009291446.005 Published online by Cambridge University Press

4.3.3 The general solution of the coordinate-space BFKL equation*

Let us now construct the solution of the BFKL equation (4.87) without making any simplifying assumptions. The goal now is to construct the most general eigenfunctions of the kernel of Eq. (4.87). This kernel operates in the transverse plane: it is convenient to think of this plane as a complex plane, replacing the two-component vectors $\vec{x}_{i\perp}$ by complex numbers ρ_i, namely

$$\rho_i = x_{i,1} + i x_{i,2}; \quad \rho_i^* = x_{i,1} - i x_{i,2}, \tag{4.103}$$

where the indices 1, 2 denote two transverse axes. In the same way as in the vector notation we define $\rho_{ij} = \rho_i - \rho_j$ and $\rho_{ij}^* = \rho_i^* - \rho_j^*$, along with the absolute value squared $|\rho_{ij}|^2 = \rho_{ij}\rho_{ij}^*$ and the integration measure $d^2\rho = d\rho d\rho^*$. Using the above complex notation it is straightforward to check that the kernel of Eq. (4.87), written as

$$\int d^2\rho_2 \frac{|\rho_{10}^2|}{|\rho_{20}^2||\rho_{21}^2|} \tag{4.104}$$

is conformally invariant: it is clearly invariant under rotations, translations, scale transformations, and reflections in the complex plane. It is also invariant under the inversion

$$\rho_i \to \frac{1}{\rho_i^*}, \quad \rho_i^* \to \frac{1}{\rho_i}. \tag{4.105}$$

Thus the kernel is invariant under all Möbius transformations

$$z \to \frac{az+b}{cz+d} \tag{4.106}$$

for arbitrary complex a, b, c, and d with $ad - bc \neq 0$. When $ad - bc = 1$ the group reduces to SL(2, C).

Consider the functions (Lipatov 1986)

$$E^{n,\nu}(\rho_{1a}, \rho_{2a}) = \left(\frac{\rho_{12}}{\rho_{1a}\rho_{2a}}\right)^{(1+n)/2+i\nu} \left(\frac{\rho_{12}^*}{\rho_{1a}^*\rho_{2a}^*}\right)^{(1-n)/2+i\nu}, \tag{4.107}$$

where ρ_a is an arbitrary point in the complex (transverse) plane, with $\rho_{ia} = \rho_i - \rho_a$ as before; n is integer and ν is real. It is easy to check by direct differentiation that the functions $E^{n,\nu}$ are the eigenfunctions of the Casimir operators M^2 and M^{*2} of the conformal Möbius group (Lipatov 1986, Lipatov 1989, Bartels, Lipatov, and Vacca 2005):

$$M^2 E^{n,\nu}(\rho_{1a}, \rho_{2a}) \equiv \rho_{12}^2 \partial_1 \partial_2 E^{n,\nu}(\rho_{1a}, \rho_{2a}) = -h(h-1)E^{n,\nu}(\rho_{1a}, \rho_{2a}), \tag{4.108a}$$

$$M^{*2} E^{n,\nu}(\rho_{1a}, \rho_{2a}) \equiv \rho_{12}^{*2} \partial_1^* \partial_2^* E^{n,\nu}(\rho_{1a}, \rho_{2a}) = -\bar{h}(\bar{h}-1)E^{n,\nu}(\rho_{1a}, \rho_{2a}), \tag{4.108b}$$

where $\partial_i = \partial/\partial\rho_i$, $\partial_i^* = \partial/\partial\rho_i^*$, and

$$h = \frac{1+n}{2} + i\nu, \quad \bar{h} = \frac{1-n}{2} + i\nu. \tag{4.109}$$

https://doi.org/10.1017/9781009291446.005 Published online by Cambridge University Press

The functions $E^{n,\nu}$ are orthonormal (Lipatov 1986)

$$\int \frac{d^2\rho_1 d^2\rho_2}{|\rho_{12}|^4} E^{n,\nu}(\rho_{1a},\rho_{2a}) E^{m,\mu}(\rho_{1b},\rho_{2b}) = a_{n,\nu}\delta_{nm}\delta(\nu-\mu)\delta^2(\rho_{ab}) + b_{n,\nu}|\rho_{ab}|^{-2-4i\nu}\left(\frac{\rho_{ab}}{\rho^*_{ab}}\right)^n \delta_{n,-m}\delta(\nu+\mu), \tag{4.110}$$

where

$$a_{n,\nu} = \frac{\pi^4/2}{\nu^2+n^2/4} = \frac{|b_{n,\nu}|^2}{2\pi^2}, \tag{4.111a}$$

$$b_{n,\nu} = \pi^3 2^{4i\nu}\frac{\Gamma\left(-i\nu+\frac{1}{2}(1+|n|)\right)}{\Gamma\left(i\nu+\frac{1}{2}(1+|n|)\right)}\frac{\Gamma\left(i\nu+\frac{1}{2}|n|\right)}{\Gamma\left(1-i\nu+\frac{1}{2}|n|\right)}. \tag{4.111b}$$

(Note that $E^{n,\nu}$ and $E^{-n,-\nu}$ are not orthogonal.) The functions $E^{n,\nu}$ also form a complete basis (Lipatov 1986), so that

$$(2\pi)^4\delta^2(\rho_{11'})\delta^2(\rho_{22'}) = \sum_{n=-\infty}^{\infty}\int_{-\infty}^{\infty} d\nu \int d^2\rho_a \frac{16(\nu^2+\frac{1}{4}n^2)}{|\rho_{12}|^2|\rho_{1'2'}|^2} \times E^{n,\nu}(\rho_{1a},\rho_{2a})E^{n,\nu*}(\rho_{1'a},\rho_{2'a}). \tag{4.112}$$

The delta functions on the left of Eq. (4.112) should be understood as acting on the space of well-behaved functions of ρ_1, ρ_2, $\rho_{1'}$, and $\rho_{2'}$ that go to zero in the limits $\rho_1=\rho_2$ and $\rho_{1'}=\rho_{2'}$.

Since the kernel of Eq. (4.87) is invariant under Möbius transformations, the functions $E^{n,\nu}$ are its eigenfunctions. To see this explicitly we need to find

$$I(\rho_0,\rho_1,\rho_a) \equiv \int d^2\rho_2 \frac{|\rho_{10}^2|}{|\rho_{20}^2||\rho_{21}^2|}[E^{n,\nu}(\rho_{1a},\rho_{2a}) + E^{n,\nu}(\rho_{2a},\rho_{0a}) - E^{n,\nu}(\rho_{1a},\rho_{0a})]. \tag{4.113}$$

Performing the inversion transformation and also reflection with respect to ρ_a, i.e., $\rho_i \to 1/\rho_{ia}$, yields

$$I(1/\rho_0,1/\rho_1,\infty) = \int d^2\rho_2 \frac{|\rho_{01}|^2}{|\rho_{02}|^2|\rho_{12}|^2}\left(\rho^h_{20}\rho^{*\bar{h}}_{20} + \rho^h_{12}\rho^{*\bar{h}}_{12} - \rho^h_{10}\rho^{*\bar{h}}_{10}\right). \tag{4.114}$$

The integral now becomes equivalent to that in Eq. (3.64), the answer to which is given by Eqs. (3.68) and (3.74). Using those results and reversing the $\rho_i \to 1/\rho_{ia}$ transformation, we write

$$I(\rho_0,\rho_1,\rho_a) = 2\pi\chi(n,\nu)E^{n,\nu}(\rho_{1a},\rho_{0a}), \tag{4.115}$$

with $\chi(n,\nu)$ given by Eq. (3.81).

https://doi.org/10.1017/9781009291446.005 Published online by Cambridge University Press

Since the $E^{n,\nu}$ are the eigenfunctions of the dipole kernel and form a complete orthonormal basis, we can write the general solution of Eq. (4.87) as

$$n(\vec{x}_{10}, \vec{x}_{1'0'}, \vec{b}_\perp, Y) = n(\rho_1, \rho_0; \rho_{1'}, \rho_{0'}; Y) = \sum_{n=-\infty}^{\infty} \int_{-\infty}^{\infty} d\nu \int d^2\rho_a e^{\bar{\alpha}_s \chi(n,\nu) Y} C_{n,\nu} E^{n,\nu}(\rho_{1a}, \rho_{0a}) E^{n,\nu *}(\rho_{1'a}, \rho_{0'a}), \tag{4.116}$$

with the coefficients $C_{n,\nu}$ fixed by the initial condition (4.88), which in the complex plane can be written as

$$n(\rho_1, \rho_0; \rho_{1'}, \rho_{0'}; Y = 0) = \frac{2\alpha_s^2 C_F}{N_c} \ln^2 \left| \frac{\rho_{11'}\rho_{00'}}{\rho_{10'}\rho_{01'}} \right|. \tag{4.117}$$

To find the $C_{n,\nu}$ we need to decompose the (Möbius-invariant) logarithm squared into a series over the $E^{n,\nu}$:

$$\ln^2 \left| \frac{\rho_{11'}\rho_{00'}}{\rho_{10'}\rho_{01'}} \right| = \sum_{n=-\infty}^{\infty} \int_{-\infty}^{\infty} d\nu \int d^2\rho_a D_{n,\nu} E^{n,\nu}(\rho_{1a}, \rho_{0a}) E^{n,\nu *}(\rho_{1'a}, \rho_{0'a}). \tag{4.118}$$

The coefficients $D_{n,\nu}$ can be found if we first note that

$$|\rho_{10}|^4 \partial_1 \partial_1^* \partial_0 \partial_0^* \ln^2 \left| \frac{\rho_{11'}\rho_{00'}}{\rho_{10'}\rho_{01'}} \right| = \frac{\pi^2}{2} |\rho_{10}|^2 |\rho_{1'0'}|^2 \left[\delta^2(\rho_{11'}) \delta^2(\rho_{00'}) + \delta^2(\rho_{10'}) \delta^2(\rho_{01'}) \right]. \tag{4.119}$$

Using Eq. (4.112) along with the following property of the $E^{n,\nu}$ functions,

$$E^{n,\nu}(\rho_{1a}, \rho_{2a}) = (-1)^n E^{n,\nu}(\rho_{2a}, \rho_{1a}), \tag{4.120}$$

yields

$$|\rho_{10}|^4 \partial_1 \partial_1^* \partial_0 \partial_0^* \ln^2 \left| \frac{\rho_{11'}\rho_{00'}}{\rho_{10'}\rho_{01'}} \right| = \frac{1}{\pi^2} \sum_{\text{even } n} \int_{-\infty}^{\infty} d\nu \int d^2\rho_a \left(\nu^2 + \tfrac{1}{4} n^2 \right) \times E^{n,\nu}(\rho_{0a}, \rho_{1a}) E^{n,\nu *}(\rho_{0'a}, \rho_{1'a}), \tag{4.121}$$

where the sum runs over all integer even n. However, using Eqs. (4.108) and (4.118) we get

$$|\rho_{10}|^4 \partial_1 \partial_1^* \partial_0 \partial_0^* \ln^2 \left| \frac{\rho_{11'}\rho_{00'}}{\rho_{10'}\rho_{01'}} \right| = \sum_{n=-\infty}^{\infty} \int_{-\infty}^{\infty} d\nu \int d^2\rho_a D_{n,\nu} h(h-1) \bar{h}(\bar{h}-1) \times E^{n,\nu}(\rho_{1a}, \rho_{0a}) E^{n,\nu *}(\rho_{1'a}, \rho_{0'a}). \tag{4.122}$$

https://doi.org/10.1017/9781009291446.005 Published online by Cambridge University Press

Comparing Eqs. (4.122) and (4.121) we can read off $D_{n,\nu}$, and substituting it back into Eq. (4.118) we obtain

$$\ln^2\left|\frac{\rho_{11'}\rho_{00'}}{\rho_{10'}\rho_{01'}}\right| = \frac{1}{\pi^2}\sum_{\text{even } n}\int_{-\infty}^{\infty} d\nu \int d^2\rho_a \frac{\nu^2+\frac{1}{4}n^2}{\left[\nu^2+\frac{1}{4}(n+1)^2\right]\left[\nu^2+\frac{1}{4}(n-1)^2\right]} \times E^{n,\nu}(\rho_{0a},\rho_{1a})E^{n,\nu*}(\rho_{0'a},\rho_{1'a}). \tag{4.123}$$

Equations (4.123) and (4.117), when compared with Eq. (4.116), allow us to write for even n

$$C_{n,\nu} = \frac{2\alpha_s^2 C_F}{\pi^2 N_c}\frac{\nu^2+\frac{1}{4}n^2}{\left[\nu^2+\frac{1}{4}(n+1)^2\right]\left[\nu^2+\frac{1}{4}(n-1)^2\right]} \tag{4.124}$$

with $C_{n,\nu}=0$ for odd n.

Equations (4.116) and (4.124) give us the most general solution of Eq. (4.87) with initial condition (4.88) (cf. Lipatov 1986):

$$\begin{aligned} &n(\rho_1,\rho_0;\rho_{1'},\rho_{0'};Y) \\ &\quad= \frac{2\alpha_s^2 C_F}{\pi^2 N_c}\sum_{\text{even } n}\int_{-\infty}^{\infty} d\nu\, e^{\bar{\alpha}_s\chi(n,\nu)Y} \\ &\qquad\times \frac{\nu^2+\frac{1}{4}n^2}{\left[\nu^2+\frac{1}{4}(n+1)^2\right]\left[\nu^2+\frac{1}{4}(n-1)^2\right]}\int d^2\rho_a E^{n,\nu}(\rho_{0a},\rho_{1a})E^{n,\nu*}(\rho_{0'a},\rho_{1'a}). \end{aligned} \tag{4.125}$$

The integral over ρ_a in Eq. (4.125) can be carried out analytically (Lipatov 1997, Navelet and Peschanski 1997), yielding a somewhat simplified expression in terms of hypergeometric functions:

$$\begin{aligned} &n(\rho_1,\rho_0;\rho_{1'},\rho_{0'};Y) \\ &\quad= \frac{\alpha_s^2 C_F}{\pi^4 N_c}\sum_{\text{even } n}\int_{-\infty}^{\infty} d\nu\, e^{\bar{\alpha}_s\chi(n,\nu)Y}\frac{\nu^2+\frac{1}{4}n^2}{\left[\nu^2+\frac{1}{4}(n+1)^2\right]\left[\nu^2+\frac{1}{4}(n-1)^2\right]} \\ &\qquad\times\Big[b_{n,-\nu}w^h w^{*\bar{h}}F(h,h;2h;w)F(\bar{h},\bar{h};2\bar{h};w^*) \\ &\qquad+ b_{n,\nu}w^{1-h}w^{*1-\bar{h}}F(1-h,1-h;2(1-h);w)F(1-\bar{h},1-\bar{h};2(1-\bar{h});w^*)\Big], \end{aligned} \tag{4.126}$$

where

$$w = \frac{\rho_{01}\rho_{0'1'}}{\rho_{00'}\rho_{11'}}, \tag{4.127}$$

https://doi.org/10.1017/9781009291446.005 Published online by Cambridge University Press

so that

$$\ln^2 \left| \frac{\rho_{11'}\rho_{00'}}{\rho_{10'}\rho_{01'}} \right| = \ln^2 |1 - w|. \tag{4.128}$$

4.4 The Balitsky–Kovchegov equation

We now return to the DIS process in the dipole picture of Sec. 4.1. As follows from Eqs. (4.12) and (4.24), in order to find the DIS structure function all one needs is to find the imaginary part of the dipole–nucleus forward scattering amplitude $N(\vec{x}_\perp, \vec{b}_\perp, Y)$. In Sec. 4.2 we constructed such an amplitude in the Glauber–Gribov–Mueller multiple rescattering approximation. The resulting forward amplitude has no energy dependence, as one can see from Eq. (4.49), and therefore cannot be a realistic description of the high energy asymptotics of dipole–nucleus scattering. At the same time, the approach of Sec. 4.2 is valid only when the small-x evolution emissions are not important, that is, only for $\alpha_s Y \ll 1$. At higher energies, corresponding to rapidities Y satisfying $\alpha_s Y \gtrsim 1$, small-x evolution becomes important and can no longer be neglected.

We see that we need to resum the LLA corrections to the dipole–nucleus scattering amplitude (4.49). As usual we are interested in quantum evolution corrections that resum the powers of $\alpha_s \ln 1/x \sim \alpha_s Y$.[7] Just as in Sec. 4.2 we will be working in the rest frame of the nucleus, but this time we choose to work in the light cone gauge of the projectile dipole, $A^+ = 0$, if it is moving in the light cone plus direction. One can show by explicit calculation that for the multiple rescatterings in Fig. 4.5 this gauge is equivalent to the covariant gauge ($\partial_\mu A^\mu = 0$, see Sec. 3.3.1); therefore, our discussion in Sec. 4.2 remains valid in this new gauge. As in Sec. 4.2 we will be working either in the nucleus rest frame or in the frame in which the dipole is moving in the light cone plus direction while the target nucleus is moving in the minus direction.

We need to identify radiative corrections that bring in powers of $\alpha_s Y$. As we saw in Sec. 4.2, multiple rescatterings bring in only powers of α_s not enhanced by factors of Y (but enhanced by powers of A; the resummation parameter was $\alpha_s^2 A^{1/3}$). Therefore, additional t-channel gluon exchanges with new nucleons would not generate any powers of Y but would bring in only extra factors of α_s. These are not the corrections we are trying to resum now. Other possible corrections in the light cone gauge of the projectile dipole are modifications of the dipole wave function. The incoming dipole may have some gluons (and "sea" quarks) present in its wave function. For instance, the dipole may emit a gluon before interacting with the target; then the whole system of quark, antiquark, and gluon would rescatter in the nucleus, as shown in the upper panel of Fig. 4.23. The dipole may emit two gluons, which would then interact with the nucleus, along with the original $q\bar{q}$ pair, as shown in the lower panel of Fig. 4.23. In principle there could be many extra gluon emissions, as well as the generation of extra $q\bar{q}$ pairs in the incoming dipole's wave function. As we will shortly see, these gluonic fluctuations from Fig. 4.23 actually do bring

[7] Quantum evolution is defined as the variation of a physical quantity, with Q^2 and/or x, resulting from quantum emissions and absorptions.

https://doi.org/10.1017/9781009291446.005 Published online by Cambridge University Press

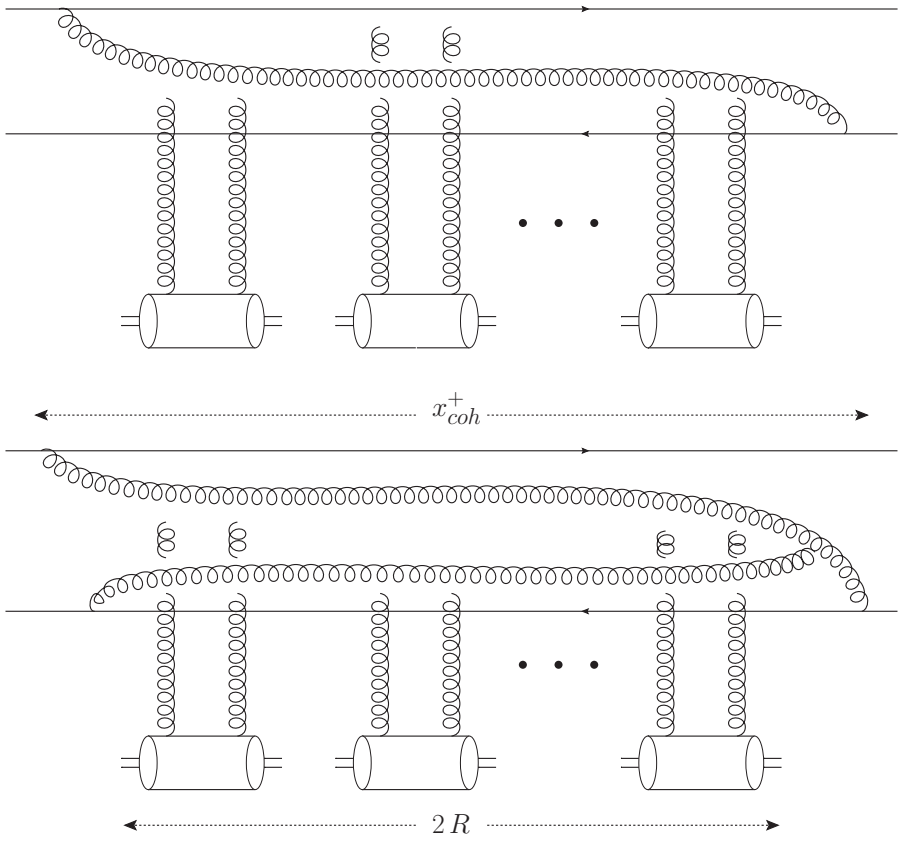

Fig. 4.23. Quantum evolution corrections to dipole–nucleus scattering due to one-gluon (upper panel) and two-gluon (lower panel) emissions. The lower panel also shows the coherence time scale for gluon emission x^+_{coh} and the nuclear size $2R$. At high energy $x^+_{coh} \gg 2R$: the figure does not fully reflect this scale difference.

the factors of α_s enhanced by powers of rapidity Y, i.e., they do generate leading logarithmic corrections. Just as with the BFKL evolution, fluctuations leading to the formation of $q\bar{q}$ pairs actually enter at the subleading logarithmic level, bringing in powers of $\alpha_s^2 Y$, and are not important for the leading logarithmic approximation used in this chapter.

Several times above (see the discussion around Eqs. (2.156), (3.126), and (4.2)), we have used the fact that owing to the uncertainty principle, for an incoming dipole moving in the light cone plus direction a gluon with momentum k^μ in its wave function would have coherence length

$$x^+_{coh} \approx \frac{k^+}{k_\perp^2} \tag{4.129}$$

along the x^+-axis. Note straight away that t-channel gluon exchanges between the dipole and the nucleons in the nucleus, in the Glauber–Gribov–Mueller approximation of Sec. 4.2, have $k^+ = 0$ with eikonal accuracy (i.e., up to corrections suppressed by powers of the

https://doi.org/10.1017/9781009291446.005 Published online by Cambridge University Press

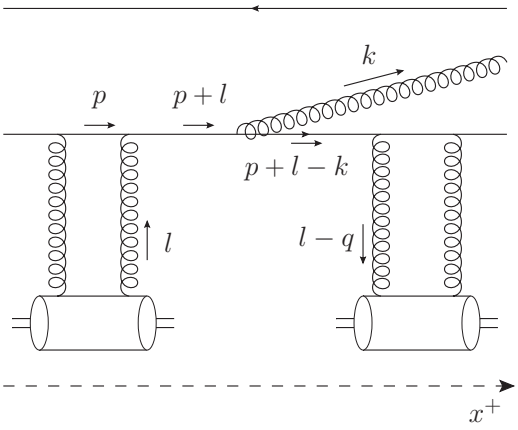

Fig. 4.24. A diagram with a gluon emission between the dipole interactions with two nucleons.

energy). Thus these t-channel gluons have $x^+_{coh} = 0$ and are instantaneous in the x^+ "time" direction in our eikonal picture. These are the instantaneous or Coulomb gluons. The instantaneous nature of these gluons explains why the dipole rescatters on the nucleons sequentially: as the nucleons are assumed to be separated in x^+, the dipole interacts with a nucleon as it crosses the latter's x^+-range, with interactions that are out of order, like that in Fig. 4.6B, not allowed by causality. The nucleons span the whole nucleus; thus the x^+-time interval filled with the instantaneous interactions of Fig. 4.5 is of the order of the nuclear radius R in the nuclear rest frame.

Consider now the gluon modifications to the incoming dipole's wave function shown in Fig. 4.23. If a gluon's k^+ is large enough, as is the case at high energy, the coherence lengths of these gluons would be much larger than the nuclear radius, $x^+_{coh} \gg R$, so that each gluon would coherently rescatter on the nucleons in the nucleus, just like the original dipole in Fig. 4.5. This is indeed what is shown in Fig. 4.23.

Note that gluons are emitted by the incoming dipole only before the multiple rescattering interaction (and absorbed back, after the interaction, into the forward amplitude). Emissions during the interaction are suppressed by the inverse powers of the center-of-mass energy of the scattering system. This can be checked via an explicit calculation in the covariant Feynman perturbation theory. Imagine a diagram with the gluon emitted or absorbed between the rescatterings, as shown in Fig. 4.24. As in our analysis of the graph in Fig. 4.9 above, we concentrate on the contribution of quark propagators to the l^--integral. We see that the diagram is proportional to

$$\int\limits_{-\infty}^{\infty} \frac{dl^-}{2\pi} \frac{e^{-il^-\Delta x^+}}{[(p+l)^2+i\epsilon][(p+l-k)^2+i\epsilon]}$$

$$\approx \int\limits_{-\infty}^{\infty} \frac{dl^-}{2\pi} \frac{e^{-il^-\Delta x^+}}{[p^+l^- - \perp^2 + i\epsilon][(p^+ - k^+)(k^- + l^-) - \perp'^2 + i\epsilon]} \tag{4.130}$$

https://doi.org/10.1017/9781009291446.005 Published online by Cambridge University Press

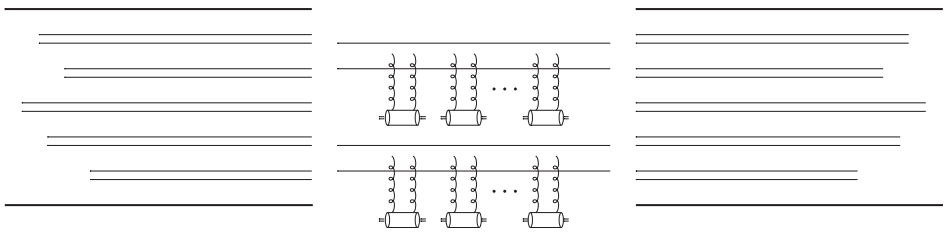

Fig. 4.25. Forward amplitude for dipole–nucleus scattering including small-x evolution: the incoming dipole develops a cascade of daughter dipoles, each of which interacts with the nucleus independently.

where $\perp$ and $\perp'$ denote the appropriate transverse momenta, whose exact values are not important to us here. We have used the fact that $l^+ = 0$ and assumed for simplicity that $p^- = 0$. We also changed the frame to that where the nucleus is moving along the negative light cone. Closing the integration contour in the lower half-plane we obtain

$$\frac{-i}{p^+(p^+-k^+)}\frac{1}{k^- + \perp^2/p^+ - \perp'^2/(p^+-k^+)}\left[e^{-i\frac{\perp^2}{p^+}\Delta x^+} - e^{-i\left(-k^- + \frac{\perp'^2}{p^+-k^+}\right)\Delta x^+}\right]$$
$$\approx \frac{-i}{p^{+2}k^-}\left(1 - e^{ik^-\Delta x^+}\right) \sim \frac{-1}{p^{+2}p'^-} = \frac{-1}{p^+ s}, \tag{4.131}$$

where we have used the fact that $p^+ \gg k^+$ and, more importantly, $\Delta x^+ \sim 1/p'^-$ with p'^- the large light cone momentum of a nucleon in the nucleus (such that $s = p^+ p'^-$ is the dipole–nucleon center-of-mass energy squared). This allowed us to expand the exponential in the second line of Eq. (4.131). Comparing with the rescatterings without gluon emission given in Eq. (4.37) (identifying k^+ in (4.37) with p^+ here), we see that gluon emission between rescatterings brings in suppression by a power of the energy squared s and can thus be neglected.

Alternatively we can consider this calculation in light cone perturbation theory. In this case, the emission of a gluon is allowed and is equally probable at any point throughout the coherence length of the parent dipole $x_{coh}^{q\bar{q}+} = p^+/p_\perp^2$, with p the momentum of the dipole and p^+ very large. The probability of emission of a gluon inside the nucleus (in the nuclear rest frame) is then proportional to $R/x_{coh}^{q\bar{q}+} \sim 1/p^+ \sim 1/s$; i.e., again, just as in Eq. (4.131) it is suppressed by a power of the center-of-mass energy squared s compared with emission outside the nucleus and can be neglected in the eikonal approximation considered here.

Our goal, therefore, is to resum the cascade of long-lived gluons that the dipole in Fig. 4.23 develops before interacting with the nucleus and then to convolute this cascade with the interaction amplitudes of the gluons with the nucleus. To resum the cascade we will assume the large-N_c limit and use Mueller's dipole model, presented in Sec. 4.3. In the large-N_c limit the gluon cascade translates into a dipole cascade, examples of which are shown in Figs. 4.19 and 4.22. As we have seen above, in the LLA gluon emissions do not change the transverse coordinates of the quark and antiquark lines in the parent dipole. Therefore, the color dipoles have the same transverse coordinates throughout the whole process: once they are created their transverse coordinates do not change. Resummation of the dipole cascade reduces to the set of diagrams represented in Fig. 4.25, which is

https://doi.org/10.1017/9781009291446.005 Published online by Cambridge University Press

a generalization of Fig. 4.5 to the case of quantum evolution corrections. The incoming dipole develops a cascade of daughter dipoles through evolution according to Mueller dipole model.

The evolved system of dipoles interacts with the nucleus. The interaction is brief and does not change the transverse coordinates of the dipoles. In the large-N_c limit no dipole interacts with any other dipole during the evolution that generates all the dipoles. For a large nucleus the daughter dipole–nucleus interaction was calculated above in the GGM approximation and is given by Eq. (4.51). That result resums powers of $\alpha_s^2 A^{1/3}$. Analyzing the diagrams for the interaction of several dipoles with the nucleus we see that the GGM interaction of, say, two dipoles with a single nucleon is suppressed by extra powers of α_s not enhanced by $A^{1/3}$ and is therefore subleading and can be neglected. The interaction of two dipoles with two nucleons in the large-N_c limit is dominated by diagrams where each dipole interacts with only one nucleon (assuming both dipoles interact). In general one can argue that, in the large-N_c limit and at the leading order in A (or, equivalently, resumming powers of $\alpha_s^2 A^{1/3}$), the interaction of any number of dipoles with the nucleus is dominated by the *independent* interactions of each dipole with a different set of nucleons in the nucleus through multiple rescatterings of the type in Fig. 4.5. This is depicted in Fig. 4.25: when the dipole wave function hits the nucleus, each dipole present in the wave function may interact with different nucleons in the nucleus by the exchange of pairs of gluons. (It can be shown that only some dipoles thus interact.) Therefore, the dipoles are completely mutually noninteracting: they do not exchange gluons in the process of evolution, since those corrections would be suppressed by powers of N_c, and they interact with *different* nucleons in the nucleus; the last statement is correct at leading order in A (Kovchegov 1999).

Summation of the dipole cascade of Fig. 4.25 now becomes straightforward. Instead of calculating the forward dipole–nucleus scattering amplitude $N(\vec{x}_\perp, \vec{b}_\perp, Y)$ we start with the S-matrix $S(\vec{x}_\perp, \vec{b}_\perp, Y)$, which is related to N via Eq. (4.38). We write it here again for completeness:

$$S(\vec{x}_\perp, \vec{b}_\perp, Y) = 1 - N(\vec{x}_\perp, \vec{b}_\perp, Y). \tag{4.132}$$

As follows from the above discussion, $S(\vec{x}_{10}, \vec{b}_{0\perp}, Y)$ can be written as a convolution of the dipole cascade and the dipole interactions with the target, as shown in Fig. 4.25. Namely, it is a sum of the probability of finding one daughter dipole in the parent dipole, convoluted with the S-matrix for dipole–nucleus scattering in the GGM approximation, and the probability of finding two dipoles, convoluted with their multiple rescattering interactions with the nucleus, etc. We write (Kovchegov 1999)

$$S(\vec{x}_{10}, \vec{b}_\perp, Y) = \sum_{k=1}^{\infty} \frac{1}{k!} \int d^2 r_1 d^2 b_1 \cdots d^2 r_k d^2 b_k \times \frac{\delta^k Z(\vec{x}_{10}, \vec{b}_\perp, Y; u)}{\delta u(\vec{r}_{1\perp}, \vec{b}_{1\perp}) \cdots \delta u(\vec{r}_{k\perp}, \vec{b}_{k\perp})}\bigg|_{u=0} s_0(\vec{r}_{1\perp}, \vec{b}_{1\perp}) \cdots s_0(\vec{r}_{k\perp}, \vec{b}_{k\perp}). \tag{4.133}$$

https://doi.org/10.1017/9781009291446.005 Published online by Cambridge University Press

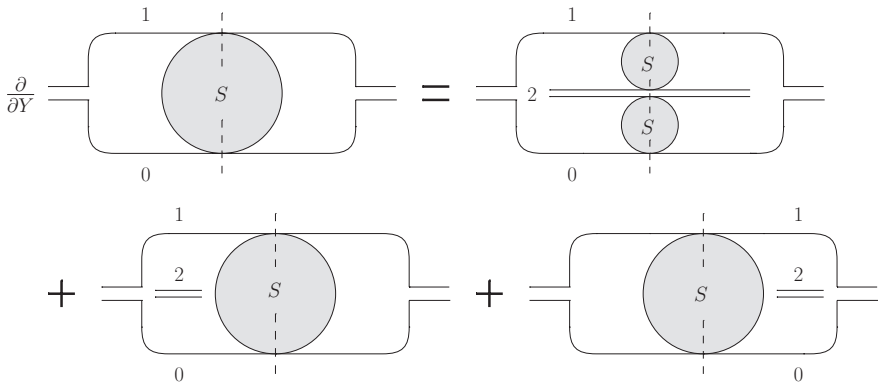

Fig. 4.26. Diagrammatic representation for the evolution equation of the S-matrix for dipole–nucleus scattering, denoted by a shaded circle. The vertical dashed lines denote the interaction with the target.

Here

$$\left.\frac{\delta^k Z(\vec{x}_{10}, \vec{b}_\perp, Y; u)}{\delta u(\vec{r}_{1\perp}, \vec{b}_{1\perp}) \cdots \delta u(\vec{r}_{k\perp}, \vec{b}_{k\perp})}\right|_{u=0} \tag{4.134}$$

gives the probability of finding *exactly* k daughter dipoles in the parent dipole wave function (cf. Eq. (4.71)), and

$$s_0(\vec{r}_\perp, \vec{b}_\perp) \equiv S(\vec{r}_\perp, \vec{b}_\perp, Y = 0) = \exp\left\{-\frac{x_\perp^2 Q_{s0}^2(\vec{b}_\perp)}{4} \ln \frac{1}{x_\perp \Lambda}\right\}, \tag{4.135}$$

as follows from Eqs. (4.51) and (4.132).

Summing the series in Eq. (4.133) yields (see Eq. (4.70))

$$S(\vec{x}_{10}, \vec{b}_\perp, Y) = Z\left(\vec{x}_{10}, \vec{b}_\perp, Y; u = s_0\right) \tag{4.136}$$

(Kovchegov 1999). This relation shows that both the dipole–nucleus S-matrix and the generating functional Z obey the same nonlinear evolution equation. The initial condition for Z in (4.76) is replaced by Eq. (4.135).

We see that the evolution of $S(\vec{x}_\perp, \vec{b}_\perp, Y)$ is the same as the evolution of the generation functional Z in Sec. 4.3: it is illustrated in Fig. 4.26 (cf. Fig. 4.21). The dipole cascade and its interaction with the target are denoted by a shaded circle. In one step of the evolution in energy (or rapidity) a soft gluon is emitted in the dipole. If the gluon is real then the original dipole is split into two dipoles, as shown at top right of Fig. 4.26; these dipoles proceed to evolve and interact (or not) independently with the target (the S-matrix includes the noninteraction term, the "1" in Eq. (4.132)). Virtual corrections, given by the two lower diagrams in Fig. 4.26, lead only to the parent dipole's subsequent evolution and interaction with the target. We obtain an evolution equation for the S-matrix (Balitsky 1996, Kovchegov

https://doi.org/10.1017/9781009291446.005 Published online by Cambridge University Press

1999):

$$\frac{\partial}{\partial Y}\, S(\vec{x}_{10}, \vec{b}_\perp, Y) = \frac{\alpha_s N_c}{2\pi^2} \int d^2x_2 \frac{x_{10}^2}{x_{20}^2 x_{21}^2} \times \left[S\left(\vec{x}_{12}, \vec{b}_\perp + \frac{\vec{x}_{20}}{2}, Y\right) S\left(\vec{x}_{20}, \vec{b}_\perp + \frac{\vec{x}_{21}}{2}, Y\right) - S(\vec{x}_{10}, \vec{b}_\perp, Y) \right]. \quad (4.137)$$

The initial condition for this evolution equation is given by $S(\vec{x}_{10}, \vec{b}_\perp, Y = 0)$ in Eq. (4.135). As usual $\vec{b}_\perp = (\vec{x}_{1\perp} + \vec{x}_{0\perp})/2$.

Using Eq. (4.132) in Eq. (4.137) we derive an evolution equation for the imaginary part of the forward dipole–nucleus scattering amplitude N (Balitsky 1996, Kovchegov 1999):

$$\frac{\partial}{\partial Y} N(\vec{x}_{10}, \vec{b}_\perp, Y) = \frac{\alpha_s N_c}{2\pi^2} \int d^2x_2 \frac{x_{10}^2}{x_{20}^2 x_{21}^2} \times \left[N\left(\vec{x}_{12}, \vec{b}_\perp + \frac{\vec{x}_{20}}{2}, Y\right) + N\left(\vec{x}_{20}, \vec{b}_\perp + \frac{\vec{x}_{21}}{2}, Y\right) - N(\vec{x}_{10}, \vec{b}_\perp, Y) - N\left(\vec{x}_{12}, \vec{b}_\perp + \frac{\vec{x}_{20}}{2}, Y\right) N\left(\vec{x}_{20}, \vec{b}_\perp + \frac{\vec{x}_{21}}{2}, Y\right) \right]. \quad (4.138)$$

This is the Balitsky–Kovchegov (BK) evolution equation. The initial condition for the BK evolution is given by Eq. (4.51):

$$N(\vec{x}_\perp, \vec{b}_\perp, Y = 0) = 1 - \exp\left\{ -\frac{x_\perp^2 Q_{s0}^2(\vec{b}_\perp)}{4} \ln \frac{1}{x_\perp \Lambda} \right\}, \quad (4.139)$$

where we have replaced $Q_s^2(\vec{b}_\perp)$ from Eq. (4.51) by $Q_{s0}^2(\vec{b}_\perp)$ to underscore that this is the saturation scale in the initial condition for the evolution. (As we will see shortly, the saturation scale is modified by the nonlinear BK evolution equation: in particular it becomes dependent on the rapidity Y.) Equation (4.138) resums all powers of the multiple rescattering parameter $\alpha_s^2 A^{1/3}$, along with the leading logarithms of energy in the large-N_c limit given by powers of $\alpha_s N_c Y$.

Below we will sometimes use a more compact notation for the dipole–nucleus amplitude,

$$N(\vec{x}_{1\perp}, \vec{x}_{0\perp}, Y) \equiv N(\vec{x}_{10}, \vec{b}_\perp, Y). \quad (4.140)$$

Using this notation, we can rewrite Eq. (4.138) as

$$\frac{\partial}{\partial Y} N(\vec{x}_{1\perp}, \vec{x}_{0\perp}, Y) = \frac{\alpha_s N_c}{2\pi^2} \int d^2x_2 \frac{x_{10}^2}{x_{20}^2 x_{21}^2} \times \left[N(\vec{x}_{1\perp}, \vec{x}_{2\perp}, Y) + N(\vec{x}_{2\perp}, \vec{x}_{0\perp}, Y) - N(\vec{x}_{1\perp}, \vec{x}_{0\perp}, Y) - N(\vec{x}_{1\perp}, \vec{x}_{2\perp}, Y)\, N(\vec{x}_{2\perp}, \vec{x}_{0\perp}, Y) \right]. \quad (4.141)$$

https://doi.org/10.1017/9781009291446.005 Published online by Cambridge University Press

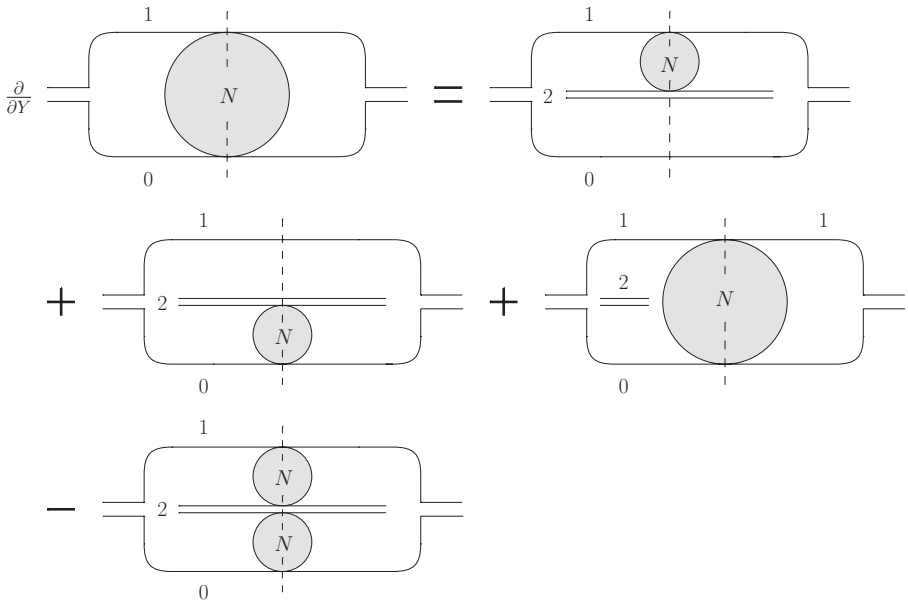

Fig. 4.27. Diagrammatic representation of the BK evolution equation for the forward dipole–nucleus scattering amplitude N, denoted by a shaded circle. Only one virtual term is shown, for brevity.

The BK equation is represented diagrammatically in Fig. 4.27. Balitsky–Kovchegov evolution has a simple physical meaning. At fixed rapidity a colorless dipole with size x_{10} decays into two dipoles with sizes x_{12} and x_{20}. Either one dipole proceeds to evolve and interact with the target while the other dipole remains a spectator (the first two, linear, terms after the equals sign in Fig. 4.27) or both dipoles evolve and interact with the target (the nonlinear term in Fig. 4.27). The minus sign in front of the nonlinear term reflects the fact that taking into account two independent interactions overestimates the result. The nonlinear term corresponds to the shadowing corrections in the GGM approach: for instance, expanding Eq. (4.45) in powers of interactions with the nucleons we see that the quadratic term enters with a minus sign. The reason for that minus sign is the same as the reason for the minus sign in the last term of Eq. (4.138).

Equation (4.138) was originally derived by Balitsky (1996) in the framework of the effective theory of high energy interactions and, independently, by one of the present authors (Kovchegov 1999) using the formalism of Mueller's dipole model (Mueller 1994, 1995). It was rederived by Braun (2000a) using the large-N_c limit of the expression for the triple pomeron vertex from Bartels and Wusthoff (1995) in a resummation of the fan diagrams in Fig. 3.23.

Comparing the linear part of the BK equation (the first three terms on the right of Eq. (4.138)) with Eq. (4.87), we see that the linear terms in the BK equation give the coordinate-space BFKL equation. As already mentioned, the nonlinear term can be obtained

https://doi.org/10.1017/9781009291446.005 Published online by Cambridge University Press

from the triple-pomeron vertex in the large-N_c limit (Braun 2000a). Hence Eq. (4.138) has the overall structure of the GLR equation and corresponds to fan diagram resummation in the conventional Feynman perturbation theory. It is natural to expect that the BK evolution leads to the same physical effects as the GLR equation: for a given fixed dipole size, the dipole amplitude N would start out growing with rapidity owing to BFKL evolution (see Eq. (4.102)); the nonlinear term would become important at higher rapidity and lead to saturation and slowdown of the energy growth. In the next section we will see that this is indeed the case.

In solving the BK equation (4.138) one often (but not always) assumes that the variation in the amplitude $N(\vec{x}_{10}, \vec{b}_\perp, Y)$ with the impact parameter $\vec{b}_\perp$ is small when $\vec{b}_\perp$ varies over distance scales comparable with the dipole size $|\vec{x}_{10}|$. This is indeed true for scattering on a very large nucleus far away from its edges. This assumption allows one to neglect the shifts in the impact parameter on the right-hand side of Eq. (4.138). Moreover, assuming that the nucleus is isotropic we may neglect the angular dependence of $\vec{x}_{10}$. We thus may replace $N(\vec{x}_{10}, \vec{b}_\perp, Y)$ approximately by $N(x_{10}, Y)$ in Eq. (4.138), obtaining

$$\frac{\partial}{\partial Y} N(x_{10}, Y) = \frac{\alpha_s N_c}{2\pi^2} \int d^2x_2 \frac{x_{10}^2}{x_{20}^2 x_{21}^2} \times \Big[N(x_{12}, Y) + N(x_{20}, Y) - N(x_{10}, Y) - N(x_{12}, Y)\, N(x_{20}, Y) \Big]. \tag{4.142}$$

Performing the Fourier transformation

$$N(x_\perp, Y) = x_\perp^2 \int \frac{d^2k}{2\pi} e^{i\vec{k}_\perp \cdot \vec{x}_\perp} \tilde{N}(k_\perp, Y), \tag{4.143}$$

we write (Kovchegov 2000)

$$\frac{\partial \tilde{N}(k_\perp, Y)}{\partial Y} = \bar{\alpha}_s \chi \left[0, \frac{i}{2} \left(1 + \frac{\partial}{\partial \ln k_\perp} \right) \right] \tilde{N}(k_\perp, Y) - \bar{\alpha}_s \tilde{N}^2(k_\perp, Y). \tag{4.144}$$

This equation is useful for obtaining approximate solutions for the BK evolution that we will present below. Also, note that making the identification

$$\phi(x, k_\perp^2) = \frac{N_c S_\perp}{\alpha_s \pi^2} \tilde{N}(k_\perp, Y = \ln 1/x) \tag{4.145}$$

in Eq. (4.144) reduces it to the GLR equation (3.128). This is indeed remarkable: however, there exists no physical justification for the Fourier transformation (4.143). At the lowest, two-gluon-exchange, order the relation between the dipole amplitude N and the unintegrated gluon distribution ϕ should be of the form of Eq. (4.98) (with f there proportional to ϕ). In the region where multiple rescatterings and quantum evolution are important, the exact relation between N and ϕ is not clear.

https://doi.org/10.1017/9781009291446.005 Published online by Cambridge University Press

4.5 Solution of the Balitsky–Kovchegov equation

To date there is no exact analytical solution of the BK equation. Below we will present several approximate analytical solutions, along with some numerical results. One of the main conclusions can be derived right away, without doing any work, if we notice that $N = 1$ is the fixed point of BK evolution: for $N = 1$, corresponding to the black-disk limit, the right-hand side of Eq. (4.138) vanishes and the growth of N with rapidity stops. Hence the BK equation does not violate the black-disk limit.

4.5.1 Solution outside the saturation region; extended geometric scaling

Let us begin analyzing BK evolution when the forward amplitude is small, $N \ll 1$. In the multiple rescatterings (GGM) approximation (see Eq. (4.139)) we know that for small dipoles with $x_\perp \ll 1/Q_{s0}$ the amplitude N is also small, and saturation and unitarization effects are not very important yet. The fact that the forward amplitude N goes to zero as $x_\perp \to 0$ is based on a fundamental physical principle of color transparency, which is valid beyond the multiple-rescattering approximation. This allows us to conclude that $N \ll 1$ for small dipole sizes $x_\perp$ even when small-x evolution is included. For $N \ll 1$ we can linearize the BK equation; as we observed earlier, this gives us the coordinate-space BFKL equation. With the approximation used in Eq. (4.142) we can write

$$\frac{\partial N(x_{10}, Y)}{\partial Y} = \frac{\bar{\alpha}_s}{2\pi} \int d^2x_2 \frac{x_{10}^2}{x_{20}^2 x_{21}^2} \Big[N(x_{12}, Y) + N(x_{20}, Y) - N(x_{10}, Y) \Big]. \tag{4.146}$$

This is exactly Eq. (4.90), whose solution we can write as (cf. Eq. (4.101))

$$N(x_\perp, Y) = \int_{-\infty}^{\infty} d\nu \, C_\nu \, \exp\{\bar{\alpha}_s \chi(0, \nu) Y + (1 + 2i\nu) \ln(x_\perp Q_{s0})\}, \tag{4.147}$$

where we use Q_{s0} as the typical transverse scale characterizing the target nucleus. In the $\vec{b}_\perp$-independent approximation that we are employing, Q_{s0} is not a function of $\vec{b}_\perp$. As usual, C_ν is a constant fixed by the initial conditions. Just as in the case of BFKL evolution, the integral (4.147) can be evaluated either in the DLA or in the diffusion approximation depending on the kinematics of the problem.

Double logarithmic approximation

Consider the case of very small dipole size, $x_\perp Q_{s0} \ll 1$, such that transverse logarithms like $\ln(x_\perp Q_{s0})$ become important, leading to a new resummation parameter $\alpha_s Y \ln(x_\perp Q_{s0})$. This is the DLA we considered before. Approximating $\chi(0, \nu)$ as follows,

$$\chi(0, \nu) \approx \frac{2}{1 - 2i\nu}, \tag{4.148}$$

https://doi.org/10.1017/9781009291446.005 Published online by Cambridge University Press

we find a saddle point at

$$\nu^*_{DLA} \approx -\frac{i}{2}\left(1-\sqrt{\frac{2\bar{\alpha}_s Y}{\ln 1/(x_\perp Q_{s0})}}\right). \tag{4.149}$$

Using Eq. (4.148) in Eq. (4.147) and performing the integration over ν in the saddle point approximation yields

$$N(x_\perp, Y)\Big|_{x_\perp Q_{s0}\ll 1} = (x_\perp Q_{s0})^2 C_{\nu^*_{DLA}} \frac{\sqrt{\pi}}{2} (2\bar{\alpha}_s Y)^{1/4} \ln^{-3/4} \frac{1}{x_\perp Q_{s0}} \times \exp\left\{2\sqrt{2\bar{\alpha}_s Y \ln 1/(x_\perp Q_{s0})}\right\}. \tag{4.150}$$

We see that, as for the GGM multiple-rescatterings case (see Eq. (4.139)), the amplitude $N(x_\perp, Y)$ in the DLA regime grows quadratically with the dipole size $x_\perp$, though this rise receives a correction owing to the exponential in Eq. (4.150). On top of that, as is typical for the DLA case, the amplitude also grows with rapidity Y.

Extended geometric scaling region

Now let us study the region where the dipole size is still small, but not much smaller than the inverse saturation scale: $x_\perp Q_{s0} \lesssim 1$. In this region, evolution is still linear and one would still expect Eq. (4.147) to give us the solution. We begin by evaluating the ν-integral in Eq. (4.147) in the saddle-point approximation. The location of the saddle point ν_{sp} is determined by the standard condition

$$\bar{\alpha}_s \chi'(0, \nu_{sp}) Y + 2i \ln x_\perp Q_{s0} = 0, \tag{4.151}$$

which gives the saddle point ν_{sp} as a function of $x_\perp$ and Y: $\nu_{sp} = \nu_{sp}(x_\perp, Y)$. (The prime in Eq. (4.151) indicates a derivative with respect to ν, $\chi'(0, \nu) = \partial\chi(0, \nu)/\partial\nu$.) Crudely approximating the ν-integral in Eq. (4.147) by the value of the integrand at $\nu = \nu_{sp}$, we obtain

$$N(x_\perp, Y) \propto (x_\perp Q_{s0})^{1+2i\nu_{sp}} e^{\bar{\alpha}_s \chi(0,\nu_{sp})Y}. \tag{4.152}$$

The amplitude given by Eq. (4.152) grows with energy and with the dipole size $x_\perp$. When it becomes of order 1, say $N \approx 1/2$, the approximation in which this solution is derived breaks down and one has to go back to solving the nonlinear BK equation (4.142). Let us estimate where this breakdown of the linear regime occurs. We want to find a line in the $(x_\perp, Y)$-plane along which N is an order 1 constant: this will give us the saturation scale.

The saturation scale $Q_s(Y)$ (which now is a function of rapidity) is therefore defined by the condition

$$N(x_\perp = 1/Q_s(Y), Y) = \text{const}, \tag{4.153}$$

where the constant is of order 1. Using Eq. (4.152) in Eq. (4.153) yields

$$\bar{\alpha}_s \chi(0, \nu_0) Y + (1 + 2i\nu_0) \ln(Q_{s0}/Q_s(Y)) = 0, \tag{4.154}$$

https://doi.org/10.1017/9781009291446.005 Published online by Cambridge University Press

where $\nu_0 \equiv \nu_{sp}(x_\perp = 1/Q_s(Y), Y)$. Taking the saddle point condition (4.151) along the saturation line we get

$$\bar{\alpha}_s \chi'(0, \nu_0) Y + 2i \ln(Q_{s0}/Q_s(Y)) = 0. \tag{4.155}$$

Solving Eqs. (4.154) and (4.155) yields (Gribov, Levin, and Ryskin 1983, Iancu, Itakura, and McLerran 2002, Mueller and Triantafyllopoulos 2002)

$$Q_s(Y) = Q_{s0} \exp\left\{\bar{\alpha}_s \frac{\chi(0, \nu_0)}{1 + 2i\nu_0} Y\right\} \tag{4.156}$$

with

$$\frac{\chi'(0, \nu_0)}{\chi(0, \nu_0)} = \frac{2i}{1 + 2i\nu_0}. \tag{4.157}$$

It follows from Eq. (4.157), which one can solve numerically using Eq. (3.81), that ν_0 is simply a number (Gribov, Levin, and Ryskin 1983),

$$\nu_0 \approx -0.1275i. \tag{4.158}$$

Using this value of ν_0 in Eq. (4.156) we get

$$Q_s(Y) \approx Q_{s0}\, e^{2.44\bar{\alpha}_s Y}. \tag{4.159}$$

We have obtained a very important result: as follows from Eqs. (4.156) and (4.159), the saturation scale grows as an exponential of the rapidity. Since $Y = \ln 1/x$ this is indeed consistent with the power-of-$1/x$ growth in Eq. (3.135) obtained on general physical grounds in discussing GLR evolution. We now have the same qualitative result, with the exact exponent of the growth now specified by the slightly more detailed calculation that we have performed. Note that since $Q_{s0} \sim A^{1/6}$ (see Eq. (4.52)), we have $Q_s(Y) \sim A^{1/6}$ as well. This result can be understood as follows: the initial conditions for BK evolution (4.139) contain only one dimensionful scale Q_{s0} (we neglect the logarithm as a slowly varying function). The BK equation is conformally invariant; hence the scales resulting from this evolution, such as $Q_s(Y)$, should all be proportional to Q_{s0} and have the same A-scaling (see e.g. Kharzeev, Levin, and McLerran (2003)). It is also important to stress that the small-x evolution *does not* preserve the GGM formula (4.45) by simply including x- and A-dependence in the lowest-order nuclear gluon distribution, defined by $xG_A = AxG_N$; this would lead to a different scaling of $Q_s(Y)$ with A. In fact evolution corrections completely destroy the GGM form of N.

The region with momentum $Q < Q_s(Y)$ (corresponding to $x_\perp > 1/Q_s(Y)$), where the nonlinear term in the BK equation becomes important, is the *saturation region*.

Eliminating the rapidity dependence from Eq. (4.152), to absorb all the Y-dependence into $Q_s(Y)$, yields with the help of Eq. (4.156)

$$N(x_\perp, Y) \propto (x_\perp Q_{s0})^{1+2i\nu_{sp}} \left(\frac{Q_s(Y)}{Q_{s0}}\right)^{(1+2i\nu_0)\chi(0,\nu_{sp})/\chi(0,\nu_0)}. \tag{4.160}$$

With the accuracy of our crude version of the saddle point approximation, we write $\nu_{sp} \approx \nu_0$ in the vicinity of the saturation scale. Substituting this into Eq. (4.160) we obtain (Iancu,

https://doi.org/10.1017/9781009291446.005 Published online by Cambridge University Press

Itakura, and McLerran 2002, Mueller and Triantafyllopoulos 2002)

$$N(x_\perp, Y) \propto [x_\perp Q_s(Y)]^{1+2i\nu_0}. \tag{4.161}$$

The dipole amplitude still grows with both $x_\perp$ and Y, just as in the DLA regime. However, the growth with $x_\perp$ is slower than the quadratic DLA scaling of Eq. (4.150). Conversely, the growth in N with rapidity appears to be stronger in Eq. (4.161) than in the DLA case (4.150).

We have another important result in Eq. (4.161): the dipole scattering amplitude $N(x_\perp, Y)$, which, in general, can be a function of two independent variables $x_\perp$ and Y, is here a function of a *single* variable, $x_\perp Q_s(Y)$. This result is known as *geometric scaling*. Geometric scaling has been demonstrated (and the term coined) in an analysis of the HERA DIS data by Stasto, Golec-Biernat, and Kwiecinski (2001) (see also Kwiecinski and Stasto 2002) presenting one of the strongest arguments for the observation of saturation phenomena at HERA (see Fig. 9.1). Theoretically it was first observed as a property of GLR-type equations by Bartels and Levin (1992). For the BK equation, geometric scaling was first demonstrated deep inside the saturation region by Levin and Tuchin (2000): this result will be derived below. As we will see shortly, the expression (4.161) that we have obtained is valid outside the saturation region, but not too far from the saturation boundary, i.e., for $x_\perp Q_s(Y) \lesssim 1$. The fact that geometric scaling is valid outside the saturation region was first observed by Iancu, Itakura, and McLerran (2002). This scaling phenomenon outside the saturation region is referred to as *extended geometric scaling*.

Note that the (absolute) value of ν_0 found in Eq. (4.158) is not very large. In fact, one can check explicitly that $\chi(0, \nu_0)$ is still well described by Eq. (3.84), which was used in the diffusion approximation presented in Sec. 3.3.4. The result (4.161) is valid as long as ν_{sp} is not too far from ν_0 (cf. (4.160)). If we decrease the dipole size $x_\perp$ then we would eventually end up in the DLA region, where the saddle point is close to $\nu = -i/2$ (cf. Eq. (4.149)). Clearly Eq. (4.150) cannot be written as a function of a single variable $x_\perp Q_s(Y)$ and thus violates geometric scaling. We conclude that the extended geometric scaling of Eq. (4.161) is valid only as long as $\chi(0, \nu_{sp})$ is described better by the diffusion formula (3.84) than by the DLA approximation (4.148). By equating the two approximations we see that the transition occurs near $\nu_{sp}^{geom} = -0.22i$, which, owing to Eq. (4.151), corresponds to

$$\ln \frac{1}{x_\perp^{geom} Q_{s0}} \approx 5.75\, \bar{\alpha}_s Y, \tag{4.162}$$

so that the border (upper limit) of the extended geometric scaling region is defined by the scale $k_{geom} = 1/x_\perp^{geom}$ given by (cf. Iancu, Itakura, and McLerran (2002))

$$k_{geom} = Q_{s0} e^{5.75\,\bar{\alpha}_s Y} = Q_s(Y) \left(\frac{Q_s(Y)}{Q_{s0}} \right)^{1.35}. \tag{4.163}$$

Therefore, the extended geometric scaling is valid up to

$$k_\perp = \frac{1}{x_\perp} \leq k_{geom}. \tag{4.164}$$

https://doi.org/10.1017/9781009291446.005 Published online by Cambridge University Press

Since $k_{geom} \gg Q_s(Y)$, the region of extended geometric scaling is parametrically broad and can be quite large at large Y. For $k_\perp > k_{geom}$ the solution maps back onto the DLA regime of Eq. (4.150).

Our current analytical knowledge of the saturation scale at high energy extends well beyond the approximation derived in Eq. (4.156). In fact we know that

$$Q_s(Y) = Q_{s0} \exp\left\{\bar{\alpha}_s \frac{\chi(0,\nu_0)}{1+2i\nu_0} Y - \frac{3}{2(1+2i\nu_0)} \ln \bar{\alpha}_s Y + \text{const} \right. \\ \left. - \frac{6}{(1+2i\nu_0)^2} \sqrt{\frac{2\pi}{-\bar{\alpha}_s \chi''(0,\nu_0) Y}} + O\left(\frac{1}{Y}\right)\right\}. \tag{4.165}$$

One can show that the expression in the exponent of Eq. (4.165) is universal, in the sense that it is independent of the initial conditions for BK evolution with the exception of the constant term, which may depend on the initial conditions. As mentioned above, the first term in this expression was derived by Gribov, Levin, and Ryskin (1983) when analyzing GLR evolution and by Iancu, Itakura, and McLerran (2002) for the BK equation. The second term in the exponent of Eq. (4.165) was found by Mueller and Triantafyllopoulos (2002) and by Munier and Peschanski (2004a). The derivation of Mueller and Triantafyllopoulos (2002) is close to that presented above: however, they obtained the correct value of the second term on the right of Eq. (4.165) by modeling the saturation boundary as an absorptive barrier in the $(x_\perp, Y)$-plane. The derivation of Munier and Peschanski (2004a) employed a traveling wave solution of the BK equation. The third nontrivial ($O(1/\sqrt{Y})$) term in the exponent was also calculated by Munier and Peschanski (2004b). The traveling wave approach is very close in spirit and in letter to the method of characteristics used to solve differential equations: we will present both solutions below. For a comprehensive up-to-date summary of the results on the high energy behavior of the saturation scale we recommend a recent paper by Beuf (2010).

4.5.2 Solution inside the saturation region; geometric scaling

Let us now analyze the behavior of the solution of Eq. (4.138) deep inside the saturation region, where nonlinear effects are very important. Deep inside the saturation region, when the dipole size $x_\perp$ becomes large, $x_\perp \gg 1/Q_s(Y)$ (but we still have $x_\perp \ll 1/\Lambda_{QCD}$), the quasi-classical GGM amplitude from Eq. (4.51) approaches 1. As mentioned at the beginning of this section, analyzing Eq. (4.138) we can easily see that $N = 1$ is also a stationary solution of that equation. Therefore we conclude that, for large dipole sizes, BK evolution would not change the amplitude

$$N(\vec{x}_\perp, \vec{b}_\perp, Y) = 1, \quad x_\perp \gg 1/Q_s(Y), \tag{4.166}$$

which has reached the black-disk limit (BDL) (cf. Eq. (4.33)) and will remain there. Now let us determine the asymptotic approach to the black-disk limit (4.166). To do this we

https://doi.org/10.1017/9781009291446.005 Published online by Cambridge University Press

employ Eq. (4.137). As follows from Eq. (4.132), the S-matrix is small near the BDL, where $N \approx 1$. Keeping only terms linear in S in Eq. (4.137) yields

$$\frac{\partial S(\vec{x}_{10}, \vec{b}_\perp, Y)}{\partial Y} = -\frac{\alpha_s N_c}{2\pi^2} \int d^2x_2 \frac{x_{10}^2}{x_{20}^2 x_{21}^2} \, S(\vec{x}_{10}, \vec{b}_\perp, Y), \tag{4.167}$$

where the integral over dipole sizes goes over $x_{02}, x_{12} > 1/Q_s(Y)$. To perform the integral we replace the ultraviolet (UV) cutoff ρ in Eq. (A.20) (see also Eq. (4.64)) with $1/Q_s(Y)$ and use Eq. (A.29) to obtain

$$\frac{\partial S(\vec{x}_{10}, \vec{b}_\perp, Y)}{\partial Y} = -2\bar{\alpha}_s \ln\left[x_{10} Q_s(Y)\right] S(\vec{x}_{10}, \vec{b}_\perp, Y). \tag{4.168}$$

Defining the *scaling* variable

$$\xi \equiv \ln\left[x_\perp^2 Q_s^2(Y)\right] \tag{4.169}$$

with (cf. Eq. (4.156))

$$\frac{2\chi(0, \nu_0)}{1 + 2i\nu_0}\bar{\alpha}_s \equiv \frac{\partial \xi}{\partial Y} = \frac{\partial \ln\left[x_\perp^2 Q_s^2(Y)\right]}{\partial Y}, \tag{4.170}$$

we can rewrite Eq. (4.168) as

$$\frac{\partial S}{\partial \xi} = -\frac{1 + 2i\nu_0}{2\chi(0, \nu_0)} \xi S. \tag{4.171}$$

The solution of Eq. (4.171) can be written straightforwardly as (Levin and Tuchin 2000)

$$S(\xi) = S_0 \exp\left\{-\frac{1 + 2i\nu_0}{2\chi(0, \nu_0)} \xi^2\right\} \tag{4.172}$$

with $S_0 < 1$ a constant. The corresponding dipole amplitude N is given by

$$N(\xi)\Big|_{x_\perp \gg 1/Q_s(Y)} = 1 - S_0 \exp\left\{-\frac{1 + 2i\nu_0}{2\chi(0, \nu_0)} \xi^2\right\} \tag{4.173}$$

Equation (4.173) is known as the Levin–Tuchin formula (Levin and Tuchin 2000).

Note that the S-matrix and the amplitude N for dipole–nucleus scattering given by Eqs. (4.172) and (4.173) are functions of a single variable ξ, or, more precisely, of the combination $x_\perp Q_s(Y)$. This is indeed the *geometric scaling* found above: while before we obtained the scaling outside the saturation region, now we see that geometric scaling is also valid inside the saturation region.

Equations (4.173), (4.161), and (4.150) give us a good idea of the amplitude $N(x_\perp, Y)$ given by the solution of the BK equation as a function of rapidity Y and dipole size $x_\perp$. We see that $N(x_\perp, Y)$ grows with $x_\perp$ but at very large $x_\perp$ saturates to 1: thus the black-disk limit is not violated. Hence, at the qualitative level the overall shape of $N(x_\perp, Y)$ given by the GGM formula and shown in Fig. 4.11 is preserved. The amplitude $N(x_\perp, Y)$ also grows with rapidity Y though at larger $x_\perp$ the growth slows down, eventually stopping at the black-disk limit. The saturation scale increases with rapidity; this means that the GGM curve from Fig. 4.11 starts moving to the left on that plot. We will illustrate

these conclusions with explicit plots when we discuss the numerical solution of BK evolution.

4.5.3 Semiclassical solution

We now present another powerful approach to solving the BK equation, which allows us to reproduce the results obtained above while providing new insight.

Defining (cf. Eq. (3.74))

$$\chi(\gamma) \equiv 2\psi(1) - \psi(\gamma) - \psi(1-\gamma), \tag{4.174}$$

with γ related to ν via Eq. (3.79), we rewrite Eq. (4.144) as

$$\partial_Y \tilde{N}(\rho, Y) = \bar{\alpha}_s \chi\left(-\partial_\rho\right)\tilde{N}(\rho, Y) - \bar{\alpha}_s \tilde{N}^2(\rho, Y), \tag{4.175}$$

where $\partial_Y = \partial/\partial Y$ and

$$\rho = \ln \frac{k_\perp^2}{Q_{s0}^2}. \tag{4.176}$$

Let us now look for the solution of Eq. (4.175) using a semiclassical approximation. We write

$$\tilde{N}(\rho, Y) = e^{\Omega(\rho, Y)} \tag{4.177}$$

and assume that $\Omega(\rho, Y)$ is a slowly varying function of its arguments, such that $\Omega_{\rho Y} \ll \Omega_\rho \Omega_Y$, $\Omega_{\rho\rho} \ll \Omega_\rho^2$, $\Omega_{YY} \ll \Omega_Y^2$, with similar relations for the higher-order derivatives: the nth-order derivative is always much smaller than the nth power of the first derivative. (Here $\Omega_\rho = \partial\Omega/\partial\rho$, $\Omega_Y = \partial\Omega/\partial Y$, etc.)

Substituting Eq. (4.177) into Eq. (4.175) and employing the semiclassical approximations just outlined yields

$$\partial_Y \Omega = \bar{\alpha}_s \chi\left(-\partial_\rho \Omega\right) - \bar{\alpha}_s e^{\Omega}. \tag{4.178}$$

We will study Eq. (4.178) using the method of characteristics (see e.g. Courant and Hilbert 1953), following Gribov, Levin, and Ryskin (1983), Collins and Kwiecinski (1990), Bartels, Schuler, and Blumlein (1991), and Levin and Tuchin (2001). Defining partial derivatives

$$-\gamma \equiv \Omega_\rho, \quad \omega \equiv \Omega_Y, \tag{4.179}$$

we can rewrite Eq. (4.178) as

$$F \equiv \omega - \bar{\alpha}_s \chi(\gamma) + \bar{\alpha}_s e^{\Omega} = 0. \tag{4.180}$$

https://doi.org/10.1017/9781009291446.005 Published online by Cambridge University Press

The characteristics of Eq. (4.178) can then be found by solving the following set of ordinary differential equations:

$$\frac{d\rho}{dt} = F_{-\gamma} = \bar{\alpha}_s \frac{d\chi(\gamma)}{d\gamma}, \tag{4.181a}$$

$$\frac{dY}{dt} = F_{\omega} = 1, \tag{4.181b}$$

$$\frac{d\gamma}{dt} = -F_{\rho} - (-\gamma)F_{\Omega} = \bar{\alpha}_s \gamma e^{\Omega}, \tag{4.181c}$$

$$\frac{d\omega}{dt} = -F_{Y} - \omega F_{\Omega} = -\bar{\alpha}_s \omega e^{\Omega}, \tag{4.181d}$$

$$\frac{d\Omega}{dt} = (-\gamma)F_{-\gamma} + \omega F_{\omega} = -\bar{\alpha}_s \gamma \frac{d\chi(\gamma)}{d\gamma} + \omega. \tag{4.181e}$$

Equation (4.181b) gives $Y = t$. In addition we can use Eq. (4.180) to eliminate ω from Eqs. (4.181). The remaining equations are

$$\frac{d\rho}{dY} = \bar{\alpha}_s \frac{d\chi(\gamma)}{d\gamma}, \tag{4.182a}$$

$$\frac{d\gamma}{dY} = \bar{\alpha}_s \gamma e^{\Omega} \tag{4.182b}$$

$$\frac{d\Omega}{dY} = \bar{\alpha}_s \left[\chi(\gamma) - \gamma \frac{d\chi(\gamma)}{d\gamma} - e^{\Omega} \right]. \tag{4.182c}$$

These equations are still difficult to solve in the general case. One may construct approximations of $\chi(\gamma)$ and solve the resulting equations exactly (see Levin and Tuchin (2001)). Instead of following this path we will keep $\chi(\gamma)$ exact and will again explore the linear regime. If $\tilde{N} = e^{\Omega} \ll 1$ then we can recast Eq. (4.182c) as

$$\frac{d\Omega}{dY} \approx \bar{\alpha}_s \left[\chi(\gamma) - \gamma \frac{d\chi(\gamma)}{d\gamma} \right]. \tag{4.183}$$

We see that there exists a *critical* characteristic trajectory of constant Ω (and hence $\tilde{N}$), defined by $d\Omega/dY = 0$, which leads to the following equation for $\gamma = \gamma_{cr}$ (Gribov, Levin, and Ryskin 1983):

$$\chi(\gamma_{cr}) = \gamma_{cr} \frac{d\chi(\gamma_{cr})}{d\gamma_{cr}}. \tag{4.184}$$

This is exactly equivalent to Eq. (4.157). Equation (4.184) gives $\gamma_{cr} \approx 0.6275$, which is consistent with Eq. (4.158) (see Eq. (3.79)). The critical line in the (ρ, Y)-plane follows from Eq. (4.182a):

$$\frac{d\rho_s}{dY} = \bar{\alpha}_s \frac{\chi(\gamma_{cr})}{\gamma_{cr}}. \tag{4.185}$$

Since we have defined the critical line as a line of constant $\tilde{N}$, the definition is analogous to that of Eq. (4.153) and therefore defines the saturation scale. Solving Eq. (4.185) with

https://doi.org/10.1017/9781009291446.005 Published online by Cambridge University Press

the initial condition $\rho_s(Y=0)=0$ yields

$$\rho_s(Y)=\bar{\alpha}_s\frac{\chi(\gamma_{cr})}{\gamma_{cr}}Y, \tag{4.186}$$

which is equivalent to Eq. (4.156) if we write $\rho_s(Y)=\ln Q_s^2(Y)/Q_{s0}^2$.

Note that one can verify the $e^{\Omega}\ll 1$ approximation made in arriving at Eq. (4.183): substituting $\gamma=\gamma_{cr}$ back into Eq. (4.182c) and using the relation (4.184) one can solve the resulting equation to show that the value of Ω along the critical trajectory (Ω_{cr}) is indeed large and negative, $\Omega_{cr}\approx-\ln\bar{\alpha}_s Y$.

Finally, near the critical (saturation) line we can expand (for fixed Y) as follows:

$$\Omega\approx\Omega_{cr}+\Omega_{\rho_s}(\rho-\rho_s)=\Omega_{cr}-\gamma_{cr}(\rho-\rho_s). \tag{4.187}$$

We have also used Eq. (4.179) in arriving at Eq. (4.187). Note that $\Omega_{cr}\approx-\ln\bar{\alpha}_s Y$ is independent of ρ and is a slowly varying function of Y: therefore, it carries little dynamical information and can be treated as a constant in our approximation. Employing Eq. (4.186) to define $Q_s^2(Y)=Q_{s0}^2e^{\rho_s}$, we obtain

$$\tilde{N}(\rho,Y)=e^{\Omega}\propto e^{-\gamma_{cr}(\rho-\rho_s)}=\left(\frac{Q_s^2(Y)}{k_\perp^2}\right)^{\gamma_{cr}}, \tag{4.188}$$

which again is in perfect agreement with Eq. (4.161) (if we replace $x_\perp$ with $1/k_\perp$ in the latter). Thus we have rederived the extended geometric scaling behavior of the dipole–nucleus scattering amplitude, this time working in momentum space.

It is interesting to notice that the critical line has a very transparent physical meaning. The solution for Ω, given by Eq. (4.187), can be written as

$$\Omega\approx\Omega_{cr}-\gamma_{cr}\rho+\omega_{cr}Y, \tag{4.189}$$

with $\omega_{cr}=\bar{\alpha}_s\chi(\gamma_{cr})$. This is similar to the phase of a traveling wave packet moving along the ρ-axis with time Y, having wave number γ_{cr} and frequency ω_{cr}. (The profile of the wave packet would be determined by a prefactor to Eq. (4.188), which is not given by our approximate solution.) Such a wave packet has two characteristic velocities: the phase velocity v_{ph} (the velocity of a line with constant phase Ω) and the group velocity v_{gr} (the velocity of the maximum of the packet). Using Eq. (4.180) but dropping the e^{Ω} term, we can easily calculate these two velocities, obtaining

$$v_{gr}=\frac{\partial\omega}{\partial\gamma}=\bar{\alpha}_s\frac{d\chi(\gamma)}{d\gamma}, \tag{4.190}$$

$$v_{ph}=\frac{\omega}{\gamma}=\bar{\alpha}_s\frac{\chi(\gamma)}{\gamma}. \tag{4.191}$$

One can see that the critical line corresponds to the unique trajectory on which $v_{gr}=v_{ph}$ (Gribov, Levin, and Ryskin 1983, Munier and Peschanski 2004a).

The characteristics trajectories of BK evolution are shown in Fig. 4.28. They cannot cross each other, and the critical trajectory plays the role of a divider between two groups of trajectories, as shown in Fig. 4.28. This figure illustrates the special and essential role of

https://doi.org/10.1017/9781009291446.005 Published online by Cambridge University Press

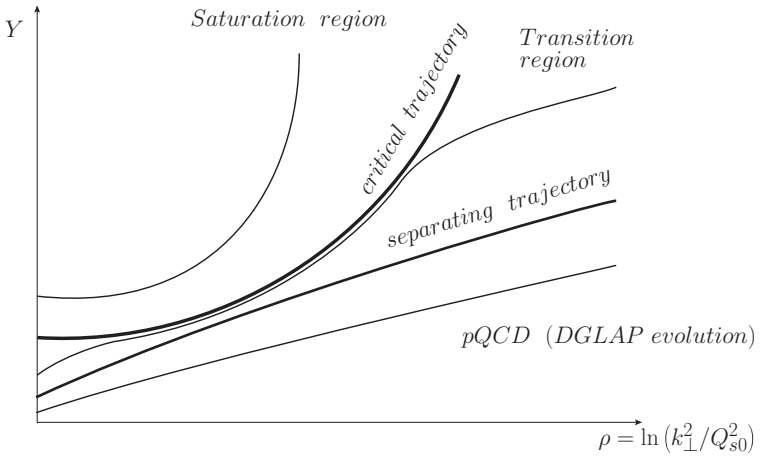

Fig. 4.28. The characteristics for Eq. (4.178) plotted in the (ρ, Y)-plane.

the critical (saturation) trajectory as a divider between pQCD (DGLAP) physics, possibly modified by small corrections due to the interactions of partons, and the saturation domain. The parton interactions are responsible for the characteristic phenomena in the latter region, in particular for the saturation of the parton density. The trajectories to the right of the critical line are very close to the trajectories of the linear (BFKL) evolution equation except in the region close to the critical line, when the effect of the critical (saturation) trajectory becomes important. This is illustrated by the "separating trajectory" also shown in Fig. 4.28, which separates the characteristics which are not affected by the saturation region, located to the right of that line, from those located to the left of the line. The unaffected characteristics are those of the DLA DGLAP. The trajectories to the left of the separating trajectory but to the right of the critical trajectory do not resemble the trajectories of the linear equation, and their behavior indicates that the linearized semiclassical approach is not applicable in this region.

4.5.4 Traveling wave solution

There is another elegant method of reproducing (and improving upon) the above results for geometric scaling and the critical anomalous dimension. We start with Eq. (4.175) and expand its kernel around γ_{cr}, defined in Eq. (4.184):

$$\chi(-\partial_\rho) = \chi(\gamma_{cr}) + (-\partial_\rho - \gamma_{cr})\chi'(\gamma_{cr}) + \tfrac{1}{2}(-\partial_\rho - \gamma_{cr})^2\chi''(\gamma_{cr}) + \cdots \tag{4.192}$$

Truncating the expansion at the quadratic level of course limits the applicability of the approach we are about to develop. Certainly this approximation would not work in the DLA region. Equation (4.175) becomes

$$\begin{aligned}\partial_Y \tilde{N}(\rho, Y) = \bar{\alpha}_s\left[\chi(\gamma_{cr}) - \tilde{N}(\rho, Y)\right]\tilde{N}(\rho, Y) - \bar{\alpha}_s\chi'(\gamma_{cr})\left(\partial_\rho + \gamma_{cr}\right)\tilde{N}(\rho, Y) \\ + \tfrac{1}{2}\bar{\alpha}_s\chi''(\gamma_{cr})(\partial_\rho + \gamma_{cr})^2\tilde{N}(\rho, Y).\end{aligned} \tag{4.193}$$

https://doi.org/10.1017/9781009291446.005 Published online by Cambridge University Press

Redefining the variables and the unknown function $\tilde{N}$ (Munier and Peschanski 2003),

$$t \equiv \tfrac{1}{2}\bar{\alpha}_s \chi''(\gamma_{cr})\gamma_{cr}^2 Y, \tag{4.194a}$$

$$x \equiv \gamma_{cr}\,\rho + \bar{\alpha}_s \left[\chi''(\gamma_{cr})\gamma_{cr}^2 - \chi(\gamma_{cr})\right] Y, \tag{4.194b}$$

$$u(t,x) \equiv \frac{2}{\chi''(\gamma_{cr})\gamma_{cr}^2}\tilde{N}(\rho, Y), \tag{4.194c}$$

and employing Eq. (4.184) brings Eq. (4.193) into the form

$$\partial_t u(t,x) = \partial_x^2 u(t,x) + u(t,x)[1-u(t,x)]. \tag{4.195}$$

This equation was first studied by Fisher (1937) and by Kolmogorov, Petrovsky, and Piskunov (1937) and is referred to in the mathematical community as the F–KPP equation. (For a review see van Saarloos (2003).)

The initial condition for Eq. (4.195) can be constructed by first finding the initial condition for Eq. (4.144). Inverting Eq. (4.143) we write

$$\tilde{N}(k_\perp, Y) = \int \frac{d^2x_\perp}{2\pi} e^{-i\vec{k}_\perp\cdot\vec{x}_\perp} \frac{N(x_\perp, Y)}{x_\perp^2}. \tag{4.196}$$

Dropping the b-dependence in Eq. (4.139) and using the result in Eq. (4.196) we obtain

$$\tilde{N}(k_\perp, Y=0) = \int \frac{d^2x_\perp}{2\pi} e^{-i\vec{k}_\perp\cdot\vec{x}_\perp} \frac{1}{x_\perp^2}\left[1 - \exp\left\{-\frac{x_\perp^2 Q_{s0}^2}{4}\ln\frac{1}{x_\perp\Lambda}\right\}\right]. \tag{4.197}$$

While the exact analytic integration in Eq. (4.197) does not lead to a compact answer, we can find the asymptotics of the initial conditions from it. At large $k_\perp$ (small $x_\perp$), expanding the exponential in Eq. (4.197) to the first nontrivial order and integrating using Eq. (A.9) yields

$$\tilde{N}(k_\perp, Y=0)\Big|_{k_\perp/Q_{s0}\gg 1} \approx \frac{Q_{s0}^2}{4k_\perp^2}. \tag{4.198}$$

At small $k_\perp$ (large $x_\perp$), dropping the exponential and integrating over $x_\perp$ with $1/Q_{s0}$ as the IR cutoff we get

$$\tilde{N}(k_\perp, Y=0)\Big|_{k_\perp/Q_{s0}\ll 1} \approx \ln\frac{Q_{s0}}{k_T}. \tag{4.199}$$

For $u(t=0,x)$ these initial conditions imply

$$u(t=0,x) \propto \begin{cases} \frac{1}{4}e^{-x/\gamma_{cr}}, & x\to+\infty, \\ -\dfrac{x}{2\gamma_{cr}}, & x\to-\infty. \end{cases} \tag{4.200}$$

It was proven that the F–KPP equation admits traveling wave solutions at late times t if the initial condition $u(0,x)$ decreases monotonically from 1 to 0 as x varies from $-\infty$ to $+\infty$, falling off exponentially with x as $x\to+\infty$ (Bramson 1983). While the initial

https://doi.org/10.1017/9781009291446.005 Published online by Cambridge University Press

condition giving $u(0, x)$ in Eq. (4.200) violates this condition at $x \to -\infty$, following Munier and Peschanski (2003) we assume that the high energy asymptotics of the solution outside the saturation region will not change significantly if we simply "freeze" $u(0, x)$ at $u = 1$ inside the saturation region. According to the theory of the F–KPP equation the asymptotic traveling wave solution depends on the speed of the exponential falloff $e^{-x/\gamma_{cr}}$ at $x \to +\infty$ in the initial condition for the equation: for $1/\gamma_{cr} \approx 1.5936 > 1$ the traveling wave solution is

$$u(t, x)\Big|_{t\to\infty} \sim f\left(x - 2t + \tfrac{3}{2}\ln t + O(1)\right), \tag{4.201}$$

for some function f. We see that $u(t, x)$ and, owing to Eq. (4.194), $\tilde{N}(\rho, Y)$ are functions of a single variable,

$$x - 2t + \tfrac{3}{2}\ln t = \gamma_{cr} \ln \frac{k_\perp^2}{Q_s(Y)^2} + \text{const}, \tag{4.202}$$

where

$$Q_s(Y)^2 = Q_{s0}^2 \exp\left\{\bar{\alpha}_s \frac{\chi(\gamma_{cr})}{\gamma_{cr}} Y - \frac{3}{2\gamma_{cr}} \ln \bar{\alpha}_s Y\right\}. \tag{4.203}$$

This is indeed geometric scaling. The saturation scale in Eq. (4.203) is identical to that in Eq. (4.165) up to the first two terms in the exponent.

Dropping the nonlinear term in Eq. (4.195) we see that $u(t, x) = e^{-x+2t}$ is clearly a solution of the resulting linearized equation, giving (Munier and Peschanski 2004a)

$$\tilde{N}(\rho, Y) \propto \left(\frac{Q_s^2(Y)}{k_\perp^2}\right)^{\gamma_{cr}}, \tag{4.204}$$

in agreement with Eqs. (4.161) and (4.188).

Owing to the approximations we have made, in expanding $\chi(\gamma)$ in order to arrive at Eq. (4.193) and in neglecting the fact that Eq. (4.200) violates the condition stated by Bramson (1983) for the existence of a traveling wave solution, we can conclude that the reduction of the BK equation to the F–KPP equation is valid only for $k_\perp$ values in the vicinity of the saturation scale. In particular, Eq. (4.193) does not give the solution (4.173) deep inside the saturation region. Interestingly, the traveling wave (geometric scaling) pattern itself appears to be more universal than the F–KPP reduction: for instance, Eq. (4.173) also has a traveling wave form. The traveling wave structure is also preserved in other models of the dipole BFKL kernel. For example, if we simplify the kernel of Eq. (4.138) by resumming only the transverse logarithms (such as $\ln x_\perp^2 Q_s^2(y)$ and $\ln x_\perp^2 \Lambda_{QCD}^2$), thus taking into account only the leading twist contributions to the full BFKL kernel, the BK equation can be reduced to a wave equation (Levin and Tuchin 2000, 2001) for which one also has a traveling wave solution (Polyanin and Zaitsev 2004, formula 3.4.1).

The existence of traveling wave solutions indicates that, at very high energy, $\tilde{N}(\rho, Y)$ behaves like a wave with a fixed coordinate (ρ) profile, which travels with increasing Y toward larger values of ρ without a change in profile. This is an important physical result from the traveling wave approach.

https://doi.org/10.1017/9781009291446.005 Published online by Cambridge University Press

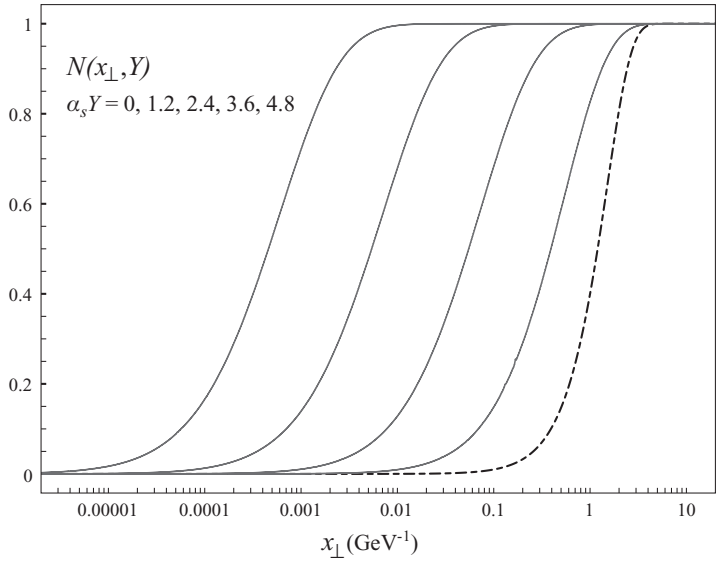

Fig. 4.29. Dipole amplitude $N(x_\perp, Y)$ plotted as a function of $x_\perp$; the curves right to left correspond to increasing values of $\alpha_s Y$, as shown in the legend. (We thank Javier Albacete for providing us with this figure.)

4.5.5 Numerical solutions

There are a number of numerical solutions of the BK equation. We are not going to give a comprehensive overview of these solutions here but will merely show some results.

A numerical solution of the BK equation (4.142) without impact parameter dependence, giving the amplitude $N(x_\perp, Y)$ as a function of $x_\perp$, is shown in Fig. 4.29 for several values of the rescaled rapidity $\alpha_s Y$. The initial condition is specified at $Y = 0$ by a slight modification of the GGM formula (4.51),

$$N(x_\perp, Y) = 1 - \exp\left\{-\frac{x_\perp^2 Q_{s0}^2}{4} \ln\left(\frac{1}{x_\perp \Lambda} + e\right)\right\} \tag{4.205}$$

with $Q_{s0} = 1$ GeV and $\Lambda = 0.2$ GeV, and is represented by the dashed line in Fig. 4.29. (Since the exponent of Eq. (4.51) is written in the $x_\perp \Lambda \ll 1$ approximation, e has been added in Eq. (4.205) to keep N positive for $x_\perp \Lambda > 1$.)

We see from Fig. 4.29 that the nonlinear small-x evolution pushes the dipole amplitude $N(x_\perp, Y)$ towards lower values of $x_\perp$ as Y increases. This is indeed in agreement with our analytical results: as $Q_s(Y)$ grows with rapidity, $1/Q_s(Y)$ decreases, moving the curve to the left along the $x_\perp$-axis. The growth in the saturation scale with rapidity Y is shown in Fig. 4.30. Here, the saturation scale is defined by requiring that $N(x_\perp = 1/Q_s(Y), Y) = 1/2$; it is plotted in Fig. 4.30 as a function of $\alpha_s Y$. Again we see qualitative agreement with the above analytical results: the saturation scale grows with rapidity. At large Y we see that $\ln Q_s(Y)$ grows linearly with $\alpha_s Y$, in agreement with Eq. (4.165); the slope of about

https://doi.org/10.1017/9781009291446.005 Published online by Cambridge University Press

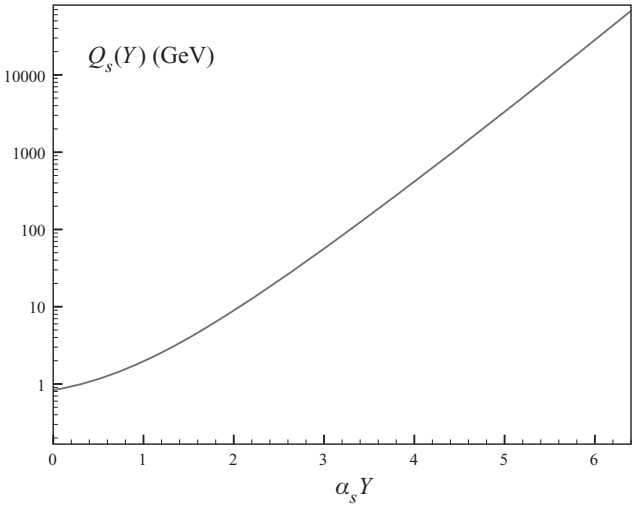

Fig. 4.30. The saturation scale $Q_s(Y)$ given by a numerical solution of the BK evolution equation, plotted as a function of the rescaled rapidity $\alpha_s Y$. (We thank Javier Albacete for providing us with this figure.)

2.1 is close to the analytical estimate, $2.44 N_c/\pi = 2.33$, in Eq. (4.159). (Note that for a more detailed comparison of Fig. 4.30 with the analytical results one also needs to take into account the logarithmic correction in the exponent of Eq. (4.165).)

The numerical solutions also exhibit the property of geometric scaling. This is demonstrated in Fig. 4.31, which shows the curves from Fig. 4.29 plotted as functions of the scaling variable

$$\tau = x_\perp Q_s(Y), \tag{4.206}$$

for the same set of $\alpha_s Y$ values as in Fig. 4.29. One can see the onset of the geometric scaling behavior both inside and outside the saturation region: as the rapidity Y increases, all the curves approach a universal scaling curve. (Indeed, at very large transverse momenta or very small $x_\perp$ the geometric scaling in Fig. 4.31 would be violated owing to the onset of the DLA DGLAP asymptotics; this is not shown in the figure because of its limited range in $x_\perp Q_s(Y)$.)

For another quantitative comparison of the analytic results and the numerical solutions we show in Fig. 4.32 a plot of the coordinate-space dipole amplitude $N(x_\perp, Y)$ as a function of the scaling variable τ over a broader range in τ, both for fixed-coupling (the dashed line) and running-coupling (the solid line) BK evolution (Albacete and Kovchegov 2007b). (The running-coupling BK evolution is given by the BK equation with running-coupling corrections included (rcBK). We will discuss rcBK in Chapter 6 (see Eq. (6.9) with kernels given either by Eq. (6.12) or Eq. (6.14)).) In the fixed-coupling case, comparing the power of 0.6 in Fig. 4.32 with Eq. (4.161) or Eq. (4.188) we see that it is consistent with the theoretical prediction of 0.6275 from, say, Eq. (4.184).

https://doi.org/10.1017/9781009291446.005 Published online by Cambridge University Press

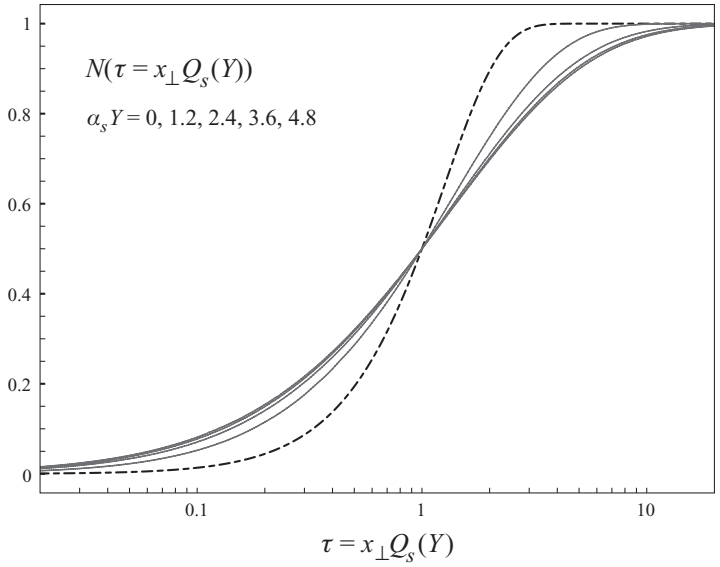

Fig. 4.31. The dipole amplitude $N(x_\perp, Y)$ as a function of the scaling variable $\tau = x_\perp Q_s(Y)$; the curves (in clockwise order in relation to the crossing point) correspond to the same values of $\alpha_s Y$ as in Fig. 4.29. (We thank Javier Albacete for providing us with this figure.) A color version of this figure is available online at www.cambridge.org/9780521112574.

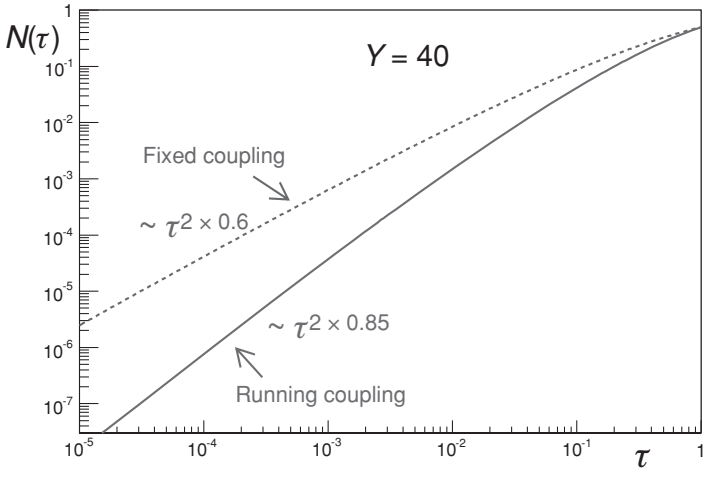

Fig. 4.32. Asymptotic solutions ($Y = 40$) of the evolution equation for running coupling (solid line) and fixed coupling with $\alpha_s = 0.2$ (dashed line). A fit to a power-law function $a\tau^{2\gamma}$ in the region $\tau \in [10^{-6}, 10^{-2}]$ yields $\gamma \approx 0.85$ for the running-coupling solution and $\gamma \approx 0.6$ for the fixed-coupling solution. (Reprinted with permission from Albacete and Kovchegov (2007b). Copyright 2007 by the American Physical Society.) A color version of this figure is available online at www.cambridge.org/9780521112574.

https://doi.org/10.1017/9781009291446.005 Published online by Cambridge University Press

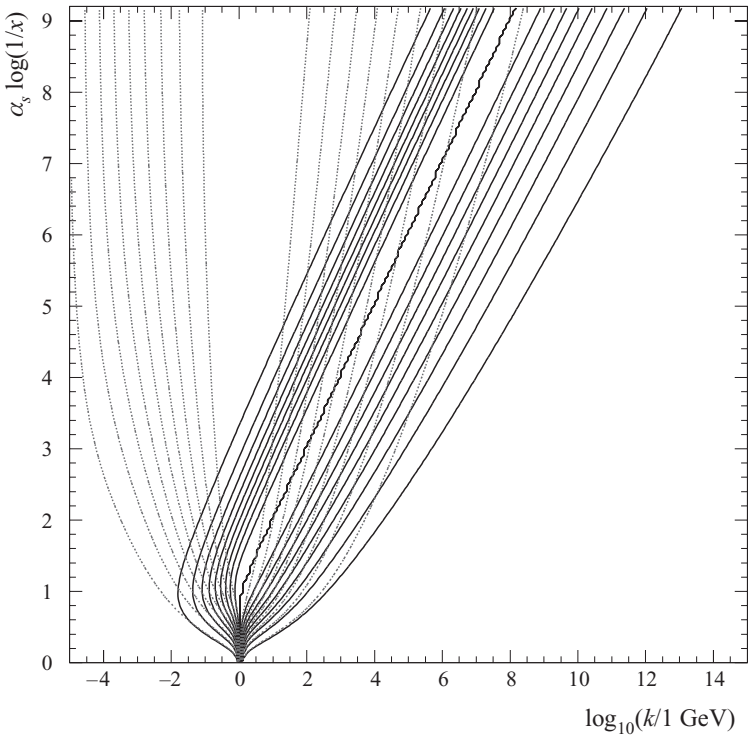

Fig. 4.33. A contour plot of the numerical solutions ($\sim k_\perp \tilde{N}(\vec{k}_\perp, Y)$) of the BFKL and BK evolution equations in momentum space, as functions of the transverse momentum $k_\perp$ and the rescaled rapidity $\alpha_s Y = \alpha_s \ln 1/x$. (We thank Anna Stasto for providing us with this figure.) A color version of this figure is available online at www.cambridge.org/9780521112574.

In Sec. 3.3.6 we discussed the two main problems of BFKL evolution unitarity violation and diffusion into the IR. From Fig. 4.29, along with the analytical calculations presented above in Sec. 4.5.2, we see that for the BK solution one always has $N \leq 1$, so that we can conclude that BK evolution does not violate the black-disk limit hence resolving this issue of the BFKL evolution. We see that a resolution of BDL violation still occurs in the perturbative domain, owing to the large value of saturation scale $Q_s(Y)$ there.

To answer the question regarding diffusion into the IR, represented by the Bartels cigar of Fig. 3.19, we will present one more result, from the numerical solution of the fixed-coupling BK equation of Golec-Biernat, Motyka, and Stasto (2002). Figure 4.33 depicts the lines of constant value for the numerical solution for $k_\perp \tilde{N}(k_\perp, Y)$ of the BFKL and BK equations in momentum space. Namely, Fig. 4.33 contains contour plots of $k_\perp \tilde{N}(k_\perp, Y)$ as a function of transverse momentum $k_\perp$ and rapidity $Y = \ln 1/x$. To illustrate the point, the initial conditions for both the BFKL and BK equations were chosen to be delta functions in the transverse momenta, $\delta(k_\perp - k_{0\perp})$ with $k_{0\perp} = 1$ GeV. One can see that the solutions of the BFKL equation (the dotted lines in Fig. 4.33) spread out as the rapidity increases. This is the diffusion discussed in Sec. 3.3.6, which is dangerous because it generates

https://doi.org/10.1017/9781009291446.005 Published online by Cambridge University Press

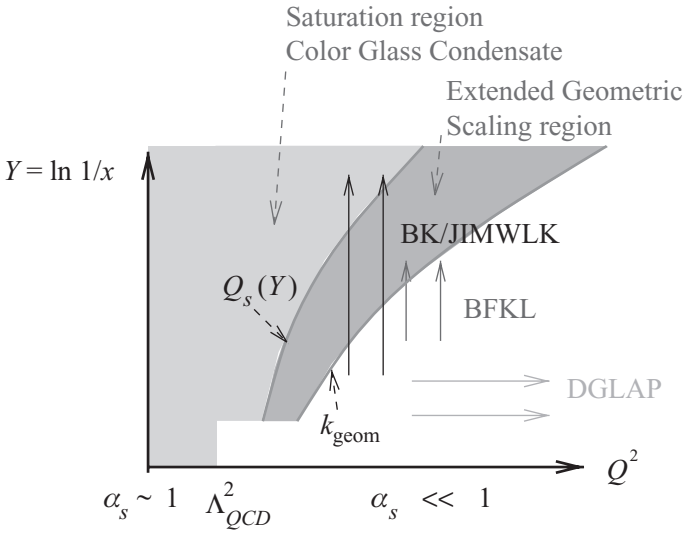

Fig. 4.34. Our understanding of high energy QCD interactions plotted in the plane of rapidity $Y = \ln 1/x$ and $\ln Q^2$. (Reprinted from Jalilian-Marian and Kovchegov (2006), with permission from Elsevier.) A color version of this figure is available online at www.cambridge.org/9780521112574.

nonperturbative low-$k_\perp$ gluons, for which our small-coupling treatment would not apply. Figure 4.33 shows that nonlinear BK evolution (shown by the solid lines in Fig. 4.33) avoids this problem. The nonlinear term in Eq. (4.138) leads to two main effects: (i) it drives the constant-value lines of the solution towards higher momenta, which is consistent with the increase in the saturation scale in Eq. (4.156), and (ii) it virtually eliminates the spread of the solution: as one can see from Fig. 4.33 the width of the $k_\perp$-distribution of the BK solution is roughly independent of rapidity. This solves the IR diffusion problem of the BFKL equation.

4.5.6 Map of high energy QCD

We summarize the results obtained in this Chapter in Fig. 4.34. This is a "map of high energy QCD", which may be compared with Fig. 4.28 and Fig. 3.22. Figure 4.34 represents the action of the evolution equations we have discussed, plotted in the $(Q^2, Y = \ln 1/x)$-plane. The region with $Q^2 \lesssim \Lambda^2_{QCD}$ is nonperturbative: there α_s is large and so we cannot use perturbation theory. The DGLAP evolution applies at large Q^2 and not very small x, as indicated by the horizontal arrows denoting evolution in Q^2. The BFKL equation is responsible for the evolution in x: it is represented by the short vertical arrows. At small enough x the linear BFKL evolution breaks down and nonlinear saturation effects set in. The transition to the saturation region is denoted by the saturation line $Q = Q_s(Y)$ (cf. the critical line in Fig. 4.28), and the saturation region is located above this line. The generalization of the BFKL evolution in x to include the saturation physics is accomplished by BK evolution in the large-N_c limit. Outside the large-N_c limit the nonlinear small-x evolution is described by the Jalilian–Marian–Iancu–McLerran–Weigert–Leonidov–Kovner

https://doi.org/10.1017/9781009291446.005 Published online by Cambridge University Press

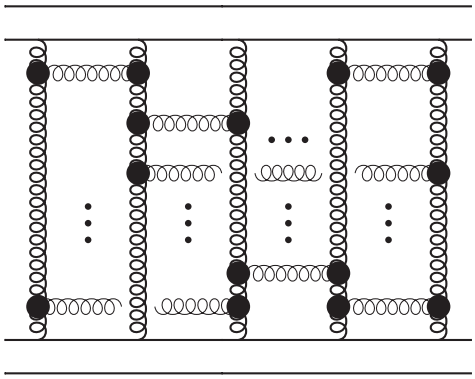

Fig. 4.35. Diagrams contributing to the BKP evolution. The vertical gluon lines are reggeized gluons, while the large solid circles denote Lipatov vertices.

(JIMWLK) evolution equation, which is a functional evolution equation to be presented in the next chapter (Jalilian-Marian *et al.* 1997b, 1999a, b, Iancu, Leonidov, and McLerran 2001a, b, Weigert 2002, Ferreiro *et al.* 2002). Both the BK and JIMWLK evolutions are shown by long vertical arrows. As shown above, geometric scaling works inside the saturation region. We have also indicated the lower boundary of the extended geometric scaling region by k_{geom} from Eq. (4.163).

The saturation region is also called the the color glass condensate, as indicated in Fig. 4.34: this term will be explained below. It is important to stress once more that all the nonlinear dynamics driving the saturation phenomena takes place for $Q_s \gtrsim Q \gg \Lambda_{QCD}$, i.e., in the perturbative region where the strong coupling constant is small and our perturbative calculations are justified.

4.6 The Bartels–Kwiecinski–Praszalowicz equation*

One may wonder whether the dipole evolution presented above should receive some potentially important subleading-N_c corrections. The problem is easier to address when formulated in terms of the standard BFKL approach. The BFKL equation of Sec. 3.3 gives the evolution for two reggeized gluons in the t-channel. Now imagine the case of an arbitrary number of t-channel reggeized gluons. Their small-x evolution is shown in Fig. 4.35.

To write down an evolution equation for n-reggeized gluon exchange, as in the BFKL case one has to define the Green function of the exchange, $G(\vec{k}_{1\perp}, \ldots, \vec{k}_{n\perp}; \vec{k}'_{1\perp}, \ldots, \vec{k}'_{n\perp}; Y)$, corresponding to a "rectangle" like that in Fig. 3.5, with n gluon legs attached to it from above and n more attached from below, as shown on the left of Fig. 4.36. Moreover, we only account for the discontinuities (the imaginary parts) of the Green function between all consecutive t-channel gluon exchanges, as shown by the cuts in Fig. 4.36. The scattering amplitude without such cuts can be reconstructed from the BKP Green function by the repeated use of dispersion relations, as in the case of gluon reggeization considered in Sec. 3.3.5.

https://doi.org/10.1017/9781009291446.005 Published online by Cambridge University Press

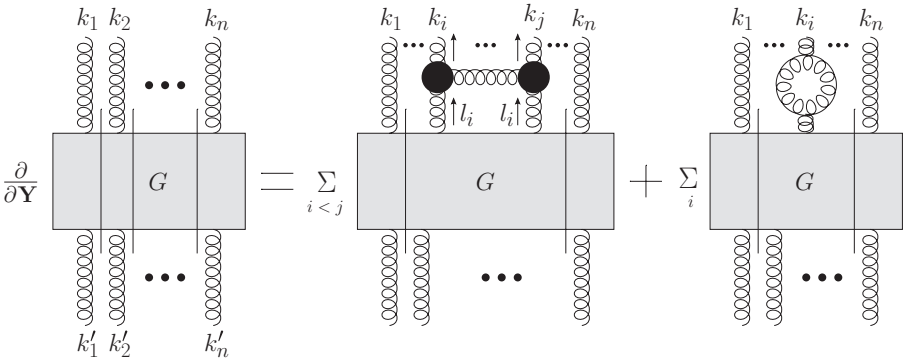

Fig. 4.36. Diagrammatic representation of the BKP evolution equation for the $2n$-point Green function. All momenta flow up in the diagrams and the vertical straight lines denote cuts.

One can write down an evolution equation for this Green function by applying the BFKL kernel to any pair of the reggeized gluons shown in Fig. 4.36. One obtains the Bartels–Kwiecinski–Praszalowicz (BKP) equation,

$$\begin{aligned}\partial_Y G(\vec{k}_{1\perp},\ldots,\vec{k}_{n\perp};\vec{k}'_{1\perp},\ldots,\vec{k}'_{n\perp};Y)\\ =\sum_{i=1}^{n}\omega_G(\vec{k}_{i\perp})G(\vec{k}_{1\perp},\ldots,\vec{k}_{n\perp};\vec{k}'_{1\perp},\ldots,\vec{k}'_{n\perp};Y)+\lambda_{color}\sum_{i<j}\int d^2l_i d^2l_j\\ \times K^{ij}_{NF}(\vec{k}_{i\perp},\vec{k}_{j\perp};\vec{l}_{i\perp},\vec{l}_{j\perp})G(\vec{k}_{1\perp},\ldots,\vec{l}_{i\perp},\ldots,\vec{l}_{j\perp},\ldots,\vec{k}_{n\perp};\vec{k}'_{1\perp},\ldots,\vec{k}'_{n\perp};Y),\end{aligned} \tag{4.207}$$

where $K^{ij}_{NF}(\vec{k}_{i\perp},\vec{k}_{j\perp};\vec{l}_{i\perp},\vec{l}_{j\perp})$ is the nonforward BFKL kernel, given by (cf. Eq. (3.103))

$$\begin{aligned}K^{ij}_{NF}(\vec{k}_{i\perp},\vec{k}_{j\perp};\vec{l}_{i\perp},\vec{l}_{j\perp})=\frac{\alpha_s N_c}{2\pi^2}\,\delta^{(2)}(\vec{k}_{i\perp}+\vec{k}_{j\perp}-\vec{l}_{i\perp}-\vec{l}_{j\perp})\\ \times\left[\frac{k^2_{i\perp}}{l^2_{i\perp}(\vec{k}_{i\perp}-\vec{l}_{i\perp})}+\frac{k^2_{j\perp}}{l^2_{j\perp}(\vec{k}_{i\perp}-\vec{l}_{i\perp})}-\frac{(\vec{k}_{i\perp}+\vec{k}_{j\perp})^2}{l^2_{i\perp}l^2_{j\perp}}\right].\end{aligned} \tag{4.208}$$

The coefficient λ_{color} depends on the color-SU(3) representation of the two gluons that interact, namely

$$\lambda_{singlet}=1,\quad \lambda_{8_S}=\lambda_{8_A}=\tfrac{1}{2},\quad \lambda_{10}=\lambda_{\overline{10}}=0,\quad \lambda_{27}=-\tfrac{1}{3} \tag{4.209}$$

where $8_S, 8_A, 10, \overline{10}, 27$ denote the representations of the SU(3) color group (the subscripts S, A denote the symmetric and antisymmetric representations). For $n=2$ in the color-singlet case Eq. (4.207) reduces to the BFKL equation (3.58) and in the color-octet case Eq. (4.207) becomes the equation (3.102) leading to the bootstrap equation (3.107).

The general proof of Eq. (4.207) can be found in the papers of Bartels (1980) and Kwiecinski and Praszalowicz (1980) (see also Jaroszewicz 1980). A review of this approach

https://doi.org/10.1017/9781009291446.005 Published online by Cambridge University Press

Table 4.1. *The intercepts of multi-reggeized gluon states as found in Korchemsky, Kotanski, and Manashov (2002)*

Number of reggeized gluons	Intercept
$n = 2$	$2.77\bar{\alpha}_s$
$n = 4$	$0.67\bar{\alpha}_s$
$n = 6$	$0.39\bar{\alpha}_s$

was given by Lipatov (1999). (See also the papers of Korchemsky, Kotanski, and Manashov (2004) and Lipatov (2009) and references therein for recent developments.)

The contribution of multi-reggeized gluon states to the onium–onium scattering cross section is N_c-suppressed compared with that of single-BFKL-pomeron exchange. To see this suppression for a four-reggeized gluon state (with all four gluons in a net color-singlet state) one has to first subtract from it the color configurations corresponding to single- and double-BFKL-ladder exchanges (which are included in the four-gluon evolution, owing to the bootstrap property of Sec. 3.3.5), along with the three-reggeized gluon configurations. The remaining quantity would contribute to the onium–onium cross section at order $1/N_c^4$ (for $\alpha_s N_c$ fixed); this is suppressed in comparison with single-BFKL-ladder exchange, which is of order $1/N_c^2$, (4.102), and is comparable with double-BFKL-pomeron exchange, also of order $1/N_c^4$. The dipole model presented above does not contain such contributions: in fact one has to augment the dipole model with color quadrupoles to reproduce the evolution of the four-gluon BKP state (Chen and Mueller 1995).

While the coupling of the four-gluon BKP state, and of the states with higher numbers of gluons, to the onia is N_c^2-suppressed, their evolution (4.207) clearly contains a leading-N_c contribution.[8] One may, therefore, be concerned that the solutions of Eq. (4.207) could lead to these multi-reggeized gluon states giving contributions to the cross section that grow with rapidity faster than the multi-BFKL-pomeron exchanges at the same order in N_c^2-suppression and thus become order-1 corrections to the dipole model (or even dominating the cross section). For instance, the four-gluon state, after all subtractions, might grow with energy faster than the two-BFKL-pomeron exchange contribution. Such worries have been put to rest by an explicit solution of the large-N_c version of the BKP equation, performed by Korchemsky, Kotanski, and Manashov (2002), whose results (for even n) are summarized in Table 4.1. One can see, for instance, that the intercept of the $n = 4$ state, equal to $0.67\bar{\alpha}_s$, is significantly smaller than the effective intercept due to two BFKL ladder exchanges, which is $2(\alpha_P - 1) = 8\bar{\alpha}_s \ln 2 \approx 5.55\bar{\alpha}_s$ and can be safely neglected. More importantly, it follows from Table 4.1 that the higher-n states actually have intercepts that *decrease* with n, thus becoming progressively less important than the n-pomeron contribution with intercept $n(\alpha_P - 1)$, growing linearly with n. States with odd n are also unimportant for the total

[8] For a general SU(N_c) group the decomposition of $N_c \otimes N_c$ contains another representation, denoted $\mathcal{R}_7$, with $\lambda_{\mathcal{R}_7} = 1/N_c$. The evolution of two gluons in this representation, along with that in representation 27 ($\lambda_{27} = -1/N_c$) is N_c-suppressed. (See Kovner and Lublinsky (2007) for a detailed presentation of group factors.)

cross section: their intercepts are less than or equal to zero. In the next section we will work out the case of an odderon, which corresponds to three gluons in the t-channel.

4.7 The odderon*

Consider a scattering amplitude mediated by a t-channel exchange of a C-odd object, all of whose other quantum numbers are those of a pomeron (or QCD vacuum). Such a process is important phenomenologically for the exclusive production of some C-odd vector mesons, such as pions, J/ψ, η_C, etc. The exchanged object with vacuum quantum numbers except for $C = -1$ is called the *odderon* (by analogy with the definition of the pomeron in Sec. 3.2). Its existence in QCD was first suggested by Lukaszuk and Nicolescu (1973).

Let us determine the odderon contribution to onium–onium scattering. We start by considering the general scattering amplitude for an onium on a target. The charge conjugation operation interchanges the quark and the antiquark:

$$C: \qquad \vec{x}_{1\perp} \leftrightarrow \vec{x}_{0\perp}, \qquad z \leftrightarrow 1 - z, \tag{4.210}$$

where as usual the quark in the onium is located at $\vec{x}_{1\perp}$ while the antiquark is at $\vec{x}_{0\perp}$, and z is the longitudinal momentum fraction carried by the quark. In the GGM or LLA approximations the z-dependence can be neglected: we will discard it here. The odderon-exchange amplitude, by definition, corresponds to an elastic amplitude that is anti-symmetric under the operation (4.210):

$$\mathcal{O}(\vec{x}_{1\perp}, \vec{x}_{0\perp}, Y) = -\mathcal{O}(\vec{x}_{0\perp}, \vec{x}_{1\perp}, Y). \tag{4.211}$$

We can relate the elastic odderon amplitude $\mathcal{O}$ to the S-matrix $S(\vec{x}_{1\perp}, \vec{x}_{0\perp}, Y)$ (in the notation of Eq. (4.140)) by

$$\mathcal{O}(\vec{x}_{1\perp}, \vec{x}_{0\perp}, Y) = \frac{1}{2i}\left[S(\vec{x}_{1\perp}, \vec{x}_{0\perp}, Y) - S(\vec{x}_{0\perp}, \vec{x}_{1\perp}, Y)\right]. \tag{4.212}$$

In the eikonal and LLA approximations we have $S(\vec{x}_{0\perp}, \vec{x}_{1\perp}) = S^\dagger(\vec{x}_{1\perp}, \vec{x}_{0\perp})$, so that

$$\begin{aligned}\mathcal{O}(\vec{x}_{1\perp}, \vec{x}_{0\perp}, Y) &= \frac{1}{2i}\left[S(\vec{x}_{1\perp}, \vec{x}_{0\perp}, Y) - S^\dagger(\vec{x}_{1\perp}, \vec{x}_{0\perp}, Y)\right] \\ &= \operatorname{Im} S(\vec{x}_{1\perp}, \vec{x}_{0\perp}, Y)\end{aligned} \tag{4.213}$$

(Hatta *et al.* 2005a). We see that the odderon amplitude is equal to the imaginary part of the S-matrix and hence, to the real part of the T-matrix. We can thus generalize Eq. (4.132) to

$$S(\vec{x}_{1\perp}, \vec{x}_{0\perp}, Y) = 1 - N(\vec{x}_{1\perp}, \vec{x}_{0\perp}, Y) + i\mathcal{O}(\vec{x}_{1\perp}, \vec{x}_{0\perp}, Y). \tag{4.214}$$

Now let us return to onium–onium scattering. The lowest-order C-odd onium–onium scattering amplitude is given by the three-gluon exchange diagrams depicted in Fig. 4.37. The gluons in Fig. 4.37 couple only to the quarks and antiquarks in the onia: contributions with gluons coupling to each other are either C-even or zero, by color algebra considerations. In general, three gluons can be either in the f^{abc} or d^{abc} color configuration, where $d^{abc} = 2\mathrm{Tr}[t^a\{t^b, t^c\}]$ is an absolutely symmetric object, the braces denoting an anticommutator. We are interested in the part of the diagram in Fig. 4.37 (in the eikonal approximation)

https://doi.org/10.1017/9781009291446.005 Published online by Cambridge University Press

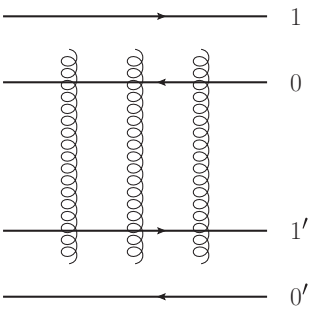

Fig. 4.37. The lowest order odderon exchange diagram in onium–onium scattering. As usual, the disconnected gluon lines imply sums over all couplings to the quark and antiquark lines.

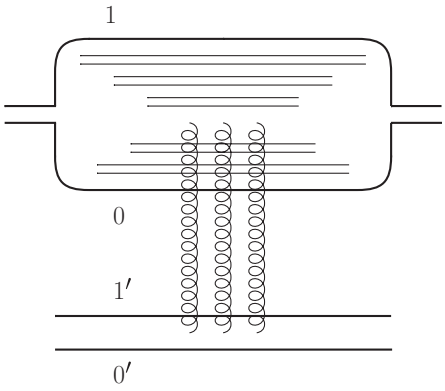

Fig. 4.38. Odderon evolution in the large-N_c approximation: a dipole cascade convoluted with triple-gluon exchange.

contributing to the odderon onium–onium amplitude $\mathcal{O}(\vec{x}_{1\perp}, \vec{x}_{0\perp}; \vec{x}'_{1\perp}, \vec{x}'_{0\perp}, Y)$. One can show, using Eq. (4.212), that only the d^{abc} configuration contributes to $\mathcal{O}$. By analogy with Eq. (4.117) we write, switching to the complex-variable notation of Sec. 4.3.3,

$$\mathcal{O}(\rho_1, \rho_0; \rho_{1'}, \rho_{0'}; Y = 0) = c_0\, \alpha_s^3 \ln^3 \left| \frac{\rho_{11'}\rho_{00'}}{\rho_{10'}\rho_{01'}} \right| \tag{4.215}$$

with c_0 some constant (dependent on N_c), whose exact value is not important for us. Clearly the exchange in Eq. (4.215) is C-odd, as it changes sign under either the $1 \leftrightarrow 0$ or the $1' \leftrightarrow 0'$ interchange.

Equation (4.215) can be used as the initial condition of the LLA small-x evolution in the large-N_c limit, which we would like to construct for the odderon amplitude $\mathcal{O}(\vec{x}_{1\perp}, \vec{x}_{0\perp}, Y)$. Above, in constructing the dipole model cascade we did not make any assumptions about the C-parity of the scattering amplitude: hence the dipole evolution should apply to the odderon case. Working in the rest frame of one of the colliding onia we present the odderon evolution in Fig. 4.38, constructed by analogy with Fig. 4.22. The incoming onium develops a dipole cascade, with one dipole exchanging three t-channel gluons

https://doi.org/10.1017/9781009291446.005 Published online by Cambridge University Press

with the lower onium at rest. Note that the triple-gluon exchange of Fig. 4.37 can only couple to a single dipole in the onium wave function, since a single gluon cannot couple to a color dipole in an elastic process. Hence the evolution for the odderon amplitude should be described by the same dipole BFKL equation, with different initial condition (4.215).

By analogy with Eq. (4.87) we write (Kovchegov, Szymanowski, and Wallon (2004))

$$\begin{aligned}
&\partial_Y \mathcal{O}(\vec{x}_{1\perp}, \vec{x}_{0\perp}; \vec{x}'_{1\perp}, \vec{x}'_{0\perp}; Y) \\
&= \frac{\alpha_s N_c}{2\pi^2} \int d^2 x_2 \frac{x_{10}^2}{x_{20}^2 x_{21}^2} \\
&\quad \times \left[\mathcal{O}(\vec{x}_{1\perp}, \vec{x}_{2\perp}; \vec{x}'_{1\perp}, \vec{x}'_{0\perp}; Y) + \mathcal{O}(\vec{x}_{2\perp}, \vec{x}_{0\perp}; \vec{x}'_{1\perp}, \vec{x}'_{0\perp}; Y) - \mathcal{O}(\vec{x}_{1\perp}, \vec{x}_{0\perp}; \vec{x}'_{1\perp}, \vec{x}'_{0\perp}; Y) \right].
\end{aligned} \tag{4.216}$$

This is the linear evolution equation for the odderon amplitude; Eq. (4.215) provides its initial conditions. While Eq. (4.216) is derived here in the large-N_c limit it is also valid for any N_c, as shown by Hatta *et al.* (2005a).

Since Eq. (4.216) is simply the BFKL equation, we know how to find its solution. Decomposing the initial condition (4.215) over the eigenfunctions of the Möbius group, we write

$$\begin{aligned}
&\mathcal{O}(\rho_1, \rho_2; \rho_{1'}, \rho_{2'}; Y = 0) \\
&= c_0 \, \alpha_s^3 \frac{6}{\pi^2} \sum_{\text{odd}\, n} \int_{-\infty}^{\infty} d\nu \int d^2 \rho_a \\
&\quad \times \frac{\nu^2 + \frac{1}{4} n^2}{\left[\nu^2 + \frac{1}{4}(n+1)^2\right]\left[\nu^2 + \frac{1}{4}(n-1)^2\right]} \chi(n, \nu) E^{n,\nu}(\rho_{1a}, \rho_{2a}) E^{n,\nu *}(\rho_{1'a}, \rho_{2'a})
\end{aligned} \tag{4.217}$$

and, using Eq. (4.115), we obtain the general solution of Eq. (4.216) for the odderon amplitude:

$$\begin{aligned}
&\mathcal{O}(\rho_1, \rho_2; \rho_{1'}, \rho_{2'}; Y) \\
&= c_0 \, \alpha_s^3 \frac{6}{\pi^2} \sum_{\text{odd}\, n} \int_{-\infty}^{\infty} d\nu \int d^2 \rho_a \, e^{\bar{\alpha}_s \chi(n,\nu) Y} \\
&\quad \times \frac{\nu^2 + \frac{1}{4} n^2}{\left[\nu^2 + \frac{1}{4}(n+1)^2\right]\left[\nu^2 + \frac{1}{4}(n-1)^2\right]} \chi(n, \nu) E^{n,\nu}(\rho_{1a}, \rho_{2a}) E^{n,\nu *}(\rho_{1'a}, \rho_{2'a}).
\end{aligned} \tag{4.218}$$

Owing to the property (4.120) of the functions $E^{n,\nu}$ this amplitude is indeed C-odd. Note that the solution (4.125) of the BFKL equation for the forward amplitude is C-even as it contains a sum over even n, while the odderon solution (4.218) has a sum over odd n and is therefore C-odd. We see from Eq. (4.216) that in dipole language the odderon and

https://doi.org/10.1017/9781009291446.005 Published online by Cambridge University Press

the pomeron evolutions are given by the same dipole BFKL equation; the different initial conditions project out different contributions.

The solution (4.218), constructed in this form by Kovchegov, Szymanowski, and Wallon (2004), is analogous to that found in momentum space earlier by Bartels, Lipatov, and Vacca (2000), which is known as the BLV solution. The latter was obtained by solving the BKP equation (4.207) for three gluons in the d^{abc} color state. We can now find the intercept of the three-gluon BKP d^{abc}-state. The leading high energy asymptotics of the BFKL solution (4.125) is given by the $n = 0$ term in the series, since it carries the largest intercept. In the case of Eq. (4.218) the $n = 0$ term is no longer included in the sum, and the largest intercept comes from the $n = \pm 1$ terms, giving, in the saddle-point approximation around $\nu = 0$ (Bartels, Lipatov, and Vacca 2000),

$$\alpha_{odd} - 1 = \bar{\alpha}_s \chi(n = \pm 1, \nu = 0) = 0. \tag{4.219}$$

We see that the odderon amplitude does not grow with energy, even when small-x evolution is included! This is an interesting result, which may be the reason for the lack of experimental observation of the odderon.

The odderon amplitude also receives saturation corrections due to nonlinear evolution. Consider dipole–nucleus scattering. The nonlinear evolution equation for the C-odd amplitude $\mathcal{O}(\vec{x}_{1\perp}, \vec{x}_{0\perp}, Y)$ in the large-N_c approximation can be found by inserting Eq. (4.214) into Eq. (4.137) and taking the imaginary part of the resulting expression, keeping in mind that both N and $\mathcal{O}$ are real quantities. This gives (Kovchegov, Szymanowski, and Wallon 2004, Hatta *et al.* 2005a)

$$\begin{aligned}\partial_Y \mathcal{O}(\vec{x}_{1\perp}, \vec{x}_{0\perp}, Y) = {} & \frac{\alpha_s N_c}{2\pi^2} \int d^2x_2 \frac{x_{01}^2}{x_{20}^2 x_{21}^2} \\ & \times \left[\mathcal{O}(\vec{x}_{1\perp}, \vec{x}_{2\perp}, Y) + \mathcal{O}(\vec{x}_{2\perp}, \vec{x}_{0\perp}, Y) - \mathcal{O}(\vec{x}_{1\perp}, \vec{x}_{0\perp}, Y)\right] \\ & - \frac{\alpha_s N_c}{2\pi^2} \int d^2x_2 \frac{x_{01}^2}{x_{20}^2 x_{21}^2} \\ & \times \left[\mathcal{O}(\vec{x}_{1\perp}, \vec{x}_{2\perp}, Y) N(\vec{x}_{2\perp}, \vec{x}_{0\perp}, Y) + N(\vec{x}_{1\perp}, \vec{x}_{2\perp}, Y) \mathcal{O}(\vec{x}_{2\perp}, \vec{x}_{0\perp}, Y)\right].\end{aligned} \tag{4.220}$$

We conclude that saturation simply suppresses the odderon amplitude $\mathcal{O}$ further, by making it decrease with energy. This can be readily seen from Eq. (4.220) by, for instance, substituting $N = 1$ in it for $x_{20}, x_{21} > 1/Q_s(Y)$, corresponding to the saturated total dipole–nucleus cross section. One would then get the S-matrix version of the Levin–Tuchin formula, Eq. (4.172), but now for the odderon amplitude $\mathcal{O}$, indicating that it falls off steeply with increasing energy or rapidity in the presence of saturation.

Further reading

More details on some aspects of the GGM multiple-rescattering formula and on BK evolution, with its solution, can be found in the reviews by Iancu and Venugopalan (2003),

https://doi.org/10.1017/9781009291446.005 Published online by Cambridge University Press

Weigert (2005), and Jalilian-Marian and Kovchegov (2006). Further information on the semiclassical approximation for the solution of the BK equation can be found in Levin and Tuchin (2000, 2001) (see also Diaz Saez and Levin (2011) and references therein). A comprehensive summary of the current status and achievements of the traveling wave approach can be found in Beuf (2010). The most recent status of the saturation boundary approaches to solving the BK equation at higher orders is discussed in Avsar *et al.* (2011) and references therein. The consequences of the conformal symmetry of the fixed-coupling BK evolution for its solution have been recently explored by Gubser (2011).

The solution of the BKP equation, especially for the odderon case, has been widely discussed, and we consider that the review and paper of Lipatov (1999, 2009) together with the paper of Korchemsky, Kotanski, and Manashov (2004) can bring the reader to the current understanding of this problem. A comprehensive review of the theory of odderon evolution and the status of experimental searches for the odderon was given by Ewerz (2003).

Exercises

4.1 By summing all possible connections of the t-channel gluons to the dipole in Fig. 4.10, derive Eq. (4.40) explicitly.

4.2** Find the virtual correction to the onium wave function in Eq. (4.64) by an explicit calculation of diagrams. One may directly sum the LCPT diagrams in Fig. 4.14 (Chen and Mueller 1995). Alternatively, one may start with a momentum-space expression for each distinct contributing Feynman diagram, Fourier-transform it into coordinate space in x^-, regulate the x^--integrals, and integrate over the x^--coordinates of the quark–gluon vertices from $-\infty$ to 0. Fourier-transforming the obtained expression into transverse coordinate space should yield (4.64).

4.3 Follow the steps outlined in the text to find the eigenvalues of the kernel of Eq. (4.90). Namely, starting with Eq. (4.95) reduce it to Eq. (4.97).

4.4 Starting with Eq. (4.90) use the substitution (4.98) to obtain the BFKL equation (3.58) for the function f. You may find Eqs. (A.9) and (A.10) handy.

4.5 **(a)** Solve the following zero-transverse-dimensional equation for the generating functional $Z(Y, u)$ (cf. Eq. (4.77)):

$$\partial_Y Z = \alpha_s (Z^2 - Z) \tag{4.221}$$

with initial condition $Z(Y = 0, u) = 0$. Using Eq. (4.81) find the number of dipoles in this "wave function".

(b) Perform a similar exercise for a toy model of the BK equation (4.138): solve

$$\partial_Y N = \alpha_s N - \alpha_s N^2, \tag{4.222}$$

https://doi.org/10.1017/9781009291446.005 Published online by Cambridge University Press

with $N(Y=0) = N_0 \ll 1$ as the initial condition; $N_0 > 0$ is a constant. Show that $N(Y) \to 1$ as $Y \to \infty$.

4.6 Suppose that the dipole–nucleus scattering amplitude in the linear regime outside the saturation region is given by the following approximation of the DLA formula (4.150) (for $x_\perp Q_{s0} \ll 1$)

$$N(x_\perp, Y) = (x_\perp Q_{s0})^2 \exp\left\{2\sqrt{\bar{\alpha}_s Y \ln[1/(x_\perp Q_{s0})^2]}\right\}. \tag{4.223}$$

(a) Find the energy-dependent saturation scale $Q_s(Y)$ by requiring that

$$N(x_\perp = 1/Q_s(Y), Y) = 1. \tag{4.224}$$

(b) Show that for $1/Q_s(Y) \gg x_\perp \gg 1/k_{geom}$, with $k_{geom} = Q_s^2(y)/Q_{s0}$, (cf. Eq. (4.163)), Eq. (4.223) can be rewritten as

$$N(x_\perp, Y) \approx x_\perp Q_s(Y), \tag{4.225}$$

i.e., as a function of a single variable $x_\perp Q_s(Y)$ instead of the two variables $x_\perp$ and Y (cf. Eq. (4.161)). This is a simplified derivation of the extended geometric scaling (Iancu, Itakura, and McLerran 2002).

4.7* Derive Eq. (4.217) with $\mathcal{O}(\rho_1, \rho_2; \rho_{1'}, \rho_{2'}; Y = 0)$ as given in Eq. (4.215).

4.8 Determine the high energy asymptotics of the F_2 structure function (and $\sigma_{tot}^{\gamma^* A}$). At very small x we have $Q_s \gg Q$. Argue that in such a case the $x_\perp$-integral in (4.12) is dominated by $1/Q_s \ll x_\perp \ll 1/Q$. Approximating the dipole–nucleus interaction by a black disk of radius R, so that $N(x_\perp, b_\perp, Y) \approx \theta(R - b_\perp)$, and expanding the Bessel functions in Eqs. (4.18) and (4.21), show using Eq. (4.10a) that

$$F_2 \sim \sigma_{tot}^{\gamma^* A} \sim R^2 \ln \hat{s} \sim \ln^3 \hat{s}; \tag{4.226}$$

the last conclusion results from the substitution $R = R_0 + a \ln \hat{s}$, reflecting the diffusion of the black-disk radius (3.115). Equation (4.226) sets an upper limit on $\sigma_{tot}^{\gamma^* A}$ known as the *Gribov bound* (Gribov 1970).

https://doi.org/10.1017/9781009291446.005 Published online by Cambridge University Press